Digital DLTS studies on radiation induced defects in Si, GaAs and GaN

by

Walter Ernst Meyer

Submitted in partial fulfilment of the degree

PhD (Physics)

in the Faculty of Natural & Agricultural Science

University of Pretoria

Pretoria

November 2006

Supervisor: Prof F D Auret

Co-supervisor: Prof S A Goodman

Digital DLTS studies on radiation induced defects in Si, GaAs and GaN

by

Walter Ernst Meyer

Submitted in partial fulfilment of the degree PhD (Physics) in the Faculty of Natural & Agricultural Science, University of Pretoria

Supervisor: Prof F D Auret
Co-supervisor: Prof S A Goodman

Since the development of deep level transient spectroscopy (DLTS) in the 1970's by Lang and others, the technique has become a powerful analytical tool to characterise the electrical properties of defects in semiconductors. With the development of more powerful computers and improved data acquisition systems, it has become possible to replace the original analogue boxcar analysers and lock-in amplifiers that were commonly used in early DLTS systems with digitisers and digital signal processing equipment.

The use of a computer for signal processing allows for much more flexibility in the DLTS system. For instance, a digital DLTS system is capable of measuring a much wider range of emission rates than an analogue system. Furthermore, since the digital DLTS system does not rely on a repetitive signal, such a system can observe phenomena such as defect metastability that cannot be observed in an analogue system.

In this thesis, the design and characterisation of a digital DLTS system is described. The results of a number of experiments that illustrated the capabilities of the system are reported.

The extended range of emission rates that could be measured by the system were illustrated by the measuring of the EL2 defect in GaAs over the temperature range 270 – 380 K (corresponding to emission rates ranging from less than 10^{-3} s^{-1} to more than 10^{3} s^{-1}). The results compared well with previous results obtained by means of an analogue DLTS system. Further low temperature measurements on the E2 defect in GaAs showed that in the low temperature region, thermal radiation from the cryostat shroud influenced carrier emission.

The field dependence of the emission rate of a number of defects, including defects in as-grown n-GaN, He-ion irradiated n-GaN and Si, was investigated as well.

The ability of the digital DLTS system to measure single transients was used to investigate configurationally bistable defects in He-ion irradiated *p*-Si and a sputter-induced defect with negative-U properties in n-GaN. In both of these cases, the results proved far superior to those obtained by means of an analogue system.

Acknowledgements

I would like to thank the following persons for their contributions towards the completion of this study:

- My supervisor, Prof F D Auret and co-supervisor, Prof S A Goodman for their guidance, support, encouragement and valuable discussions.

- Prof G Myburg for the vacuum deposition of the Schottky contacts, and helpful suggestions and discussions during the experimental part of this study.

- The South African National Research Foundation for their financial assistance during this study.

- My colleagues in the Physics Department of the University of Pretoria for their willingness to help, their interest and encouragement.

- Many friends for their encouragement, help and moral support.

- Prof L Strauss for introducing me to physics when I was a child and for constantly encouraging me (and threatening me) to complete this PhD.

- My parents for their endless support and encouragement.

Contents

1 Introduction

Semiconductor technology forms the basis of the modern electronics industry. The current drive toward miniaturisation is fuelled by the demand for faster switching speeds, lower power requirements and higher integration. As devices become smaller, they become more sensitive to the effects of minor imperfections in the crystal lattice. These imperfections, called *defects*, are formed either during the growth of the semiconductor crystal or during subsequent processing steps such as metallization, ion-implantation, annealing and etching, and can affect the performance of devices.

In most cases, defects in semiconductors are detrimental to device performance, reducing the mobility of carriers and acting as trapping and recombination centres that reduce free carrier lifetime. However, there are a number of applications in which defects are used to enhance device performance, e.g. electron irradiation induced defects in Si power diodes increase the switching speed of the diodes by acting as recombination centres at the *p-n* junction that reduce minority carrier lifetime (Baliga, 1996). In order to predict the influence that a defect would have on device performance (be it detrimental or beneficial) it is essential that the properties of the defect are known. Intimate knowledge of the defect's characteristics would allow the use of defect engineering to improve the device characteristics by eliminating detrimental defects and in some cases even introducing defects that enhance device performance. Peaker (1993) discusses some examples of defect engineering.

One of the most important techniques used to determine the electrical characteristics of a defect is known as Deep Level Transient Spectroscopy (DLTS). During a DLTS measurement, the emission of carriers from a deep-level trap is investigated as a function of temperature. From this data, it is possible to draw an Arrhenius plot, from which one obtains the apparent capture cross-section σ_a and the position of the energy level in the band gap, E_T. These two quantities are collectively known as the defect's *signature*, which can help to identify the defect. A DLTS measurement can also reveal other

properties of the defect such as its depth distribution and introduction rates, as well as metastability and annealing properties.

The standard DLTS technique makes use of a lock-in amplifier (LIA) to analyse the signal from the sample. However, with modern technology it has become possible to digitise the signal and analyse it numerically. Digital data analysis has a number of advantages over the older analogue method: Firstly, because no repetitive signal is required, it is possible to analyse much slower transients that would otherwise take unreasonably long in an LIA system. Secondly, in principle only a single transient is required to do a complete analysis over the whole frequency range – this allows for much faster data acquisition and the recording of "single shot" events as are observed with metastable defects. Thirdly, the digital data analysis technique allows much more advanced data analysis to be performed. This technique would allow the resolution of the DLTS system, which is inherently limited with an LIA-based DLTS system, to be improved using inverse Laplace transforms and other deconvolution techniques (see, for instance Dobaczewski, 1994 or Istratov, 1997).

In this thesis, the design and construction of a digital, isothermal DLTS system is discussed. The system has been evaluated firstly by measuring a number of "standard" defects that have been well described in the literature and secondly by using it to analyse a number of defect phenomena that would not be observable by a standard LIA-based system. The results of these measurements are discussed and some publications, in which these techniques have been used, are included.

In Chapters 2 and 3, the general theory of defects and deep-level transient spectroscopy is discussed. The discussion is not intended to be a complete study, but rather to highlight a number of topics, which will be referred to at a later stage and to define nomenclature and notation that will be used in the rest of the thesis. In Chapter 4 the design and characterisation of the digital DLTS system is discussed, while Chapter 5 describes the general experimental procedures that were followed. The experimental results are presented in Chapters 6 to 9. The experimental chapters consist of an introduction describing the basic experiment and theoretical background, followed by more detailed experimental procedure and results. Where applicable, a copy of published papers containing the discussed results and conclusions, have been included at the end of the chapter.

Chapter 10 contains general conclusions and suggestions for further research.

2

Some concepts in semiconductor physics

The properties of semiconductors are adequately described in a number of textbooks. For this reason only a short description of the aspects of semiconductor physics that are relevant to this study is given. The main aim is to familiarise the reader with the terminology and the notation used in this thesis. For a more complete introduction to the properties of semiconductors, the reader is referred to textbooks e.g. Ridly (1988) , Sze (1981), Smith (1978), and Henisch (1989).

2.1 Metal-semiconductor junctions

A number of early researchers have noted that the current flowing through a metal–semiconductor junction depends on the polarity of the applied voltage. This effect was researched further and later used in point contact rectifiers. Currently, metal-semiconductor junctions are important because they are used in devices as well as tools in the analysis of physical parameters of semiconductors. For this reason, metal-semiconductor junctions have been studied extensively.

A number of models have been suggested to explain how these junctions operate. In this chapter, the model proposed by Schottky (1942) will be discussed in more detail. This model describes an ideal case, where the metal and the semiconductor are in intimate contact, without the presence of any interfacial layer or interface states. The Bardeen model describes a more general case where the effects of an interfacial layer and interface states are taken into account (Bardeen, 1947 and Rhoderick, 1988).

2.1.1 The Schottky model

When a metal contact is evaporated onto the surface of a semiconductor, a potential barrier is formed at the metal–semiconductor interface. Here, only the case for an *n*-type semiconductor will be considered. The formation of a Schottky barrier on *p*-type material occurs similarly.

2.1.2 The ideal case

Figure 2.1 graphically illustrates the formation of a Schottky barrier. Part (a) illustrates the metal and the semiconductor in their isolated, electrically neutral states. Here χ_s is the electron affinity of the semiconductor. (The electron affinity of a substance is the energy released when an electron is added to the material – i.e. in this case the difference between the vacuum level and the conduction band edge.) ϕ_m and ϕ_s are the work functions of the metal and the semiconductor respectively. (The work function of a material is the energy required to remove an electron from the material to the vacuum level – i.e. the difference between the vacuum level and the Fermi level.) Here we only consider the case where the work function of the metal is greater than that of the semiconductor, which, in practice, is the most important case. This relationship between the two work functions causes the Fermi level of the metal to be lower than that of the semiconductor, and leads to the formation of a contact with rectifying properties.

Now, if the metal and the semiconductor were connected by means of a thin wire, electrons would flow from the semiconductor to the metal due to the difference in work function. Because of this flow of electrons, a positive charge builds up on the surface of the semiconductor, while a negative charge builds up on the surface of the metal, causing an electric field in the gap between the metal and the semiconductor. This electric field opposes the flow of electrons. The equilibrium condition is reached when the Fermi levels of the two materials coincide. This implies that the potential difference between the metal and the bulk of the semiconductor is equal to the difference in their Fermi levels.

The negative charge that builds up on the surface of the metal is caused by extra electrons that are accommodated within the Thomas-Fermi screening distance of about 0.5 Å, i.e. within the first atomic layer. In the semiconductor, the positive charge is caused by the removal of electrons. However, the only electrons close to the Fermi level that can be removed are those in the conduction band, which are provided by the ionised donor atoms. Thus, the positive charge in the semiconductor is provided solely by the uncompensated donor atoms, left after electrons have flowed from the conduction band.

The concentration of these donor atoms is much lower than the concentration of electrons in the metal. This means that electrons are depleted from the conduction band up to an appreciable depth, *w*. For carrier densities of 10^{16} cm^{-3} the thickness of this so-called depletion layer, is generally in the order of a micron. Because the charge in the depletion region is distributed over a finite distance, the potential changes slowly over the depletion region, and causes the bands to bend upwards as shown in Figure 2.1(b).

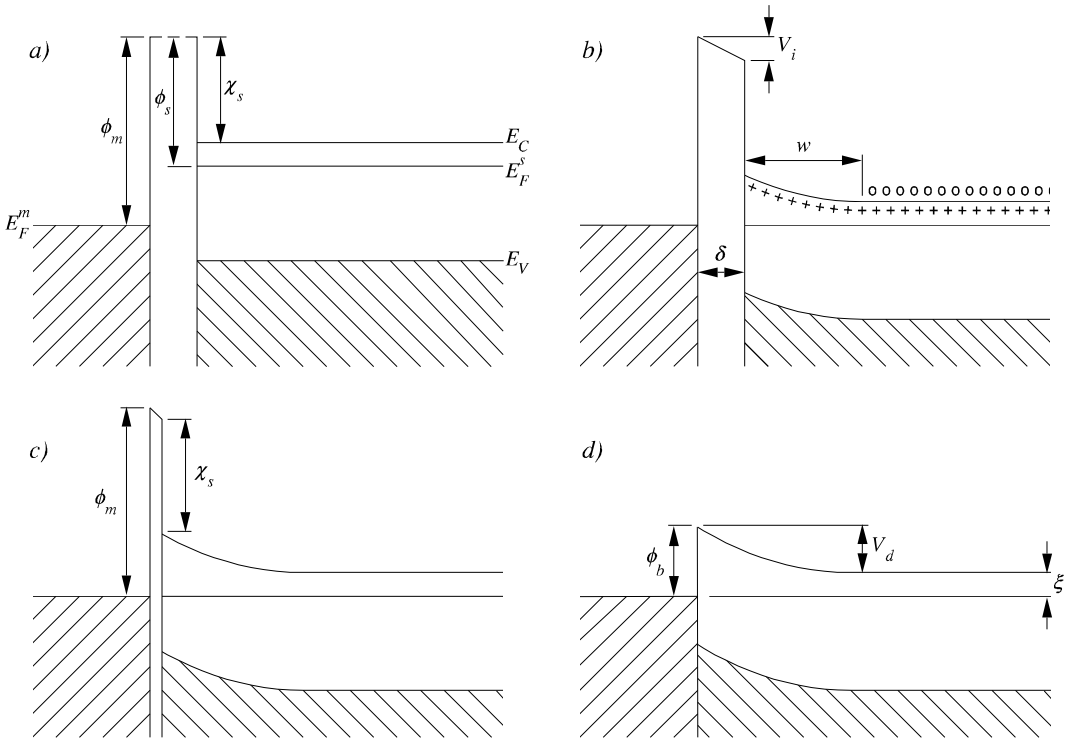

Figure 2.1 *The forming of a Schottky barrier. a) The metal and the semiconductor in their isolated states, b) electrically connected, c) separated by a narrow gap, d) in perfect contact. (After Rhoderick, 1988.)*

The difference between the electrostatic potentials at the surfaces of the metal and the semiconductor is given by $V_{\mathrm{i}} = \delta E_{\mathrm{i}}$, where δ is the distance between the metal and the semiconductor, and E_{i} is the electric field in the gap. As the gap, δ, is decreased, the electric field stays finite [Figure 2.1(c)], and causes V_{i} to tend towards zero as the gap disappears. When ideal contact is made, the barrier due to the vacuum disappears completely [Figure 2.1(d)], and the only barrier seen by electrons, is that caused by the bending of the bands in the semiconductor. The height of this barrier measured relative to the Fermi level is given by

$$\phi_{\mathrm{b}} = \phi_{\mathrm{m}} - \chi_{\mathrm{s}} \,. \tag{2.1}$$

The height of the barrier relative to the position of the conduction band in the neutral region of the semiconductor is called the diffusion potential (also called the built-in voltage), and is indicated by V_d. From Figure 2.1(d) it is clear that, under zero bias conditions

$$V_{\mathrm{d}} = \phi_{\mathrm{b}} - \xi \,, \tag{2.2}$$

where ξ is the energy difference between the Fermi level and the conduction band in the neutral semiconductor. From charge neutrality, it can be shown that (Sze, 1981)

$$\xi = kT \ln \frac{N_{\mathrm{C}}}{N_{\mathrm{D}}} \,, \tag{2.3}$$

where N_C is the density of states in the conduction band of the semiconductor and N_D is the doping density.

In practice, it is difficult to fabricate Schottky diodes by conventional vacuum deposition without a thin insulating layer of oxide about 10 to 20 Å thick forming on the surface of the semiconductor. This layer is often referred to as the interfacial layer. A practical Schottky diode is therefore better represented by Figure 2.1(c). The interfacial layer is usually very thin, so that electrons can easily tunnel through it, causing this case to be almost indistinguishable from the ideal case illustrated in Figure 2.1(d). Furthermore, the potential drop V_i is so small that Equation (2.1) remains a reasonable approximation.

In this discussion, we have made a number of assumptions that are not always valid. For example, we have neglected the effect of interface states. For a more complete discussion on other aspects influencing the barrier height, the reader is referred to Cowley (1965) and Rhoderick (1988).

2.1.3 Behaviour of the barrier under forward and reverse bias

When a bias is applied across the barrier, the relationship between the Fermi levels in the semiconductor and the metal is changed. Under zero bias conditions, the electrons from both sides of the junction “see” the same barrier height relative to their Fermi energy. As a result, there is no net flow of electrons over the barrier in the one or the other direction.

However, if a forward bias is applied (i.e. a positive potential is applied to the metal), the position of the Fermi level in the semiconductor is raised relative to that of the metal. This decreases the amount of band bending, causing electrons in the semiconductor to “see” a lower barrier than those in the metal. This causes a net flow of electrons from the semiconductor to the metal. As the forward bias is increased, the barrier presented to the electrons decreases, causing an increase in the current flowing over the junction.

Under reverse bias, the Fermi level of the semiconductor is lowered relative to that of the metal, causing more band bending and an increase in the barrier seen by electrons in the semiconductor. This also increases the width of the depletion region. The barrier experienced by electrons from the metal, however, stays constant. Thus, the current from the metal to the semiconductor stays constant, as the current from the semiconductor to the metal decreases. This causes the current under reverse bias to tend toward a limit as the reverse bias is increased. This continues until the electric field in the depletion region is large enough to cause dielectric breakdown of the semiconductor, leading to a large current flowing across the barrier. This could cause irreversible damage to the device. For a detailed discussion on current transport mechanisms, see Rhoderick (1988) or Sze (1981).

From the discussion in the previous section, it follows that the relationship between V_d and the bias applied to the diode, V_D, can be written as

$$V_d = \phi_b - \xi - V_D \,. \tag{2.4}$$

2.1.4 Calculation of the electric field in a Schottky barrier

The shape of the band edge profiles can be calculated by solving Poisson's equation, subject to certain boundary conditions. The first boundary condition is obtained from the barrier height, while the second is that there is no electric field in the bulk of the semiconductor. By choosing $x = 0$ at the interface, the boundary conditions can be written as $V(0) = V_{\mathrm{d}}$ and $E(\infty) = 0$. These relationships serve as boundary conditions for the solution of Poisson's equation in the semiconductor, which can be written in the one-dimensional case as

$$\frac{d^2V}{dx^2} = \frac{1}{\varepsilon_{\mathrm{s}}}\rho(x), \tag{2.5}$$

where $\rho(x)$ is the total charge density in the semiconductor at a depth x and ε_{s} is the permittivity of the semiconductor. In general, contributions from the valence band, the conduction band, ionised donors and acceptors and deep levels in the band gap should be taken into account. This however leads to a very complicated equation that can only be solved numerically. The equation can be simplified by making use of the depletion approximation.

According to the abrupt or depletion approximation, it is assumed that it is possible to divide the semiconductor into two regions: the depletion region, directly below the metal, which is devoid of free carriers, and the bulk of the semiconductor, which is electrically neutral, and in which no electric field exists. In the depletion region, where there are no electrons in the conduction band, the charge density, $\rho(x)$ is qN_{D}. If the width of the depletion region is w, the charge density in the semiconductor can be written as

$$\rho(x) = \begin{cases} qN_{\mathrm{D}} & \text{if } x \le w \\ 0 & \text{if } x > w \end{cases}. \tag{2.6}$$

By integrating Equation (2.5) twice, and applying the boundary conditions, the width of the depletion region can be obtained as

$$w = \sqrt{\frac{2\varepsilon_{\mathrm{s}}V_{\mathrm{d}}}{qN_{\mathrm{D}}}}, \tag{2.7}$$

while the electric field and potential in the depletion region are given by

$$E(x) = -\frac{qN_{\mathrm{D}}(w-x)}{\varepsilon_{\mathrm{s}}} \tag{2.8}$$

and

$$V(x) = -\frac{qN_{D}}{2\varepsilon_{\mathrm{s}}}(w-x)^2. \tag{2.9}$$

Figure 2.2 shows a graph of $\rho(x)$, $E(x)$ and $V(x)$ for a typical Schottky barrier.

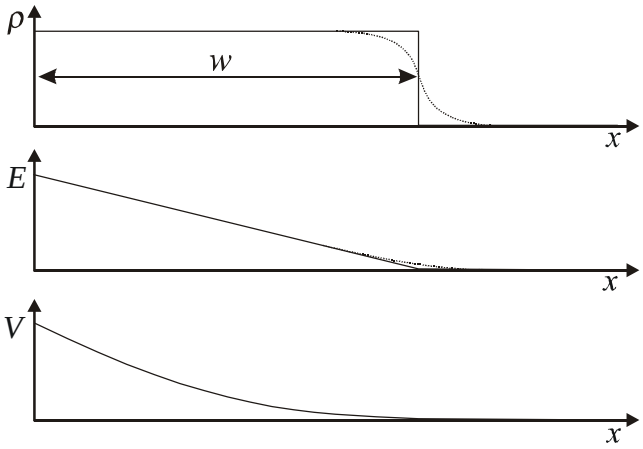

Figure 2.2 *Graphs of the charge density ρ, electric field E, and electrostatic potential V in the depletion region of a Schottky diode. The solid line indicates the results according to the depletion approximation, while the dashed line indicates the effect of a non-zero Debye length.*

The charge per unit area in the depletion region is now

$$Q_{\mathrm{d}} = qwN_{\mathrm{D}} = \sqrt{2q\varepsilon_{\mathrm{s}}N_{\mathrm{D}}V_{\mathrm{d}}}\,, \tag{2.10}$$

from which it follows that the (differential) capacitance per unit area of the diode is

$$C = \frac{\partial Q_{\mathrm{d}}}{\partial V_{\mathrm{d}}} = \sqrt{\frac{\varepsilon_{\mathrm{s}}qN_{\mathrm{D}}}{2V_{\mathrm{d}}}} = \frac{\varepsilon_{\mathrm{s}}}{w}\,. \tag{2.11}$$

In practice, this capacitance is measured by superimposing a small oscillating voltage ΔV_{osc} on the applied bias and measuring the current due to the voltage. The capacitance is then calculated from the relation $C = \Delta Q / \Delta V$. Since the properties of a Schottky diode are highly non-linear, it is important that ΔV_{osc} is small compared to the applied bias, so as not to influence the measurement.

It should be noted that the depletion region approximation is exactly that – an approximation. In reality, the transition between the depletion region and the bulk is not abrupt, but consists of a gradual transition region, as shown by the dashed line in Figure 2.2. In this transition region the potential decreases approximately exponentially with a decay constant L_{D}, called the Debye length Jackson (1975):

$$L_{D} = \sqrt{\frac{kT\varepsilon_{\mathrm{s}}}{q^{2}n}}\,, \tag{2.12}$$

where n is the carrier concentration in the semiconductor. The effects of a non-zero Debye length are particularly important when the depletion region edge is used to measure depth profiles, where the depth resolution of the technique is limited by the Debye length.

2.2 Defects and deep levels in semiconductors

The band structure of semiconductors is generally calculated for an ideal crystal (i.e. one that contains an infinite number of repetitions of the unit cell without any deviations) at 0 K. In reality, all materials contain some chemical impurities or lattice defects. Such an interruption in the lattice periodicity of a crystal is called a defect. These defects can be classified as point defects in which the perturbation of the lattice remains localised (e.g. vacancies, interstitials, substitutions) or extended defects (dislocations, surfaces, grain boundaries, voids, cavities). Since small aggregates of several point defects (e.g. divacancies, vacancy–donor complexes etc.) also cause only a local perturbation of the lattice, they are generally considered as point defects as well.

Since the periodicity of the crystal lattice is an important factor determining the band structure of the solid, one can expect that a defect will in some way influence the eigenvalues of the Schrödinger equation. Many of these defects cause bound states to appear in the forbidden energy gaps of the perfect crystal. These bound states have wave functions that decrease exponentially away from the defect. Except for numerical techniques, there is no general theory for calculating the energy levels of these bound states, but a number of approximations apply in different limiting cases.

The states in the forbidden band gap can broadly be classified into “shallow” and “deep” states. The shallow states are close to the edges of the forbidden band and can be described using the effective mass theory for which the bound-state equation reduces to a hydrogenic Schrödinger equation. On the other hand, deep level defects, which lie closer to the middle of the band gap, are better described by the tight binding approximation. According to this approximation, the eigenstates of the bound electrons are expressed as a linear combination of the free-atom eigenstates. This method is frequently referred to as the linear combinations of atomic orbitals (LCAO) method. The main advantage of the LCAO method is that it is relatively simple but none the less gives a qualitatively correct description of many experimental observations. For a detailed description of these and other methods, see Lannoo (1981), Jaros (1982) or Ridley (1988).

2.2.1 Emission and capture of carriers from defects

Defect states in the band gap can influence the properties of a semiconductor in a number of ways. Except for behaving as donors or acceptors, defect states may also influence the mobility of charge carriers by scattering, and cause various features in the optical absorption and emission spectrum of the semiconductor. The most important electrical effect of deep levels in the band gap of a semiconductor is the emission and capture of charge carriers. These processes cause various transient effects and cause defects to act as recombination and trapping centres, influencing the carrier lifetimes in semiconductors.

The kinetics of emission and capture of carriers from defect levels has been discussed extensively in the literature, see Shockley (1952), Hall (1952) and Bourgoin (1983). In this section, the case of a single level with two charge states in a non-degenerate semiconductor will be discussed, similarly to the approach followed by Bourgoin (1983).

Consider a defect with two charge states *S* and *B*, where in the *S* state the defect contains one more electron than in the *B* state. The notation e_n, e_p, k_n and k_p will be used for the probabilities for emission (e) and capture (k) of electrons (n) and holes (p).

If one assumes that there is no barrier that the electron has to overcome during the capture process, the probability per unit time, k_n, that a defect in state *B* captures an electron from the conduction band can be written as

$$k_n = c_n n = \sigma_n v_{th,n} n , \tag{2.13}$$

where c_n is the electron capture coefficient of the defect, σ_n is the electron capture cross section of the defect, $v_{th,n}$ is the thermal velocity of the electrons in the conduction band and n is the concentration of the electrons in the conduction band.

A similar equation can be written for holes:

$$k_p = c_p p = \sigma_p v_{th,p} p , \tag{2.14}$$

where p is the concentration of holes in the valence band.

If the carrier concentration is much less than the density of states in the conduction and valence bands, the number of empty states in the conduction and valence band is approximately independent of the carrier concentration. Therefore, it may be assumed that the emission rates e_n and e_p are independent of the carrier concentration. Now, if s and b are the concentration of defects in state *S* and *B* respectively, the rates for emission and capture of holes and electrons are given by:

$k_n s = c_n n s$	electron capture
$e_n b$	electron emission
$k_p b = c_p p b$	hole capture
$e_p s$	hole emission

(2.15)

At thermal equilibrium, the capture rates for each species should be equal to its emission rate, i.e. $c_n n^0 s^0 = e_n b^0$ and $c_p p^0 b^0 = e_p s^0$, where the superscript (^{0}) indicates values at thermal equilibrium. It is now possible to solve for e_n and e_p, giving

$$e_n = c_n n^0 \frac{s^0}{b^0} = \sigma_n v_{th,n} n^0 \frac{s^0}{b^0} \tag{2.16}$$

and

$$e_p = c_p p^0 \frac{b^0}{s^0} = \sigma_p v_{th,p} p^0 \frac{b^0}{s^0} . \tag{2.17}$$

At thermal equilibrium, the ratio between the concentrations of the two charge states of the defect is

$$\frac{s^0}{b^0} = \gamma \exp\left(\frac{E_T - E_F}{kT}\right), \tag{2.18}$$

where γ is a degeneracy factor equal to $Z(\mathrm{S})/Z(\mathrm{B})$. Furthermore, at thermal equilibrium the carrier densities are Bourgoin (1983)

$$n^0 = N_\mathrm{C} \exp\left(\frac{E_\mathrm{F} - E_\mathrm{C}}{kT}\right) \tag{2.19}$$

and

$$p^0 = N_\mathrm{V} \exp\left(\frac{E_\mathrm{V} - E_\mathrm{F}}{kT}\right). \tag{2.20}$$

Substituting Equation (2.18) into Equations (2.16) and (2.17), and using Equations (2.19) and (2.20), it follows that

$$e_\mathrm{n} = \sigma_\mathrm{n} v_{\mathrm{th,\,n}} \gamma N_\mathrm{C} \exp\left(-\frac{E_\mathrm{C} - E_\mathrm{T}}{kT}\right) \tag{2.21}$$

and

$$e_\mathrm{p} = \frac{\sigma_\mathrm{p} v_{\mathrm{th,\,p}} N_\mathrm{V}}{\gamma} \exp\left(-\frac{E_\mathrm{T} - E_\mathrm{V}}{kT}\right). \tag{2.22}$$

Assuming a Boltzmann distribution, the thermal velocity of electrons in the conduction band can be written in terms of their effective mass m_e^* (see, for instance Mandl, 1988)

$$v_{\mathrm{th,\,n}} = \left(\frac{8kT}{\pi m_\mathrm{e}^*}\right)^{1/2} \tag{2.23}$$

and the density of states in the conduction band N_c is

$$N_c = \frac{1}{\sqrt{2}}\left(\frac{m_e^* kT}{\pi\hbar^2}\right)^{3/2}. \tag{2.24}$$

By substituting Equation (2.23) and (2.24) into Equation (2.21), the emission rate can be written as

$$e_\mathrm{n} = \frac{2}{\pi^2\hbar^3}\frac{\sigma_\mathrm{n} m_\mathrm{e}^* k^2 T^2}{g} \exp\left(-\frac{E_\mathrm{C} - E_\mathrm{T}}{kT}\right). \tag{2.25}$$

Here, in agreement with the more common notation (see, for instance Miller, 1977), the degeneracy factor γ used by Bourgoin (1983) has been replaced by $1/g$, where g is the degeneracy of the defect level.

If it is assumed that the capture cross-section of the defect is independent of temperature, it follows that an Arrhenius plot of $\ln(e_\mathrm{n}/T^2)$ as a function of $1/T$ should yield a linear relationship from which the defect's energy E_T and capture cross-section σ_n may be calculated. These two values are frequently

referred to as the defect's signature. The defect signature is one of the important parameters used to identify a defect during electrical measurements.

Note, however, that the capture cross-section calculated from an Arrhenius plot is subject to a number of assumptions, for example, that the capture cross-section of the defect is not temperature dependent. Therefore, the capture cross-section calculated from the Arrhenius plot is frequently referred to as the *apparent* capture cross-section and indicated by $\sigma_{\mathrm{n,a}}$ in order to distinguish it from the capture cross-section determined by more direct means. For the same reason the energy level of the defect calculated from the Arrhenius plot, might differ from values obtained under different conditions or by other techniques. The differences between values obtained using different techniques, might give important information about the nature of the defect involved.

2.2.2 Defect occupation as a function of time

Many experiments measure the emission and capture of defects after the equilibrium concentration has been disturbed in some way. Consider a semiconductor containing a single deep level with a concentration N_{T}. The concentration of occupied defects is N. Due to the emission and capture of carriers, the concentration of occupied defect will change according to

$$\frac{\mathrm{d}N}{\mathrm{d}t} = (c_{\mathrm{n}} + e_{\mathrm{p}})(N_{\mathrm{T}} - N) - (c_{\mathrm{p}} + e_{\mathrm{n}})N \,. \tag{2.26}$$

The general solution to this differential equation is

$$N(t) = N(\infty) + [N(0) - N(\infty)]\exp[-(c_{\mathrm{n}} + e_{\mathrm{p}} + c_{\mathrm{p}} + e_{\mathrm{n}})t], \tag{2.27}$$

where $N(\infty)$ is the equilibrium concentration of the occupied defect for which $\mathrm{d}N/\mathrm{d}t = 0$ and is given by

$$N(\infty) = \frac{c_{\mathrm{n}} + e_{\mathrm{p}}}{c_{\mathrm{n}} + e_{\mathrm{p}} + c_{\mathrm{p}} + e_{\mathrm{n}}} \,. \tag{2.28}$$

It is often helpful to divide defects into two classes, namely minority and majority carrier traps. Majority carrier traps are defects for which the thermal emission rate for majority carriers e_{maj} is much greater than the thermal emission rate for minority carriers e_{min}. For a minority carrier trap, the opposite is true, i.e. $e_{\mathrm{min}} \gg e_{\mathrm{maj}}$. The terms *electron* trap and *hole* trap are frequently used to distinguish defects for which $e_{\mathrm{n}} \gg e_{\mathrm{p}}$ and $e_{\mathrm{p}} \gg e_{\mathrm{n}}$, respectively. Clearly, an electron trap in an *n*-type semiconductor is a majority carrier trap, while an electron trap in a *p*-type semiconductor would be a minority carrier trap.

In thermal capture and emission experiments, usually only one of the emission rates dominates the kinetics, so that Equation (2.27) may be simplified considerably. For example, for an electron trap in the depletion region, the emission rate e_{n} dominates all the other emission and capture rates, so that defect concentration as a function of time is given by

$$N(t) = N_{\mathrm{T}} \exp(-e_{\mathrm{n}}t) \,. \tag{2.29}$$

2.2.3 Field dependence of the emission rate

In Section 2.1.4, it was mentioned that an electric field exists in the depletion region of a Schottky diode. This field may be quite large, almost up to the dielectric breakdown field of the semiconductor ($\sim 10^7$ V/m). If a defect is placed in the depletion region of a Schottky diode, it will also be subject to the field, which will distort the shape of its potential well. This distortion of the potential well may enhance the emission probability of a carrier trapped in the well. The extent of this enhancement depends, amongst others, on the shape and dimensions of the potential well. A few enhancement mechanisms will be discussed briefly in the following sections.

2.2.3.1 The Poole-Frenkel effect

The simplest mechanism according to which emission of an electron from a potential well may be enhanced is the Poole-Frenkel effect. When an external field is applied to an electron trapped in a potential well, the electron is subjected to the sum of both fields. This causes the shape of the potential well to be distorted, thus raising the barrier on the one side of the defect and lowering it on the other (see Figure 2.3).

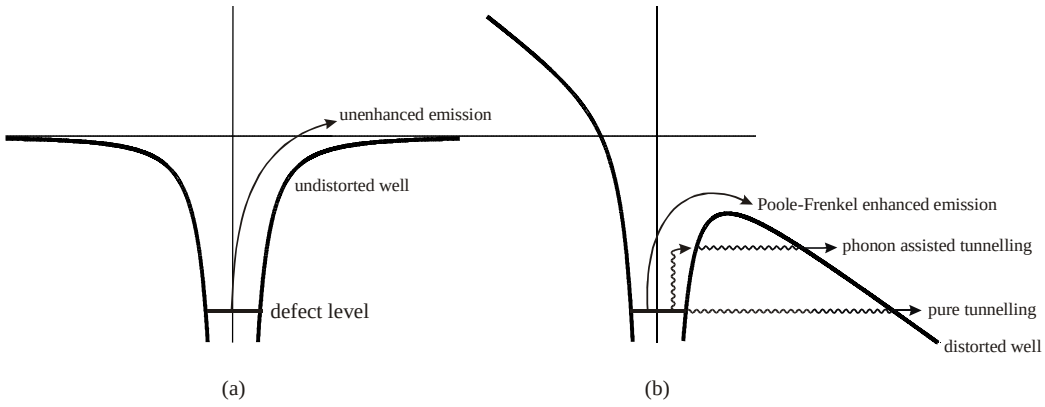

Figure 2.3 *The distortion of a coulombic well by an electric field. (a) The undistorted (zero-field) coulombic well and (b) the coulombic well in a constant, external electric field. A number of emission mechanisms are indicated schematically.*

The original theory, as developed by Frenkel (1938) deals with the one-dimensional case only. According to the one-dimensional model, the ionisation energy of a coulombic well placed in an electric field F, is lowered by

$$\Delta E_T = \sqrt{\frac{qF}{\pi\varepsilon}}\,. \tag{2.30}$$

When substituted in Equation (2.21), this implies that the emission rate of the defect is now given by

$$e(F) = e(0)\exp\left(\frac{1}{kT}\sqrt{\frac{qF}{\pi\varepsilon}}\right), \tag{2.31}$$

where $e(0)$ is the emission rate at zero electric field, k is Boltzmann's constant, T is the absolute temperature.

However, the one-dimensional model over-estimates the emission enhancement. Hartke (1968) developed the theory for a three-dimensional well, according to which the emission rate from a three-dimensional coulombic well can be described by:

$$e(F) = e(0)\left\{\left(\frac{kT}{\beta\sqrt{F}}\right)^2\left[1 + \left(\frac{\beta\sqrt{F}}{kT} - 1\right)\exp\left(\frac{\beta\sqrt{F}}{kT}\right)\right] + \frac{1}{2}\right\} \tag{2.32}$$

where

$$\beta = \left(\frac{q^3}{\pi\varepsilon}\right)^{\frac{1}{2}}. \tag{2.33}$$

The emission enhancement due to the Poole-Frenkel effect is frequently used by experimentalists to estimate the range of the defect potential. A longer range potential (e.g. a coulombic well) would show a far stronger Poole-Frenkel enhancement than a shorter range potential.

The characteristic dependence of the emission rate (e) on electric field (F) in the case of the one-dimensional Poole-Frenkel effect for a coulombic well, namely that log e is proportional to $F^{1/2}$, has been used as experimental evidence to distinguish between donor and acceptor defects. The linearity of this dependence is characteristic of a charge leaving a centre of opposite sign. In n-type material this would imply a donor type defect, whereas, in p-type material this would imply an acceptor type defect (Bourgoin, 1983).

2.2.3.2 Phonon-assisted tunnelling

The field-enhanced emission due to the Poole-Frenkel effect is generally relatively small. Some defects, however, show a much stronger field enhanced emission. This strong field enhanced emission may be explained by tunnelling mechanisms. The two mechanisms discussed here are "pure" tunnelling and phonon-assisted tunnelling, with the pure tunnelling mechanism being predominant in the high field regions (>10^8 V m^{-1}).

The phonon assisted tunnelling mechanism is observed in defects with a significant electron–lattice coupling. Due to this coupling, a trapped electron can occupy a set of stationary quasi levels separated by $\hbar\omega$, with $\hbar\omega$ being the phonon energy. Elastic tunnelling can then occur from any of these quasi deep levels to the conduction band. The coupling constant or Huang-Rhys factor S (Makram-Ebeid, 1980) is represented by

$$S = \frac{\Delta E}{\hbar\omega}, \tag{2.34}$$

where ΔE is the vibrational energy loss. The field emission rate due to phonon assisted tunnelling emission as derived by Pons (1979) is given by

$$e_f = \sum_p \Pi_p \Gamma(\Delta_p).(1 - f_{1,p}) \,. \tag{2.35}$$

The $(1 - f_{1,p})$ factor in the equation is the Fermi-Dirac probability of finding an empty conduction band state, $\Gamma(\Delta_p)$ is the tunnelling emission probability for an electron at a quasi level *p* with an energy Δ_p above the ground state and Π_p is the probability of finding the electron at quasi level *p*.

The tunnelling probability $\Gamma(\Delta_p)$ was calculated by Korol (1977) for an electron trapped in a delta function potential well as

$$\Gamma(\Delta) = \gamma \frac{\Delta}{qK} e^K \,, \tag{2.36}$$

where Δ is the energy position of the deep level below the conduction band and *K* is the WKB attenuation of the wave function across the potential barrier separating the trapping site from the free conduction band states. The pre-exponential factor γ is equal to $q/3\hbar$. Assuming a uniform field *F* and a triangular barrier, *K* is given by

$$K = \frac{4}{3} \frac{\sqrt{2m^*}}{\hbar F} \Delta^{3/2} \,, \tag{2.37}$$

where m^* is the electron effective mass.

The probability Π_p of finding an electron at a given quasi level $E_c - \Delta_p$, where $p = 0, \quad \pm 1, \quad \pm 2, \ldots$, may be calculated from

$$\Pi_p = (1 - e^{\hbar\omega/kT}) \sum_{n=0}^{\infty} e^{n\hbar\omega/kT} J_p^2 \left(2\sqrt{S\left(n + \tfrac{1}{2}\right)} \right) , \tag{2.38}$$

where J_p is a Bessel function of the first kind and *n* the integer number of phonons. This model is based on the assumption that the phonons have a single, well-defined angular frequency (ω).

In practice, the theoretical model can be fitted to experimental emission rate vs. electric field data recorded at different temperatures in order to obtain experimental values for the parameters *S* and γ.

3

DLTS: Deep level transient spectroscopy

Deep levels in semiconductors influence both the electrical and the optical properties of the material. There are a number of optical techniques for the characterisation of deep level defects in semiconductors. However, one of the main shortcomings of these techniques is that they cannot measure or predict the electrical properties. Since most semiconductor applications rely on the electrical properties of the semiconductor, it is important to know the electrical properties of a deep level defect. Furthermore, many of the processes that occur in deep levels that influence device performance are nonradiative, and cannot be observed by optical techniques. Deep level transient spectroscopy (DLTS) is one of the most versatile techniques used to determine the electrical properties of defects.

3.1 The DLTS technique

As described by Lang (1974), the DLTS technique uses a fast, sensitive capacitance meter to measure the capacitance of a reverse-biased Schottky, MOS or *p-n* junction. According to Equation (2.11), the capacitance of a reverse-biased diode can be related to the width of the depletion region, which in turn depends on the charge in the depletion region, due to dopants as well as deep levels. The DLTS technique measures the change in the capacitance of the junction due to the emission of carriers by defects in the depletion region, as described by Equation (2.29). By processing the capacitance signal with a weighting function, the emission rate of the defect in the depletion region is obtained.

Consider the case of a Schottky contact on an *n*-type semiconductor, as shown in Figure 3.1(A). The semiconductor contains a low concentration of a defect that causes a deep electron trap with energy E_T. In the figure the bulk of the semiconductor containing free carriers is indicated by the shaded area, while the depletion region is left unshaded. Filled and open circles indicate filled and empty traps respectively. For simplicity, we assume that, initially, all the traps in the depletion region are empty, while all the traps in the bulk of the semiconductor are filled.

At the start of the DLTS cycle, a smaller reverse bias (or even a forward bias) pulse is applied across the diode. [Figure 3.1(B)]. This bias pulse reduces the width of the depletion region, increasing the capacitance of the Schottky diode drastically. The reduction in the width of the depletion region fills the traps up to a distance of approximately the depletion width below the surface of the semiconductor.

After the filling pulse, the reverse bias is returned to its quiescent level [Figure 3.1(C)]. This increase in reverse bias increases the width of the depletion region again. However, since some of the deep level traps in the depletion region are now filled, the charge density in the depletion region is less than it was in (A), therefore the depletion region is slightly wider and the capacitance slightly lower than was the case in (A).

Since the filled traps in the depletion region are above the Fermi level, they now emit carriers by means of thermal processes, as described in Section 2.2. This causes the charge density in the depletion region to increase, reducing its width and increasing the capacitance of the junction.

If it is assumed that $N_T \ll N_D$, the depletion region width will not change significantly during the emission of carriers. Under these circumstances, it is reasonable to assume that the emission of carriers from the depletion region may be described by an exponential decay, as in Equation (2.29). The capacitance of the Schottky diode is then also described by an exponential decay function

$$C(t) = C_\infty + \Delta C e^{-\lambda t}, \tag{3.1}$$

where λ is the decay rate and C_∞ is the steady state capacitance of the diode.

If it is assumed that all the defects from the depletion region edge to the interface are filled by the filling pulse and subsequently emptied, the defect concentration may be calculated from the amplitude of the exponential decay function by applying Equation (2.11)

$$N_T \approx 2N_D \frac{\Delta C}{C}. \tag{3.2}$$

It is possible to obtain an activation energy and a capture cross-section associated with the emission of the carriers from the defect by measuring the decay time constant as a function of temperature, as described in Section 2.2.1.

In the above explanation, it has been assumed that the defect level is empty in the depletion region and full in the bulk. Since the defect level typically lies much deeper in the band than the dopant level, the defect level intersects the Fermi level a distance λ shallower than the depletion region edge, as shown in Figure 3.2.

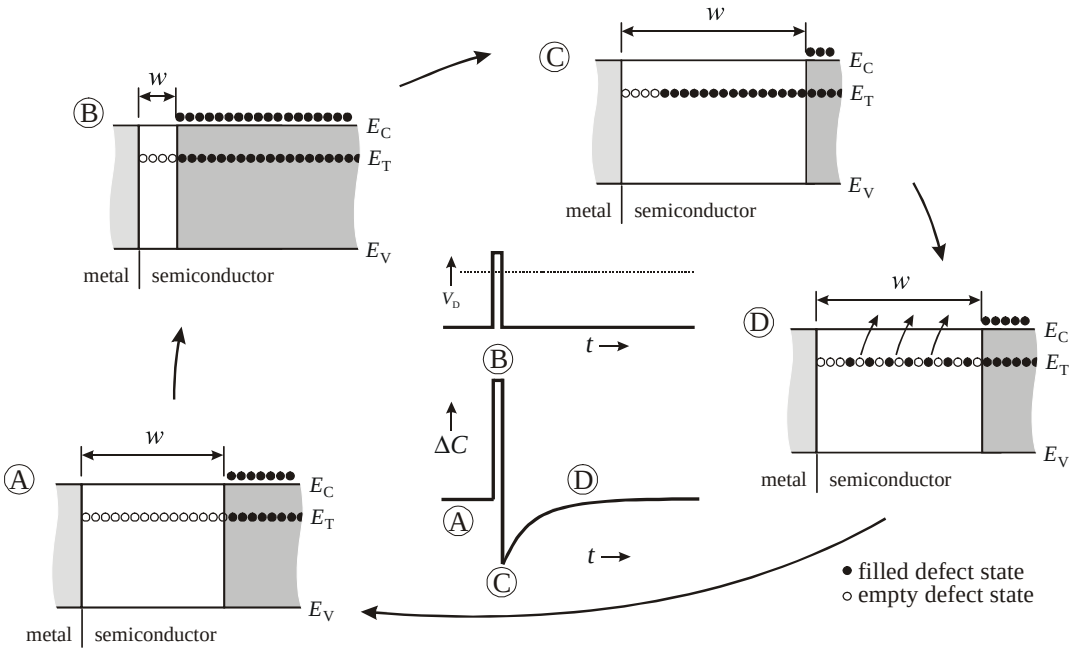

Figure 3.1 *A schematic illustration describing the origin of the DLTS transient. (A): Quiescent state, (B): Filling pulse; (C) Reverse bias; (D) Exponential decay as carriers are emitted. The graphs in the middle show the applied bias* V_D *and the change in the capacitance of the diode* ΔC *as a function of time. (After Miller, 1977.)*

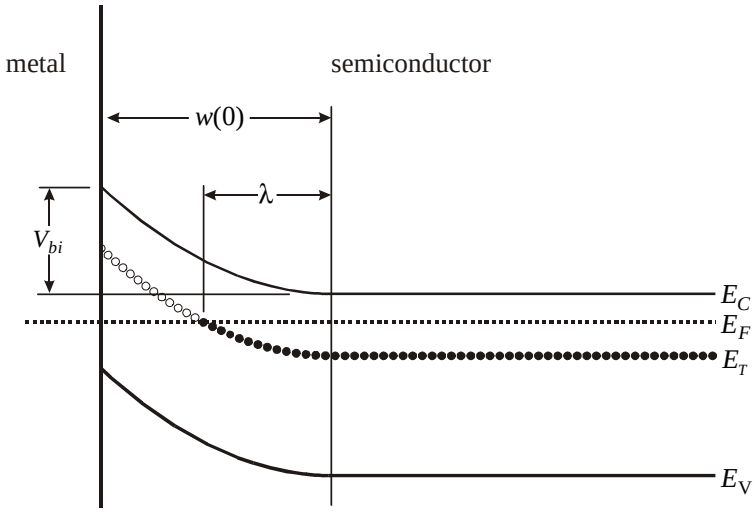

Figure 3.2 *An energy band diagram showing the relationship between the depletion region edge and the position where the defect level intersects the Fermi level.*

If a constant dopant concentration N_D is assumed, then the distance λ is independent of the width of the depletion region, and is given by

$$\lambda = \sqrt{\frac{2\varepsilon_s (E_C - E_T)}{qN_D}} \tag{3.3}$$

The result is that the DLTS measurement does not probe the region at the depletion region edge, but a region a distance λ shallower, as shown in Figure 3.3. This effect has to be taken into account when the DLTS technique is used to determine the depth profile of defects or the electric field experienced by the defects is calculated. Furthermore, during the transient, charges are removed a distance λ from the depletion region edge, therefore Equation (3.2) is not strictly valid, and a more careful analysis needs to be performed in order to obtain quantitatively correct values. DLTS depth profiling and the precautions that need to be taken are discussed in detail by Zohta (1982).

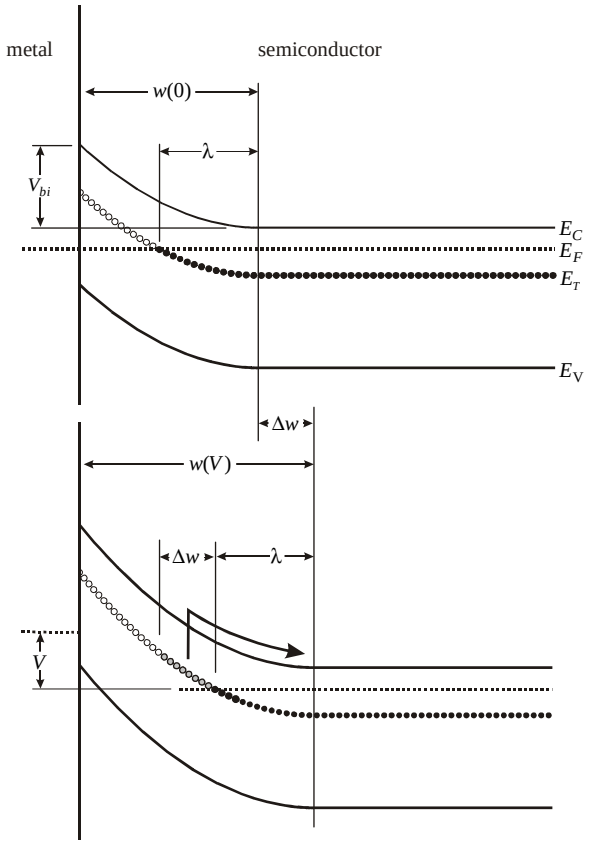

Figure 3.3 *Filling (top) and subsequent emission (bottom) of electrons from a deep level in the depletion region, assuming a constant Fermi level. In the top diagram, the filling of the defect during the filling pulse is shown. Note that due to band bending and the depth of the defect level, the defect level is filled to a depth λ shallower than the depletion region edge. After the filling pulse, the width of the depletion region increases by an amount Δw. Carriers are now emitted from a band of defects with a width Δw a distance λ shallower than the depletion region edge.*

3.2 Analysis of the DLTS transient

In the idealised case, the DLTS capacitance transient obtained from a sample with a single defect level is an exponential decay function of the form

$$C(t) = A\mathrm{e}^{-\lambda t} + C_{\infty}, \tag{3.4}$$

where A is the amplitude, λ is the decay rate and C_{∞} is the capacitance of the junction at equilibrium. Many physical processes are described by such an exponential decay process, and in principle determining the values of A, λ and C_0 is reasonably straightforward.

However, it frequently occurs that there is more than one defect level in the semiconductor and that these defects have closely spaced decay constants, or even a continuous band of decay constants. In this case, the capacitance transient can be described as the sum of a number of exponential decay functions. Many techniques have been developed for the deconvolution of such a multi-exponential function. However, there are significant problems associated with all of the techniques, and the analysis generally becomes unreliable in the presence of noise.

3.2.1 Analogue techniques

The original method used to analyse the DLTS transient was a double boxcar proposed by Lang (1974). According to this method, the DLTS signal is obtained by subtracting the capacitance measured at time t_2 from the capacitance at time t_1 (both times measured relative to the filling pulse). Qualitatively the process may be described as follows: Assume that the sample is at a low temperature and therefore there is a slow transient. Because the capacitance does not change much, the DLTS signal $S = C(t_1) - C(t_2)$ is very low [Figure 3.4(a)(i)]. As the temperature is increased, the decay rate of the transient increases causing a greater change in the capacitance between times t_1 and t_2. Therefore the DLTS signal increases as the temperature is increased [Figure 3.4(a)(ii – v)]. This increase in the DLTS signal continues until the transient decays so fast that most of the decay occurs before t_1. A further increase in temperature will now decrease the DLTS signal [Figure 3.4(a)(vi – x)]. When the DLTS signal is plotted as a function of the temperature, as in Figure 3.4(b), a peak is observed. The expression for the time constant at which the maximum in the DLTS signal is observed is easily derived, and depends on the values of t_1 and t_2:

$$\lambda_{\max} = \frac{\ln(t_2 / t_1)}{t_2 - t_1}. \tag{3.5}$$

Because the capacitance transient is very small, it is important to minimise the effect of noise on the measurements. For this reason, the capacitance measurements are usually averaged over a number of transients and, instead of taking a single point, the average capacitance values for an interval around t_1 and t_2 are taken.

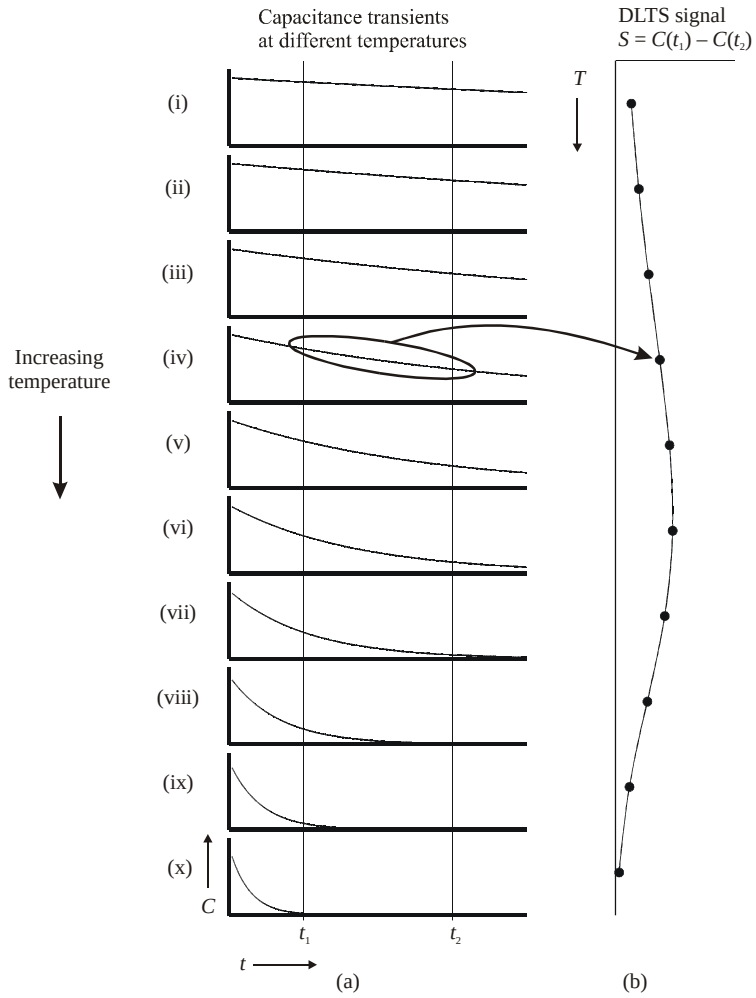

Figure 3.4 *(a) The change in the shape of a DLTS transient with increasing temperature and (b) the DLTS signal obtained from the transients plotted as a function of sample temperature. (After Lang, 1974)*

In most modern analogue DLTS systems, a lock-in amplifier is used to analyse the DLTS transient. In this arrangement, the transient is convoluted with a sine wave of a fixed frequency according to

$$S(\tau) = \frac{1}{\tau}\int_0^{\tau} C(t)\sin\left(\frac{2\pi t}{\tau}\right)dt\,. \tag{3.6}$$

The result of this convolution is referred to as the DLTS signal and is plotted as a function of the sample temperature. The result obtained is similar to that obtained from the double boxcar method, except that since the lock-in amplifier uses more of the signal the lock-in amplifier method is less sensitive to noise than the double boxcar method. It can be shown that, for an exponential transient with a sine wave weighting function, the DLTS signal reaches a maximum when $\lambda = 1/(0.423\tau)$. It is also possible to use other weighting functions, with varying degrees of success.

As an alternative to the above method, it is possible to keep the temperature constant and rather change the frequency of the LIA. This technique is referred to as isothermal DLTS or frequency scanned DLTS (Henry, 1985). Isothermal DLTS is usually implemented using digital signal processing, where a fast analogue to digital converter (ADC) connected to a computer is used to capture and analyse the data.

Both the boxcar and lock-in amplifier techniques can be successfully implemented using a fast ADC and a computer. Using a computer to analyse the transient has the further advantage that analysis at a number of lock-in amplifier frequencies can be done simultaneously, thereby saving a considerable amount of time. Furthermore, a much wider range of emission rates (especially low emission rates) can be accessed by such systems, allowing defects to be studied over a wider temperature range. However, the main advantage of digital signal processing is that modern techniques to analyse multi-exponential decay functions such as the Gaver-Stehfest method (Istratov, 1997) and various methods for calculating numerical inverse Laplace transforms (e.g. Dobaczewski, 1994) may be used.

3.2.2 Digital processing of DLTS transients

The major shortcoming of the DLTS technique is that, even for emission from a single defect level at a single decay rate, the DLTS peaks as obtained by boxcar and LIA analysis are broad, compared to the typical spacing between defects. This is in stark contrast to optical techniques, which, especially at low temperatures, yield very sharp lines. Although the broad DLTS peaks are not a serious handicap if only a single level is present, it is difficult to accurately determine the emission rate of defects with emission rates spaced less than an order of magnitude apart when both are present in the same spectrum. In fact, analysis by more advanced techniques has shown that DLTS peaks that were previously regarded as a single peak actually consist of a number of discrete peaks that could not be observed due to the limited resolution of LIA DLTS (Dobaczewski, 1992).

Istratov (1998) compares a number of different weighting functions. Some of them reduce peak widths by almost a factor of three compared to widths obtained by LIA DLTS, but at the cost of decreasing the signal to noise ratio by more than an order of magnitude. Using weighting functions based on the Gaver-Stehfest algorithm, Istratov (1997) has shown that it is possible to decrease the peak width by almost a factor 5 (compared to a lock-in amplifier), while still keeping the signal to noise requirements of the input signal realistic.

Another approach to improve the resolution of the DLTS technique is to assume that the sample emits a spectrum of emission rates with a spectral density function $F(\tau)$, so that the capacitance transient can be written as

$$C(t) = \int_0^\infty F(\tau) e^{-t\tau}\, d\tau . \tag{3.7}$$

For the case of a single emission rate, $F(\tau)$ is a delta function $\delta(\tau - \tau_0)$, while broader peaks can also be described. The aim is to obtain the $F(\tau)$ corresponding to the measured $C(t)$. In Equation (3.7) $C(t)$ is essentially the Laplace transform of $F(\tau)$, therefore an inverse Laplace transform would be required to obtain $F(\tau)$. The calculation of inverse Laplace transforms is a well-known problem and many techniques exist to do this calculation analytically as well as numerically. However, in the case of

DLTS, a number of complications arise, that make it very hard to find $F(\tau)$. Firstly, $C(t)$ is known only over a limited interval on the positive real axis, therefore the techniques that require the function $C(t)$ to be known on the complex plane cannot be used. It is still possible to calculate $F(\tau)$ under these constraints, however, most of these techniques are extremely sensitive to noise on $C(t)$. The result is that great care has to be taken in developing such an algorithm, and the results obtained should be analysed critically. A successful DLTS system based on such an inverse Laplace transform algorithm has been described by Dobaczewski (1994).

3.3 Differential DLTS

The depth range sampled by the DLTS technique depends on the applied reverse bias and the filling pulse, which respectively determine the maximum and minimum of the depth range that is observed. By recording DLTS transients under different biasing conditions and then subtracting these transients, it is possible to observe defects that lie in a limited depth range only. Such techniques are generally used to measure defect concentration depth profiles, see Lefèvre (1977) or Zohta (1982).

However, this technique is not limited to the measurement of concentration depth profiles. As described by Equation (2.8), the electric field in the depletion region also changes with depth; therefore, defects at different depths beneath the surface experience different electric fields. Thus, by restricting the measurement to only a limited depth range, it is possible to observe the behaviour of the defect under the electric field present at that depth. By applying different bias voltages, it is possible to vary the electric field in the depletion region from approximately zero to almost the breakdown field of the semiconductor. If samples with different doping levels are used, it is possible to study the behaviour of a defect under electric fields that vary by several orders of magnitude, and a variety of phenomena described in Section 2.2.3 may be observed.

4

Planning of the digital DLTS set-up

The change in capacitance of the sample during a DLTS capacitance transient is typically in the order of 1% of the total capacitance. Since it is generally difficult to measure a signal superimposed on such a large background, a lot of noise may be expected in the transient. The problem is not helped by some of the analysis techniques (e.g. inverse Laplace transforms) that are very sensitive to noise and require a high signal to noise ratio of 1000:1 or better. Consequently, great care has to be taken to avoid the effects of both random noise and systematic errors on the system and particular attention needs to be paid to using good quality instruments, correct grounding techniques and adequate screening.

If, despite taking all reasonable precautions, the signal to noise ratio is still too low, random noise may be reduced by taking the average of a large number of transients. This approach is usually followed where very high signal to noise ratios are required, e.g. for Laplace DLTS. However, it is not feasible for very long transients. In this case, it usually suffices to apply a low pass filter to the measured data.

The averaging of a large number of transients will not reduce noise that is periodic with the applied DLTS pulse. This periodic noise may occur either because the transient is recorded at a frequency that is close to that of some source of interference (usually 50 Hz mains noise and harmonics) or that some component of the DLTS system generates periodic noise. The main source of such periodic noise was found to be the pulse generator used to bias the sample.

A further source of error in a DLTS system is temperature measurement and control. Since the emission rate of a defect as well as the capacitance of the diode varies with temperature, it is essential that the sample be kept at constant temperature during the DLTS measurement.

In this chapter, the requirements of some of the components in a DLTS system will be discussed. The system used in this study will be described and the results of some tests performed on the system are presented as well.

4.1 Acquisition of the capacitance signal

The main component distinguishing a digital DLTS system from an analogue LIA-based system is the presence of an analogue to digital converter (ADC) that digitises the analogue signal and sends it to a computer for further analysis. In such a system, a number of trade-offs have to be made. Probably the most important is the speed and the resolution of the ADC.

4.1.1 Random noise

The amplitudes of typical DLTS transients range from about 10^{-1} down to less than 10^{-4} times the average capacitance of the sample, which ranges from 10 to 300 pF. This implies that, in order to be able to observe a transient with amplitude $\Delta C/C$ of 10^{-4}, the system has to measure transients with amplitude as low as 1 fF superimposed on a background of 10 pF. Good results in an LIA type analysis require the noise in the system to be an order of magnitude less than the smallest expected transient, i.e. 0.1 fF. This requirement becomes much more stringent if Laplace analysis is to be performed where a signal to noise ratio of 1000:1 or better is required in order to separate peaks differing by a factor two in emission rate. In order to achieve such a low level of noise, it is important to select a good quality capacitance meter and to ensure that noise from the pulse generator supplying the DLTS bias does not produce extra noise at the output of the capacitance meter.

In most LIA-based DLTS systems, the noise is further reduced by firstly compensating for the background capacitance by means of an “offset capacitor”. This allows the capacitance meter to be used on a more sensitive range, providing a higher signal to noise ratio. Secondly, the output of the lock-in amplifier is filtered with a time constant much longer than the period of the LIA, thereby averaging the signal over a number of transients.

Similar techniques may also be used in a digital DLTS system, except that the analogue filtering of the LIA output is replaced by digitally averaging the output of the capacitance meter over a number of transients. According to the Central Limit Theorem, such averaging should reduce the random noise by a factor of $\sqrt{n}$, where n is the number of averages taken. This averaging technique is very effective for fast transients, but becomes time consuming for longer transients. Here some of the high frequency noise may be removed by applying a smoothing algorithm to the transients.

4.1.2 Response time, sampling rate and resolution

In contrast to a temperature-scanned DLTS system, an isothermal DLTS system keeps the temperature constant while the transient is analysed for decay curves of different time constants. Since the range of

peaks that such a system can detect at a specific temperature depends on the range of time constants that can be analysed, it is important to set up the system to measure the widest possible range of decay time constants. In general, there is no lower limit to the speed of an ADC, so only the upper limit will be discussed.

In most capacitance-based DLTS systems, the capacitance meter is the factor limiting the response time. An estimate of the response time can be made by considering a typical capacitance meter operating at a frequency of 1 MHz. These capacitance meters generally need at least ten oscillator cycles to measure the capacitance; therefore, it does not make sense to sample at a rate of more than 100 kHz.

Generally, there is a trade-off between the speed of an ADC and its resolution. It is common to find 8-bit ADCs that operate at frequencies in excess of 100 MHz, however, as soon as a higher resolution is required, the techniques used to speed up these fast ADCs (e.g. flash converters) become prohibitively expensive and can no longer be used.

As mentioned previously, many of the mathematical techniques that are used to analyse a DLTS signal are extremely sensitive to noise and inaccuracies in the DLTS signal, and require a signal to noise ratio of 1000:1. Furthermore, there are frequently noise spikes superimposed on the signal that can be up to ten times the magnitude of the DLTS signal. Therefore, it is rarely possible to use the full range of the ADC for the signal, as some leeway has to be left for the noise spikes. Ideally, the ADC is required to have a resolution of at least 0.01% of full scale (i.e. 4 digits or 14 bits).

4.1.3 Periodic noise

While the averaging technique described in Section 4.1.1 is quite effective in reducing random noise, the technique will not reduce noise that is periodic with the applied DLTS pulse. The main source of such noise was found to be the pulse generator used to apply the DLTS bias to the sample. For example, the HP8115 Pulse Generator produces a glitch of about 0.5 mV roughly halfway through the transient (see Figure 4.2 and associated discussion in Section 4.2.3). Since the period in an LIA-based DLTS system remains constant, such a glitch causes only a shift in the baseline of these systems, for which is easily corrected. However, when frequency-scanned measurements are made or the DLTS signal is analysed numerically, such a glitch halfway through the signal can lead to confusing and misleading artefacts.

4.1.4 Stability

In an isothermal DLTS system, the length of the transient may vary over several orders of magnitude from a couple of milliseconds to tens of kilo seconds. This poses the problem that the instrumentation should be able to respond to fast changes in the order of tens of microseconds while remaining stable and able to record changes taking place over several minutes or even hours.

If the same criterion as for random noise is used, the system has to be stable to a level of approx 1000:1, or 10^5:1 relative to the original capacitance for a typical transient. This implies that the temperature, bias voltage and the drift of the capacitance meter and the ADC should all be tightly controlled.

Equation (2.11) can be used to determine the dependence of the capacitance of a sample on the applied bias. After some manipulation, it follows that

$$\frac{dC}{C} = -\frac{1}{2}\frac{dV_{\mathrm{d}}}{V_{\mathrm{d}}} \approx -\frac{1}{2}\frac{dV_{\mathrm{r}}}{V_{\mathrm{r}}}. \tag{4.1}$$

From this it follows that in order to measure the capacitance accurately to $\Delta C/C \sim 10^{-5}$, the reverse bias has to remain constant to one part in 2×10^5, or 5 μV in the case of a 1 V reverse bias. A similar procedure can be used to determine the sensitivity of the capacitance to temperature changes, which affect the free carrier density:

$$\frac{dC}{C} = \frac{dN_D}{2N_D}. \tag{4.2}$$

If, as a very rough approximation, one assumes that a 10 K temperature change causes a 10% (linear) change in the carrier concentration, it follows that

$$\frac{dC}{C} \approx 0.05\ \frac{dT}{T}. \tag{4.3}$$

This implies that, for a transient at 100 K, the temperature has to be kept constant to 20 mK in order to limit $\Delta C/C$ to less than 10^{-5}. However, at low temperatures close to freeze-out, the capacitance of a sample can change very fast, and even higher temperature stability is required.

Another factor affected by temperature variations is the emission rate. From Equation (2.21), it follows that

$$\frac{de_{\mathrm{n}}}{e_{\mathrm{n}}} = -\frac{E_{\mathrm{C}} - E_{\mathrm{T}}}{kT}\frac{dT}{T}. \tag{4.4}$$

Clearly the quantity $(E_{\mathrm{C}} - E_{\mathrm{T}})/kT$ depends on the specific defect involved, however, in order for the trap to be observed by DLTS, the depth of the trap $E_{\mathrm{C}} - E_{\mathrm{T}}$ has to be significantly greater than kT. On the other hand, if $E_{\mathrm{C}} - E_{\mathrm{T}}$ is much greater than kT, emission from the trap will be too slow to be observed. For a typical defect, i.e. the EL2 ($E_{\mathrm{T}} - E_{\mathrm{C}} = 0.825$ eV) observed at 300 K, the quantity $(E_{\mathrm{C}} - E_{\mathrm{T}})/kT$ is approximately 30. If $(E_{\mathrm{C}} - E_{\mathrm{T}})/kT$ is increased by 3, the emission rate drops by an order of magnitude. A safe maximum value for this quantity is approximately 50 so that we have

$$\frac{de_{\mathrm{n}}}{e_{\mathrm{n}}} \sim -50\frac{dT}{T}. \tag{4.5}$$

I.e. for 10% accuracy in the emission rate, the temperature needs to be constant to 200 mK. Obviously, for techniques such as Laplace DLTS where very narrow peaks are to be resolved, better temperature stability is required.

4.2 Selection and characterisation of the instrumentation

4.2.1 Digitiser

A good compromise between the requirements mentioned above was found in the Agilent 3458A Multimeter. This multimeter uses a multi slope integrating A/D converter that is designed in such a way as to allow for different conversion speeds. For example, at the maximum conversion rate of 100 kHz, the A/D converter provides 16 bits resolution, but at lower conversion rates, the resolution increases up to 24 bits. A further advantage is that the integrating A/D converter takes the average of the input signal over the acquisition time, therefore it automatically smoothes the input signal. This has the advantage that if a signal is sampled at a lower rate (e.g. 10 Hz) the converter does not measure the instantaneous input voltage, but rather takes the average over a 100 ms period, thus smoothing the signal and reducing the noise level. The 3458A is therefore capable of sampling at the required rate with an acceptable resolution, while much higher resolution is available at lower sampling rates.

Furthermore, the short-term stability of the multimeter far exceeds the requirements mentioned in Section 4.1.

4.2.2 Capacitance meter

A Boonton 7200 capacitance meter was used throughout this study. This same model was used in the LIA-based DLTS system. The 7200 has a fast response and a recovery time of less than 50 μs after an overload condition. The capacitance meter also allows the user to set a number of other parameters such as the oscillator signal level and has an internal bias source.

Traditionally, a number of modifications were made to older model Boonton capacitance meters used for DLTS measurements such as the 72B and 72BD. These modifications, described by Wang (1985), Christoforou (1991), and Chappell (1984) speed up the response time of the capacitance meter and reduces the time the capacitance meter requires to recover from an overload. A number of studies were made to compare the response of a modified Boonton 72BD with those of a standard 7200. In all cases, the response time and noise levels of the 7200 were similar or better than that of the modified 72BD, used previously.

In some of the very long period studies where field effect measurements were made, spurious pulses generated by the pulse generator during programming caused unwanted filling of the traps in the sample. It was therefore necessary to protect the sample from the spurious pulses produced by the pulse generator by switching the sample to the internal bias supplied by the capacitance meter. An R-C network was also added to ensure that the sample remained biased while the relay was switching between the two bias sources. The circuit diagram of the modification is shown in Figure 4.1. Note that the R-C network would influence the transition time of the pulses applied to the sample, however since this experiment involved particularly slow transients, and the time constant RC is $\sim 150\ \mu s$, the effect of the RC circuit could be neglected.

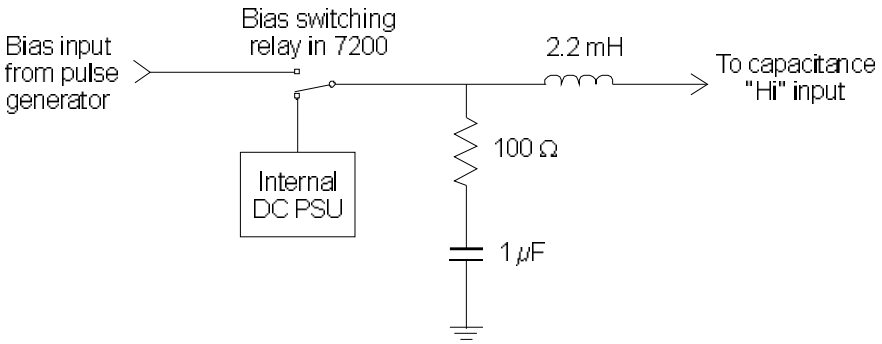

Figure 4.1 *Circuit diagram of the modifications made to the bias circuit of the Boonton 7200 Capacitance Meter.*

4.2.3 Pulse generator

In a DLTS system, the main purpose of the pulse generator is to supply a filling pulse to the sample, followed by a constant quiescent reverse bias during which the capacitance of the sample is observed. In many systems, the pulse generator also supplies the main timing signal and drives accessories such as fast pulse switches and lasers for optical DLTS. A number of pulse generators were available in the department. All were characterised in terms of their output noise and periodic glitches. Due to its programmability and superior performance the Agilent 33120A was selected for most of the work done in this thesis, however where faster pulses were required, an Agilent 8110A was used.

As mentioned earlier, only a small change in voltage is enough to change the capacitance of a Schottky diode by the same magnitude as a typical DLTS transient. Ideally, the voltage across the sample should stay constant to approx. 50 μV, or at least not vary by more than this value in a periodic way. This is especially true for an isothermal DLTS system, where a systematic glitch in the output of a pulse generator, even though its amplitude is much smaller than the random noise, can produce noticeable effects.

Since this requirement on the output of the pulse generator is much more stringent than that required in most applications, it is usually not specified in the specifications of the pulse generator, and it was necessary to measure the output of the pulse generators. During these measurements, the average of 100 pulses was taken in order to reduce random noise and make the periodic features visible. The results of these measurements are shown in Figure 4.2. Clearly, the old HP8115A pulse generator with a 0.5 mV step in the middle of its period would not be suitable. However, even some of the more expensive pulse generators, such as the Agilent 8110A also showed periodic features. The best results were obtained from arbitrary waveform generators, such as the Agilent 33120A and the 33220A, which were relatively free from periodic noise probably because, in contrast to the analogue oscillator, the digital electronics controlling the DAC cannot couple in low frequency periodic noise to the output.

It was finally decided to use the Agilent 33120A pulse generator, which had no noticeable periodic noise after the pulse, and was not too expensive. The UMIST Laplace card also produced a signal that

was free from periodic noise, though significantly more random noise. This, however, should not be a problem as the biasing circuit of the capacitance meter easily filters out the high frequency noise.

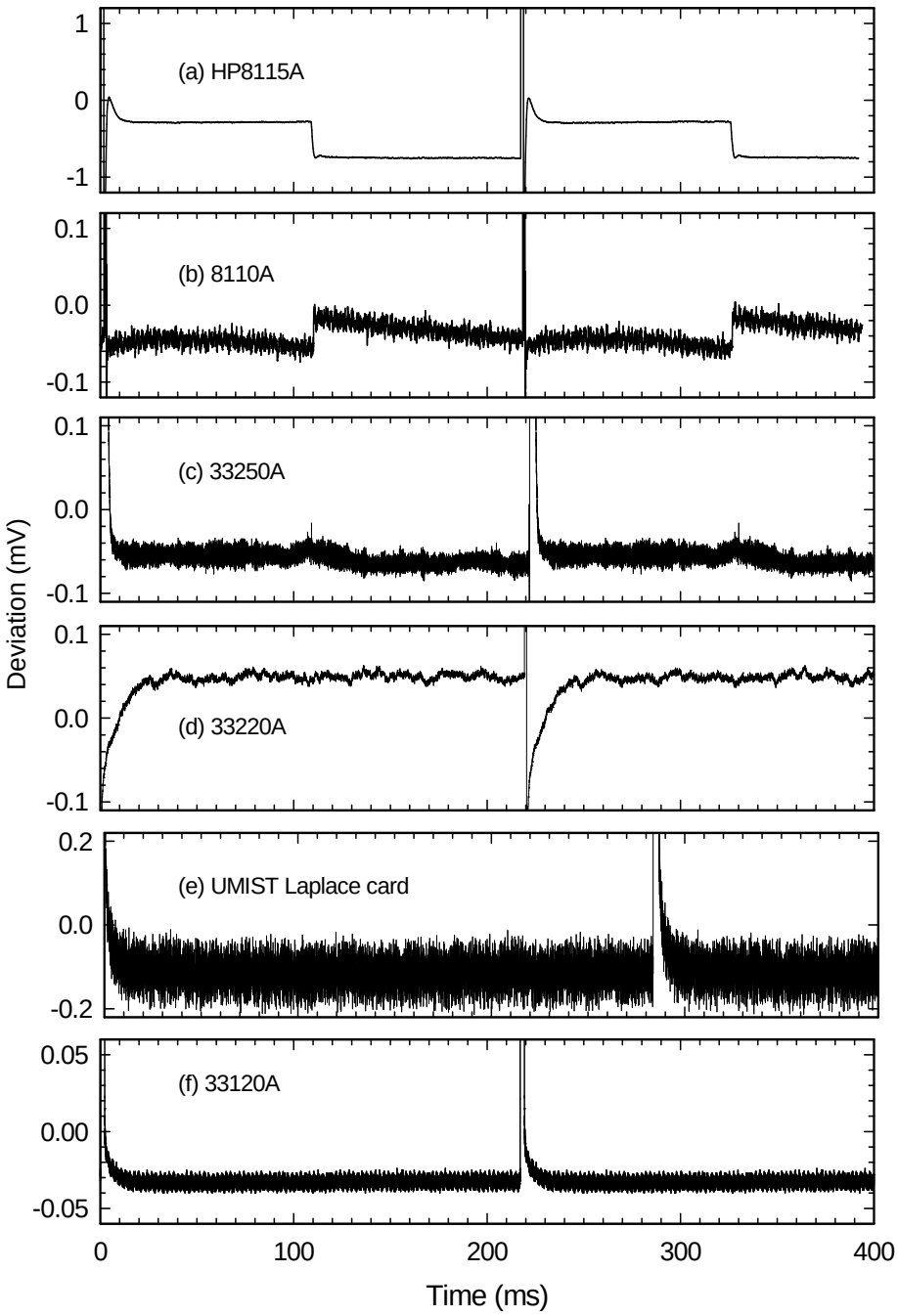

Figure 4.2 *The output obtained from six different pulse generators. In each case, a 1 V pulse was superimposed on a –1 V background. In order to emphasise the periodic noise, the average of 100 pulses was taken. The voltage was measured by means of an HP3458A multimeter on the 1 V scale. Note that the graphs have different vertical scales.*

4.2.4 Rise and fall times

The capacitance meter contains filters that prevent the 1 MHz test signal from travelling along the biasing cables and thus leading to erroneous measurements. However, these filters also act on the external bias applied via the capacitance meter to the diode under test. The positive side effect is that any high frequency noise in the output of the pulse generator is filtered out. However, the high frequency components are also removed from the filling pulse, causing overshoot of the filling pulse seen by the diode under test. While this overshoot is relatively harmless at the trailing edge, at the leading edge of the pulse the overshoot could fill traps shallower than intended. The overshoot can be avoided by smoothing the leading edge of the pulse (Figure 4.3). At the trailing edge, such smoothing is not necessary, and smoothing may in some cases even be detrimental. Therefore, the pulse generator should be able to produce pulses with a slow leading edge and a fast trailing edge. Another reason for the fast trailing edge is that in the current system, the trailing edge was used for synchronisation (see section 4.3.2).

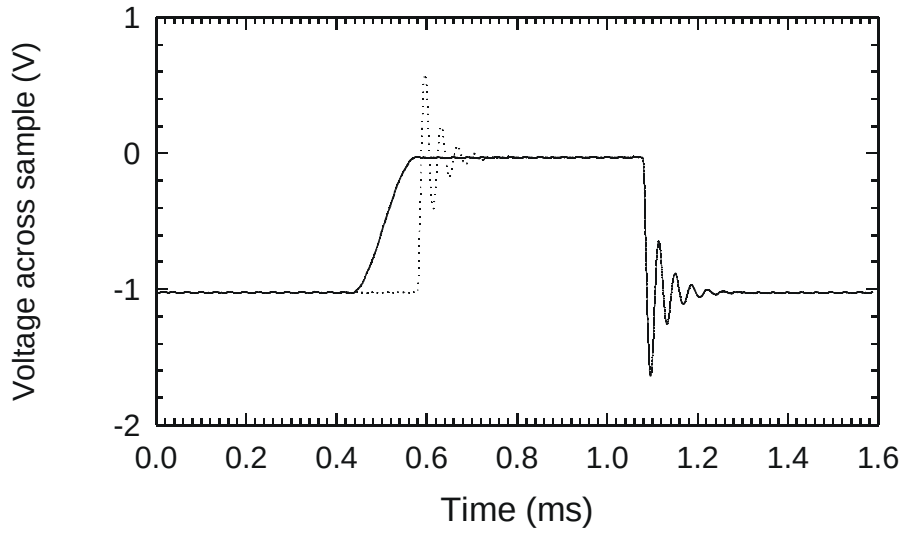

Figure 4.3 *The output of the Boonton 7200 capacitance meter in response to an external bias pulse. The solid line shows the output due to a pulse having a leading edge rise time of 0.5 ms, which eliminated the overshoot indicated by the dotted line, observed when a fast rise time (25 ns) was used. The output was measured using a Nicolet 4570 oscilloscope and the pulse generated using an HP33120A function generator.*

4.2.5 Sample mounting and temperature control

For DLTS measurements, the sample was mounted in an Air Products APD HC-2 cryostat, on a sample holder incorporating a sapphire disc that isolated the sample electrically, but ensured excellent thermal contact with the tip of the cold finger. Myburg (1992) describe the construction and performance of this sample holder (illustrated in Figure 4.4). Contact to the back ohmic contact was established by putting

the sample on a piece of indium foil. Both the Schottky contact and the indium foil were connected to the measurement circuit by beryllium copper probes. To minimise damage to the Schottky contact, the tips of the probes were rounded by sanding with very fine sanding paper. In addition, care was taken not to scratch the contact when lowering the probe. To ensure that the ohmic contact made good electrical and thermal contact with the indium foil, an additional probe was used, when necessary, to apply pressure to the sample next to the Schottky contact.

A Lake Shore 340 temperature controller with DT-470 Si diode sensors (calibrated 10 – 500 K) was used for temperature control. Using this system, it was possible to keep the temperature of the sample constant to ± 10 mK . In all cases, isothermal measurements were performed only after the temperature stabilised.

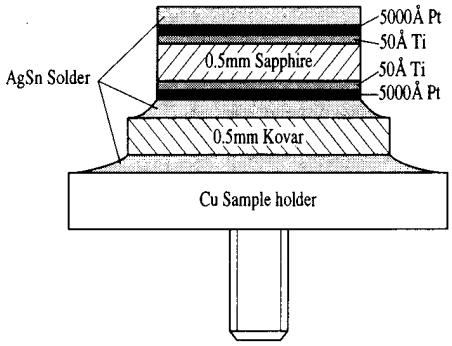

Figure 4.4 *A schematic drawing of the sample holder used during DLTS measurements. (Myburg, 1992)*

4.3 Other hardware

Except for the ready-made instruments, a number of other circuits were required to allow the system to work. For instance, a circuit was required to synchronise the recording of the transient to the DLTS filling pulse and accommodation had to be made for fast pulses, which, due to the filters in the capacitance meter, could not be applied via the capacitance meter.

4.3.1 Fast pulse interface

A number of measurements required the application of short pulses ($< 10\ \mu$s). These pulses would be severely distorted or even completely filtered out by the filters in the capacitance meter. The solution to this problem is to use reed relays to connect the pulse generator directly to the sample, while at the same time disconnecting the capacitance meter. Since it is critical that the sample is never left unconnected, the timing of the reed relays was set so that the capacitance meter was only disconnected once the pulse generator was connected and there was no more contact bounce from the relay.

Similarly, after the pulse was applied, the pulse generator was only disconnected after the capacitance meter was reconnected.

Great care was taken to select reed relays with short switching times (< 0.1 ms) and minimal contact bounce. A block diagram of the fast pulse interface is shown in Figure 4.5. This circuit allowed pulses as short as 50 ns to pass without significant distortion.

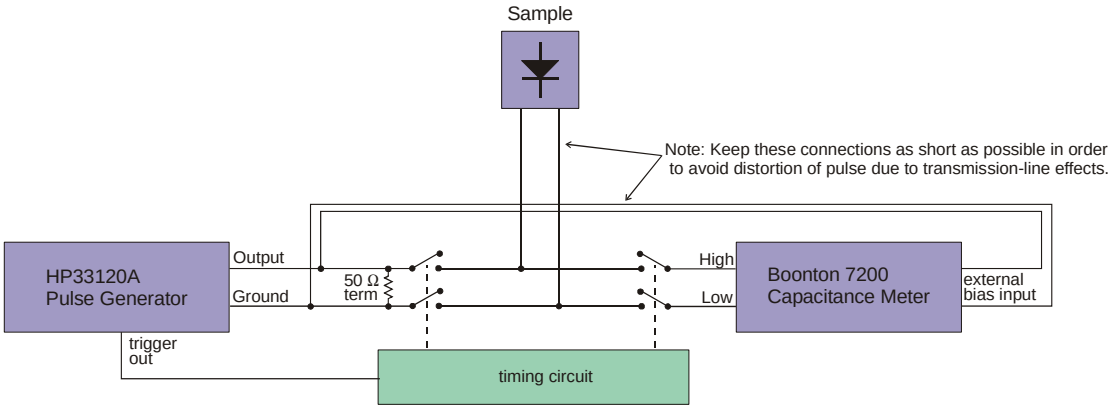

Figure 4.5 *A block diagram of the fast pulse interface.*

4.3.2 Synchronisation

It is necessary that the multimeter be in some way triggered at the start of the transient to enable it to start measuring. This trigger has to be accurate to ensure that the same reference point is used for different measurements. Furthermore, when filling pulses of varying lengths are used, the multimeter should always be triggered at a time relative to the trailing edge of the filling pulse. Therefore, it was decided to trigger the multimeter with the trailing edge of the filling pulse. Since the height and offset of the filling pulse can vary, it is not possible to use a level-sensitive trigger. However, since the HP33210A allows for different transition times for the leading and trailing edges of the pulse, the trailing transition of the pulse can be made very fast without affecting the slow rise time required for the leading edge. Consequently, it was decided to trigger on the derivative of the filling pulse. Figure 4.6 shows the circuit that was used. It consists of a voltage follower that acts as a buffer, connected to a differentiator. The output of the differentiator is fed into a voltage comparator (with some hysterisis to avoid oscillations) followed by a monostable timer that eliminated spurious triggering due to oscillations after the initial trigger pulse. The output of this circuit was used to trigger the multimeter as well as an oscilloscope that was used to troubleshoot the set up.

A block diagram of the complete digital DLTS system is shown in Figure 4.7.

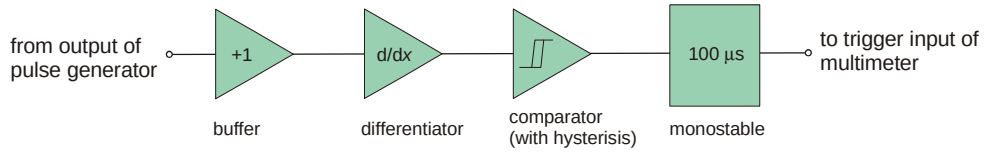

Figure 4.6 *A block diagram of the trigger circuit that was used for synchronisation.*

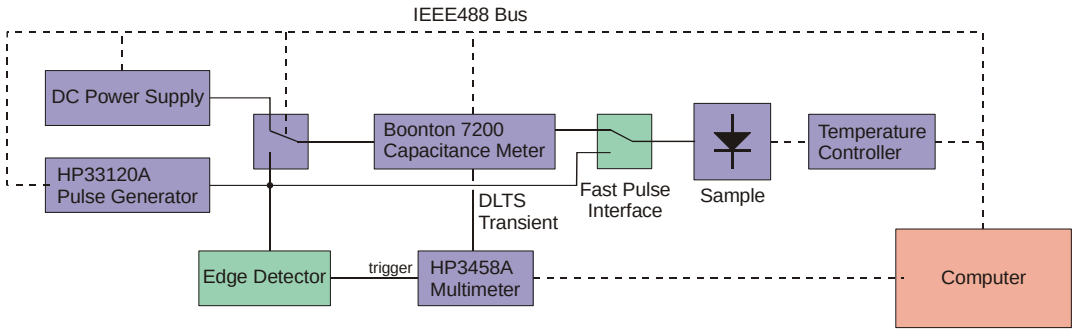

Figure 4.7 *A block diagram of the DLTS system showing the main components.*

4.4 Software

It was decided to transfer data from the multimeter to the computer in real time via the GPIB interface, thereby avoiding the need to use the limited buffer in the 3458A for temporary storage. Furthermore, since the data was transferred during the measurements, no extra time was required for this procedure. The highest transfer rate needed for measurements was 200 kB/s.

In order to achieve this high transfer rate, the software was written in Borland C and run under DOS, where the transfer of data would not be interrupted by other processes. A National Instruments PCI GPIB interface card was used. With current technology, a solution under Windows, using an environment such as LabView is probably possible, and might be preferable to the solution used in this study.

The acquisition software controlled and programmed all instruments that were involved in the measurement. Specifically, the software downloaded the required DLTS pulse to the arbitrary waveform generator, and settings such as sampling rate, resolution and aperture time were set on the multimeter. The acquired signal was averaged during the measurement, and saved to disk. The program allowed up to 64k points per transient to be measured up to the maximum sampling rate of the

multimeter, and up to 64k transients to be averaged. Measurements were automated by writing C functions that called subroutines in the main program. These C functions served as confirmation of measurement conditions, while further comments in these C functions were used for explanatory notes and further documentation.

The raw data obtained from the measurement program was smoothed using a linear weighted least squares smoothing algorithm (Jacoby, 2000), in which the data points for the smoothed curve was determined by performing a weighted least squares fit on a window of points surrounding the point in question. The weights of the points were selected to decrease rapidly as points further from the point in question. The advantage of this smoothing technique is that it allows for interpolation so that points in the smoothed data set could be spaced differently to those in the unsmoothed data set. In order to reduce the amount of data involved, the time intervals were spaced logarithmically.

In order to show DLTS spectra over a wide range, a number of transients of differing lengths were recorded. More averages were taken for shorter transients, thereby reducing the noise, while less averages were taken for longer transients, where smoothing could easily reduce noise. The recorded transients were combined to form one long transient during the smoothing procedure. This procedure reduced measuring time, while still producing acceptable DLTS spectra. Care was taken that the filling pulse was of sufficient length to fill all defects, in order to ensure that both the short and the long transients started under identical conditions, so that there was no effect carried over from the previous filling pulse.

Some experiments were made to interlace the recording of the transients. According to this procedure, the longer transient was always preceded by a number of repetitions of the shorter transient, thereby making measurement conditions more similar. However, since this interlacing procedure required more intricate programming, and the more simple procedure of recording the transients of differing lengths separately provided good results, the interlacing was not used.

DLTS spectra were obtained from the smoothed capacitance data by simulating the action of a lock-in amplifier being swept over a frequency range. The DLTS signal was calculated by

$$S(\tau) = \frac{1}{\tau}\int_0^{\tau} C(t)\sin\left(\frac{2\pi t}{\tau}\right)dt\ . \tag{3.6}$$

Further manipulation of the signal, such as subtraction and peak detection was performed using the program SigmaPlot.

5 Experimental

5.1 Introduction

The experimental section is organised in four chapters of which this one is the first. Each describes some background theory relevant to the topic. It was decided to rather discuss the aspects of the theory, which are not directly related to DLTS, as part of the experimental section where it is closest to its application.

5.2 Sample preparation

5.2.1 Gallium Arsenide

The same procedures for sample preparation were followed in all experiments. The sample was chemically cleaned before evaporation of the ohmic, as well as the Schottky contacts. The procedures used in both cases were similar, except that cleaning before the evaporation of Schottky diodes, included etching. Myburg (1992) describe the chemical cleaning procedure in detail: It involved degreasing in boiling trichloroethene, followed by rinsing once in isopropanol and then twice in de-ionised water ($\rho > 10^{18}\ \Omega\text{cm}$). Etching was performed, for 30 s, in a solution of 3 parts NH_3 (15 mol dm^{-3}) and 1 part H_2O_2 (30%) in 150 parts de-ionised water at 25°C. Etching was followed by another rinse in de-ionised water, followed by oxide removal in 6 mol dm^{-3} HCl (2 min) and a final rinse in de-

ionised water. The samples were dried under a stream of high purity nitrogen, and immediately transferred to the evaporator.

Ohmic contacts were formed by the deposition of Ni (50 Å), AuGe (2000 Å) and Au (2 500 Å) on the n^+ back surfaces of the sample, before the fabrication of the Schottky contacts. The contacts were annealed at 450 °C for 2 min in a quartz tube under a flow of Ar.

Before evaporation of the Schottky contacts, the samples were dipped in 6 mol dm^{-3} HCl for 2 – 3 seconds. Depending on the metal being deposited, either resistive or electron-beam evaporation was used to deposit the contacts through a mechanical mask.

5.2.2 Silicon

Before the deposition of Schottky contacts, the samples were degreased in boiling trichloroethylene followed by rinsing in boiling isopropanol and in de-ionised water. The samples were etched in a 10% HF solution. On the p-type material, Ti Schottky contacts were used.

For ohmic contacts, In/Ga eutectic mixture was used on the unpolished back surfaces.

5.2.3 Gallium Nitride

A similar cleaning procedure was used before deposition of both ohmic and Schottky contacts. The GaN samples were cleaned by boiling them in aqua regia (see Hacke, 1993). After rinsing the samples in de-ionised water, the samples were degreased in boiling trichloroethylene followed by rinsing in boiling isopropanol and in de-ionised water. Hereafter, the samples were dipped in a 50% HCl solution for 10 s, before being transferred to the vacuum system.

Ohmic contacts, consisting of 150 Å/2 200 Å/400 Å/500 Å layers of Ti/Al/Ni/Au (Ruvimov, 1993) were deposited by means of electron beam evaporation and annealed at 500°C for 5 min in Ar. Schottky contacts were deposited by means of either sputter deposition or resistive evaporation through a metal contact mask.

5.3 IV and CV characterisation

A number of artefacts observed during DLTS measurements can be traced to high resistivity and high leakage current (Chen, 1984). In order to evaluate the risk of these effects influencing the DLTS measurements, the quality of the contacts was evaluated by means of IV and CV measurements before DLTS measurements were performed. Since it was found that the quality of the contacts deteriorated after prolonged measurements in the cryostat, the IV and CV measurements were occasionally repeated.

The IV measurements were made by an HP 4148A pA meter/voltage source, capable of measuring currents as low as 10^{-14} A. The sample was screened from light and electrical noise by enclosing it in a light-tight metal box during measurements. The most important characteristics obtained from the IV graph were: the series resistance R_s, the barrier height $\phi_{b(IV)}$, the ideality factor *n*, and the leakage current at 1 V reverse bias $I(-1)$.

The CV characteristics were measured by an HP 4192A Impedance Analyzer, controlled by a computer via an IEEE interface. The CV measurements were performed with the sample mounted inside the cryostat at the temperature where the isothermal DLTS measurements were to be performed. Measuring conditions (i.e. oscillator level and frequency) were chosen to correspond as closely as possible to those of the DLTS measurements.

The CV characteristics were used to measure the average free carrier concentration of the sample, N_D, as well as to check the uniformity of the doping profile. The dissipation factor D (equal to the tangent of the phase angle) was measured at the reverse bias where DLTS measurements were to be performed. This factor was used to determine the degree by which the behaviour of the sample deviates from that of an ideal capacitor.

6

Characterisation of the EL2 and E2 defects in n-GaAs

6.1 Introduction

One of the advantages of a digital DLTS system over an analogue system is that the digital DLTS system allows the observation of capacitance transients with time constants varying over several orders of magnitude. In order to test the DLTS system, it was decided to measure the emission of a defect over the widest possible temperature range. Both the EL2, in as-grown material, and the radiation-induced E2 defect in GaAs were measured over a wide temperature range. The results were compared to measurements obtained from an LIA-based DLTS system.

For the EL2 defect, the results obtained using digital DLTS corresponded well with those obtained previously using an analogue system. The experimental results were also close to previously published results. This was also true for the E2 at higher temperatures. However, below approximately 40 K, the emission rate of the E2 no longer decreased with decreasing temperature, but remained constant at roughly 1×10^{-3} s^{-1}. Further experiments indicated that the emission rate of this temperature-independent peak was not affected by the electric field effect.

These unexpected observations had not previously been reported in the literature, and a number of experiments were performed to ensure that the unusual results were not due to an artefact in the measuring system. After some experimentation, it was found that the observed emission was caused by blackbody radiation from the outer shroud of the cryostat that reached the sample through a hole in the radiation shield.

6.2 The EL2 and E2 defect levels in n-GaAs

The EL2 defect is probably the most extensively studied defect in GaAs. It is always present in as-grown GaAs in concentrations typically varying from 10^{15} to 10^{17} cm^{-3}. Despite the large amount of research done on the EL2, the atomistic origin of the defect level is not yet fully understood. However, it seems that it involves an arsenic anti-site defect (As_{Ga}) (Martin, 1986; Pons, 1985). The DLTS signature of the EL2 level in GaAs is reported in the literature as E_t = 0.825 eV and $\sigma_{na} = 1.2 \times 10^{-13}$ cm^2. (See Kaminska, 1999 for a detailed review.)

The E2 is one of a number of electron traps in GaAs induced by particle irradiation, and has been well characterised. It is a reasonably shallow energy level with E_t = 0.140 eV below the conduction band, with an apparent capture cross-section of $\sigma_{na} = 1 \times 10^{-13}$ cm^2. Structurally, the E2, as well as the shallower E1, are thought to be caused by two charge states of close arsenic vacancy–interstitial pairs (Pons, 1985). Both the E1 and E2 defect levels show field-enhanced emission that can be described by the phonon-assisted tunnelling model (Goodman, 1994).

A quick calculation shows that, under low electric field conditions, the E2 level's emission rate should vary from 10^3 s^{-1} to 10^{-4} s^{-1} in the temperature range 40 to 90 K. Since this temperature range is easily accessible by the cryostats in the Physics Department, the E2 seemed to be the ideal defect to use to test the capabilities of the DLTS system. The EL2 was chosen because it is a well-known defect, however, the maximum temperature restriction of the cryostat limited the emission rate range that could be measured.

6.3 Experimental

In this study, 1×10^{16} cm^{-3} Si-doped n-GaAs grown by OMVPE on an n^+ substrate was used. Ohmic contacts were fabricated on the back surface of the sample and 0.2 μm Au Schottky contacts were deposited by resistive evaporation, as described in Section 5.2. The sample was irradiated, through the Schottky contacts, by 5.4 MeV α-particles from an Am-241 source at a fluence of 1×10^{11} cm^{-2} for 8 hours. According to a TRIM simulation, these α-particles penetrate through the gold layer to a depth of 26 μm into the GaAs. Under a reverse bias of 1 V, a typical Au Schottky diode on 10^{16} cm^{-3}-doped GaAs has a depletion region width of about 0.5 μm. The electrically active defects produced by the α-particles during their travel though the GaAs should therefore be easily detectable by DLTS under various biasing conditions. A schematic representation of the sample is shown in Figure 6.1.

DLTS spectra of the samples were measured in an LIA DLTS system as well as in the digital DLTS system. In the case of the analogue system, LIA frequencies ranging from 1 Hz to 1 kHz were used, while, for the digital system, measurements were performed at temperatures ranging from 270 to 380 K for the EL2 and 20 to 90 K for the E2 defect. (Due to materials used in the construction of the interface, the EL2 could not be measured at temperatures over 380 K). In both cases, the scans were recorded at a reverse bias of 1 V and a filling pulse height of 1.2 V.

The field dependence of the emission from the E2 defect was studied using the digital system by applying a reverse bias of 4 V and increasing the filling pulse from 0.2 V to 3.4 V in 0.2 V steps.

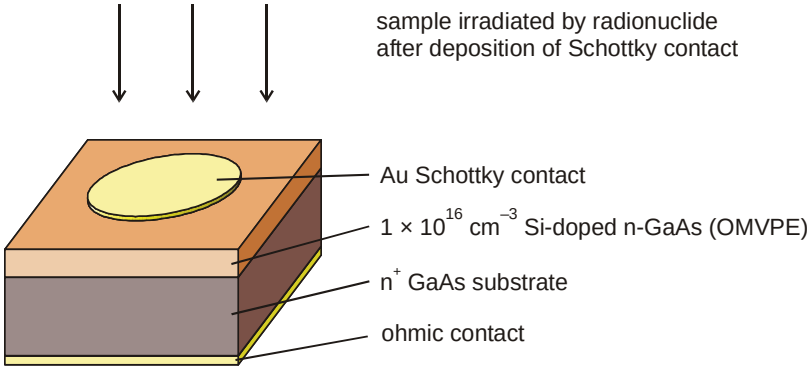

Figure 6.1 *Schematic representation of the sample used in this study.*

6.4 Results and discussion

Figure 6.2 compares the Arrhenius plots for the EL2 defect level as obtained by the two different systems. As seen in the graph, the digital system was capable of measuring the defect over a much wider range of emission rates. Over this wide range, no deviations from the linear relationship were observed. It can therefore be concluded that the digital system could measure long time constants accurately.

In the region where both systems could be used, the correspondence between the results was good. The DLTS signature obtained by the digital system (E_t = 0.833 eV and σ_{na} = 2.4 × 10^{-13} cm^2) corresponded reasonably well with the DLTS signature obtained by the analogue system (E_t = 0.785 eV and σ_{na} = 4.5 × 10^{-14} cm^2). Furthermore, the signature measured by the digital system was closer to the literature average mentioned in Section 6.2 (E_t = 0.825 eV and σ_{na} = 1.2 × 10^{-13} cm^2), than that obtained by the analogue system.

The difference in the results between the analogue and digital system seem to be due to a systematic deviation rather than due to random errors. The most probable cause for this systematic deviation is that the analogue system used an (uncalibrated) thermocouple to measure the temperature, while the temperature in the digital system was measured by a calibrated PT-100 sensor.

The results obtained by the digital DLTS system for the E2 level are shown in Figure 6.3. The emission rate from the E2 decreased as the temperature was decreased from 90 K to 40 K. However, when the temperature was decreased below 40 K, the emission rate from the E2 remained constant. In order to distinguish the peak showing a constant emission rate from the “normal” E2, the constant emission rate peak will be called E2'.

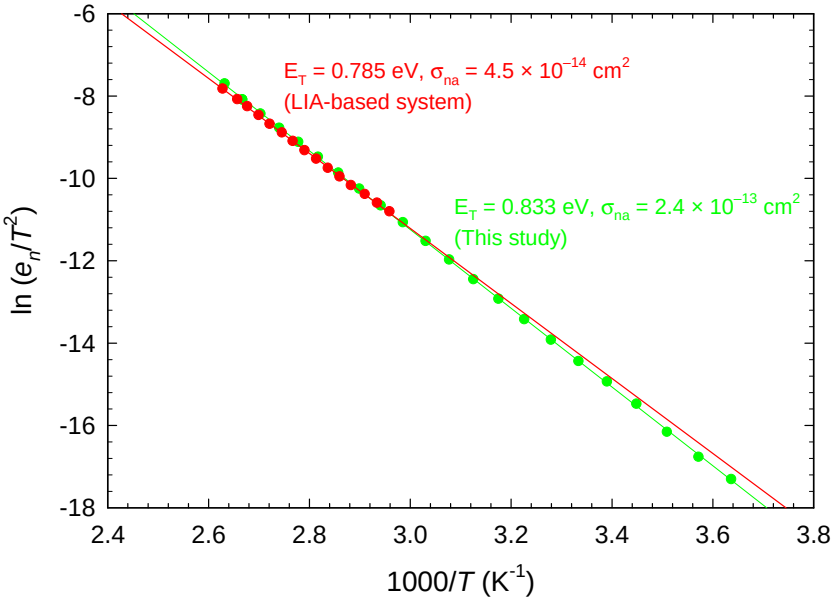

Figure 6.2 *Comparison of the Arrhenius plots obtained for the EL2 defect level as measured by the analogue as well as the digital DLTS system.*

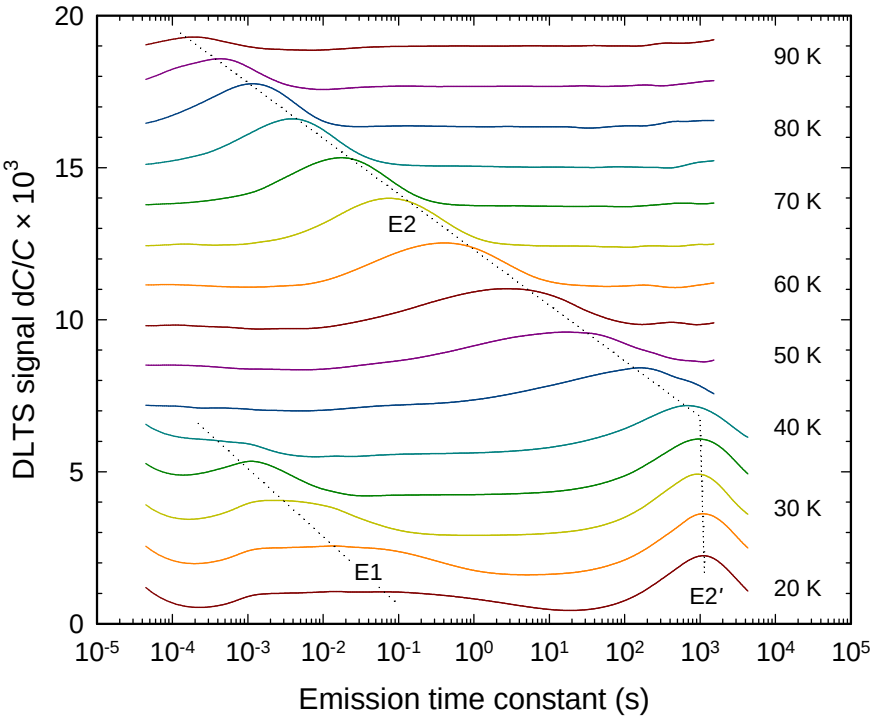

Figure 6.3 *Isothermal DLTS scans obtained from the sample at different temperatures. The bias conditions were: V_r = –1 and V_p = 1.2V. The broadening in the peaks is due to the electric field dependence of the emission rate, which becomes more pronounced at low temperatures.*

In the temperature range below 40 K, a peak due to the E1 was also visible. No unusual behaviour of the E1 was observed. The broadening in the peaks of both the E1 and the E2 was due to electric field enhanced emission. Note that the E2' peak did not show any signs of broadening.

It might be argued that, since the electric field remains approximately the same for all temperatures, the amount of broadening should also remain constant. However, in the lower temperature region, direct emission over the barrier becomes less important and the phonon-assisted tunnelling mechanism makes a significant contribution to carrier emission. Since phonon-assisted tunnelling is very sensitive to the electric field, it follows that, at lower temperatures, the varying electric field in the region probed by DLTS causes significant broadening of the DLTS peaks.

Figure 6.4 shows the dependence of the emission rate from the E2 on the temperature. At above 50 K, the log of the emission rate is approximately linearly dependent on 1/T, though at lower temperatures, the emission rate becomes practically independent of the temperature.

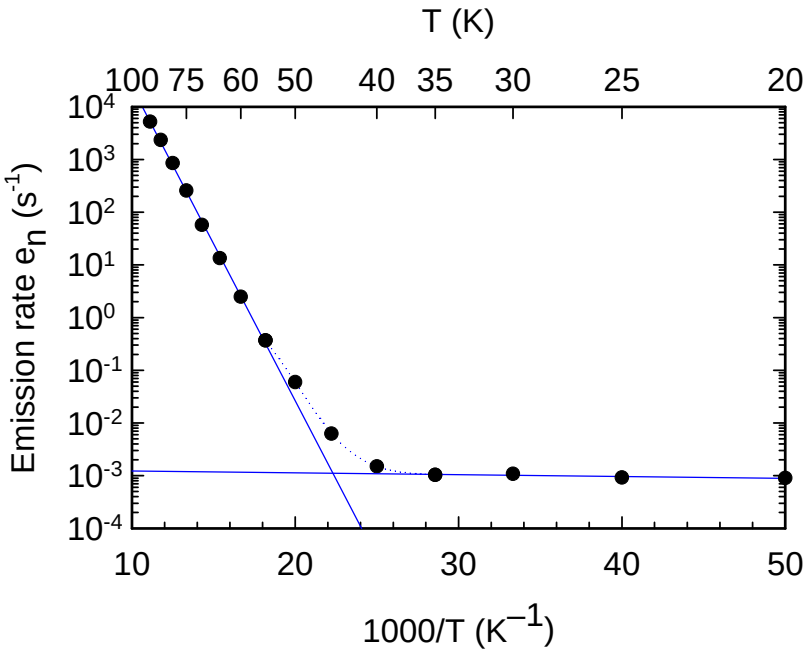

Figure 6.4 *Temperature dependence of the emission rate of the E2 level. (*V_r *= –1 V and* V_p *= 1.2 V, in* 1×10^{16} cm^{-3} *doped n-GaAs.)*

An Arrhenius plot of the data is shown in Figure 6.5. Here the data is compared to data obtained by an LIA based system in a previous study (Goodman, 1994). In the region above 50 K, the results agreed quite well, however, at 50 K a slight deviation is visible. Below 40 K the data was no longer described by Arrhenius' law, and therefore the temperature dependence of the emission rate from the defect could no longer be described by thermal emission according to Shockley-Read-Hall statistics.

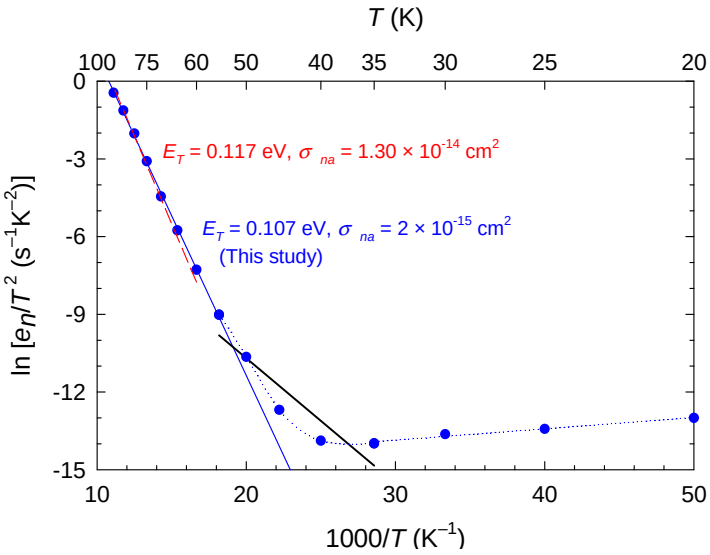

Figure 6.5 *Arrhenius plot of E2, obtained from the scans shown in Figure 6.3. The dashed line indicates results from Goodman (1994).*

Figure 6.6 shows digital DLTS spectra recorded at a reverse bias of 4 V and filling pulse amplitudes ranging from 0.2 V to 3.4 V incremented in 0.2 V steps. As the filling pulse amplitude was increased, defects closer to the surface were filled. These defects experienced a stronger field and therefore had a higher emission rate. Therefore, the DLTS peaks broadened to the left as the filling pulse was increased. Note that, in contrast to the E1, the E2' peak did not show any distortion due to the electric field until the filling pulse amplitude exceeded 2 V.

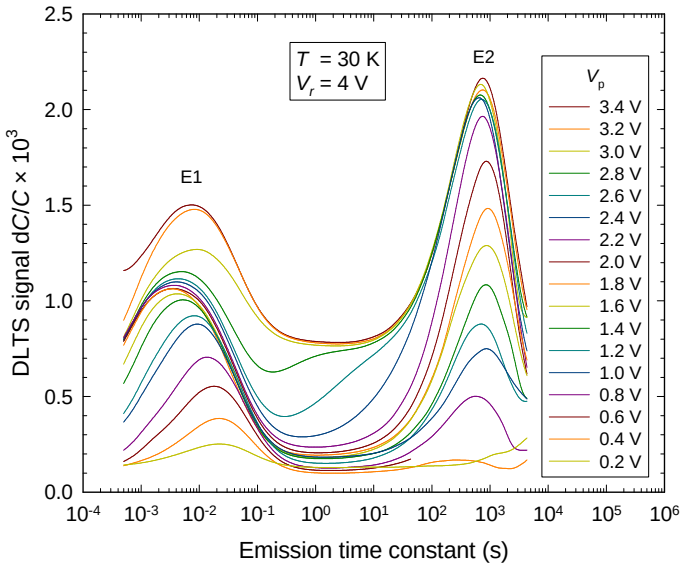

Figure 6.6 *Isothermal DLTS spectra of the E1 and E2 recorded at 30 K under a reverse bias of 4 V and filling pulse amplitudes ranging from 0.2 V to 3.4 V.*

In order to investigate the emission under a varying electric field, successive spectra in Figure 6.6 were subtracted. The result of this subtraction is shown in Figure 6.7, where the field dependence of the emission rate can be seen more clearly. Here it can be seen that the emission from the E2' remained independent of the electric field up to a field of 46 kV/cm after which the emission rate became strongly field dependent.

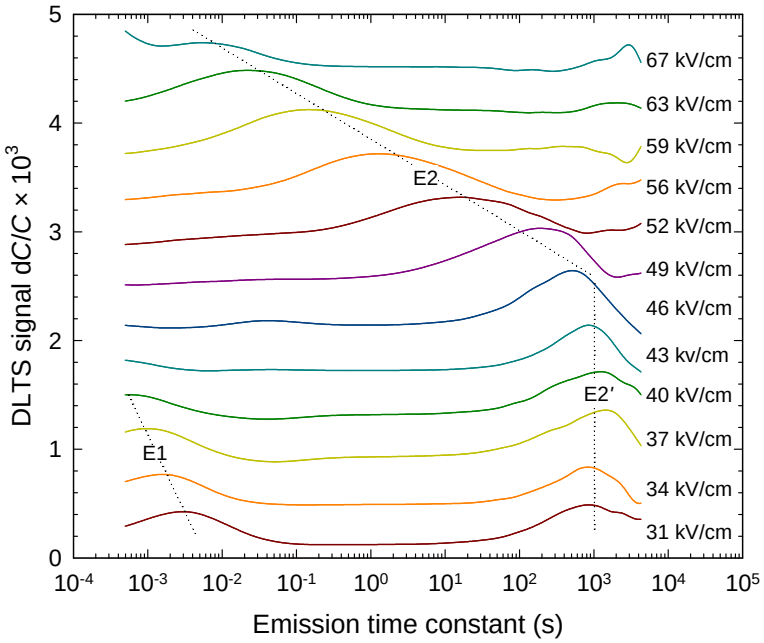

Figure 6.7 *Spectra obtained by subtracting successive scans in Figure 6.6. The average electric field experienced by the defects is also shown.*

The previous results strongly suggest that there was another mechanism according to which the E2 could emit carriers. This mechanism should be independent of temperature and electric field.

The radiation shield used in this study had a 10 mm hole in the top, for use in optical studies. When another radiation shield, without such a hole, was used, the E2' peak disappeared and was replaced with an E2 peak behaving as expected. The outer shroud of the cryostat was solid metal, so no ambient light could reach the sample. It is therefore thought that the observed emission of the E2 at low temperatures is due to blackbody radiation from the cryostat shroud.

A further investigation was done in which the top of the shroud was removed and replaced with an aluminium cap that was thermally insulated from the rest of the shroud. The bottom surface of the cap was sprayed with a carbon spray in order to approximate a blackbody radiator and a temperature sensor was attached to the cap. A 20-watt resistor was bolted on top of the cap to serve as a heater. In this way, using a second temperature controller, the temperature of the cap could be varied without affecting the rest of the set-up. It was found that the position of the peak due to the E2 shifted depending on the temperature of the cap, as shown in Figure 6.8. Note that only the position of the E2 peak shifts, therefore it is unlikely that the observed effect is due to a change in the temperature of the sample.

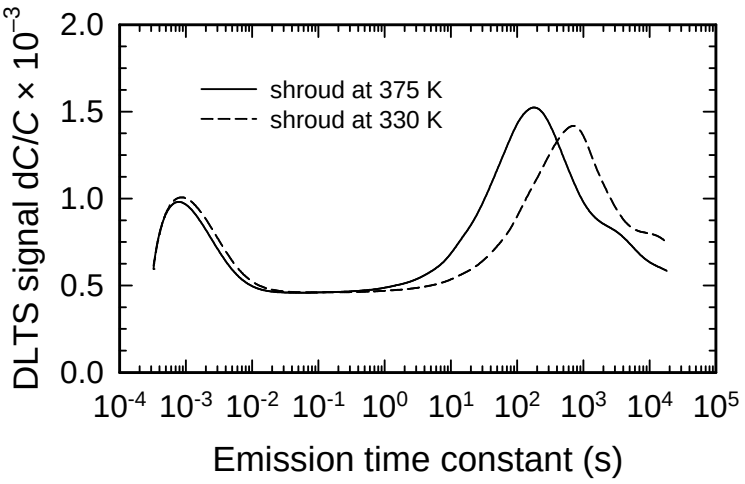

Figure 6.8 *Isothermal DLTS spectrum of the E1 and E2 levels recorded with the sample at 33 K and the cap of the radiation shield at different temperatures, showing the shift in the position of the peak due to the E2.*

6.5 Conclusions

The results obtained indicate that the digital DLTS system described can successfully measure defects with emission time constants ranging from 10^{-4} to more than 10^{3} s. The results obtained agreed well with results obtained previously using an LIA-based DLTS system, as well as with values published in the literature.

For very long time constants, deviations from the Arrhenius plot were observed, however, further investigations indicate that these deviations are due to blackbody radiation from the cryostat shroud.

6.6 Publications

Some of the results of this study were presented at the Conference on Photo-responsive Materials, Kariega Game Reserve, South Africa 25 – 29 February 2004 and published in Phys. Stat. Sol. (c) (Meyer, 2004):

1. Meyer WE and Auret FD 2004 Effect of thermal radiation on electron emission from the E2 defect in *n*-GaAs *Phys. Stat. Sol.* (c) **1** 2333

phys. stat. sol. (c) 1, No. 9, 2333–2336 (2004) / DOI 10.1002/pssc.200404850

Effect of thermal radiation on electron emission from the E2 defect in n-GaAs

W. E. Meyer* and **F. D. Auret**

Department of Physics, University of Pretoria, Pretoria, 0002, South Africa

Received 10 May 2004, revised 25 May 2004, accepted 2 June 2004
Published online 26 July 2004

PACS 71.55.Eq, 73.20.Hb

In this paper we describe the behaviour of the E2 defect in GaAs as measured by a digital DLTS system at temperatures much lower than those at which the defect is normally observed in analogue DLTS systems. We found that, at temperatures below approximately 40 K, the emission rate of the E2 defect became essentially temperature independent. We show that this behaviour is due to a competing mechanism, involving thermal radiation from the outer shroud of the cryostat, emptying the E2.

1 Introduction

The E2 defect level is one of the prominent electrically active radiation-induced defect levels in n-GaAs [1]. It can be observed by means of deep level transient spectroscopy (DLTS) [2] after irradiating n-GaAs with electrons, protons, α-particles and implantation with heavy nuclei [1, 3]. Under low-field conditions, the E2 has an energy level E_T and capture cross-section σ_{na} (collectively known as the defect's DLTS signature) of $E_C - 0.14$ eV and 1×10^{-13} cm^2 respectively in lowly doped material [1]. Emission from the E2 level is significantly enhanced by the electric field in the space charge region. This field-dependent emission is well described by the phonon assisted tunnelling model [4] with a Huang-Rhys factor, S, of 4.5 [5].

In this paper we present the results obtained when we investigated the emission from the E2 defect level at low temperatures (< 50 K) using a digital DLTS system, which is capable of measuring emission rates much lower than can be detected by traditional analogue systems.

2 Experimental

For this study we used <100> oriented GaAs epilayers grown by organo-metallic vapour phase epitaxy (OMVPE). The layers were grown on an n^+ substrate and had a free carrier concentration of 1×10^{16} cm^{-3} as determined by capacitance-voltage measurements. Ohmic contacts were fabricated on the back surface of the substrates and gold Schottky contacts, 0.7 mm in diameter and 0.2 μm thick, were evaporated resistively on the epilayer. The samples were irradiated through the evaporated contacts by 5.4 MeV α-particles from an Am-241 radionuclide.

Emission from the E2 was observed by means of a digital isothermal DLTS system in which the capacitance was measured using a Boonton 7200 capacitance meter. The capacitance signal was digitised by means of an HP3458A Multimeter. An HP33120A Arbitrary Waveform Generator provided the required reverse bias and filling pulses. The output of the HP33120A was found to be particularly stable with time, and did not suffer from baseline skew observed in some pulse generators. The use of an arbi-

* Corresponding author: e-mail: wmeyer@postino.up.ac.za

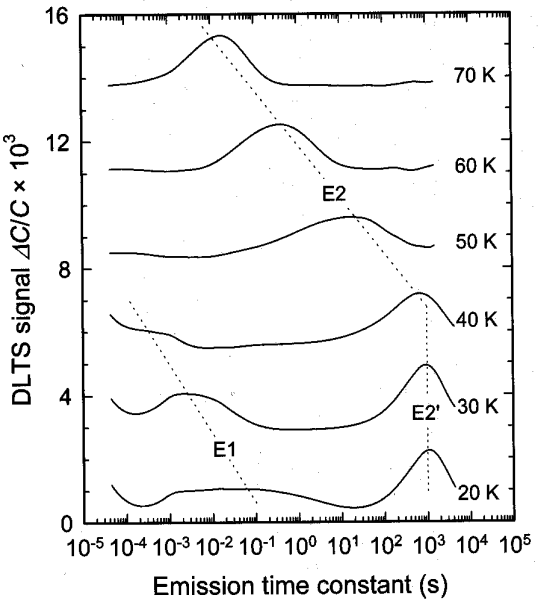

Fig. 1 Isothermal DLTS scans obtained at different temperatures. The bias conditions were: $V_r = -1$ and $V_p = 1.2$V.

trary waveform generator also allowed for the shaping of the filling pulse to minimise overshoot caused by the filters in the capacitance meter.

Initial measurements were performed without the inner shroud of the cryostat fitted. Hereafter, an inner shroud with its top removed was used. The top of the inner shroud was replaced with an aluminium disk that had a temperature sensor and a heater attached. The disk was isolated from the rest of the inner shroud by means of polystyrene foam. In order to provide a good blackbody radiator, the lower surface of the disk was painted with black colloidal graphite paint.

3 Results and discussion

Figure 1 shows the DLTS spectrum obtained at six different temperatures, without the inner shroud fitted. The curves recorded above 40 K clearly show that the emission rate from the E2 level decreased as the temperature was lowered. However, as the temperature was decreased to below 40 K, the emission rate of the E2 remained constant despite the temperature being lowered further (see the curves recorded at 20 and 30 K). In contrast to the behaviour of the E2 level, emission from the E1 level continued to decrease as the temperature was lowered.

The broadening of the E1 peak is due to field-enhanced emission, which generally becomes more pronounced at lower temperatures. At higher temperatures, the E2 peak is also broadened. However, at temperatures below 40 K, this broadening disappeared. The disappearance of the field-effect broadening of the peak indicates that the emission rate of the defect is not significantly influenced by the electric field.

Figure 2 shows an Arrhenius plot of the data obtained, and compares it to data measured previously in an LIA-based DLTS system. At higher temperatures (above 40 K), the results obtained compare well to those obtained in other studies, however, at low temperatures significant deviations were observed.

In order to ensure that these observations were not due to an artefact in the DLTS system, measurements were performed on the EL2 in the same sample over a similar emission rate range. No similar deviations were found.

From these results, we deduce that, besides the usual thermally stimulated emission mechanism, there is another mechanism that can empty the E2. This mechanism is slow ($e_n \sim 10^{-3}$ s^{-1}) and is essentially independent of temperature. At higher temperatures, the thermal emission process is much faster than the

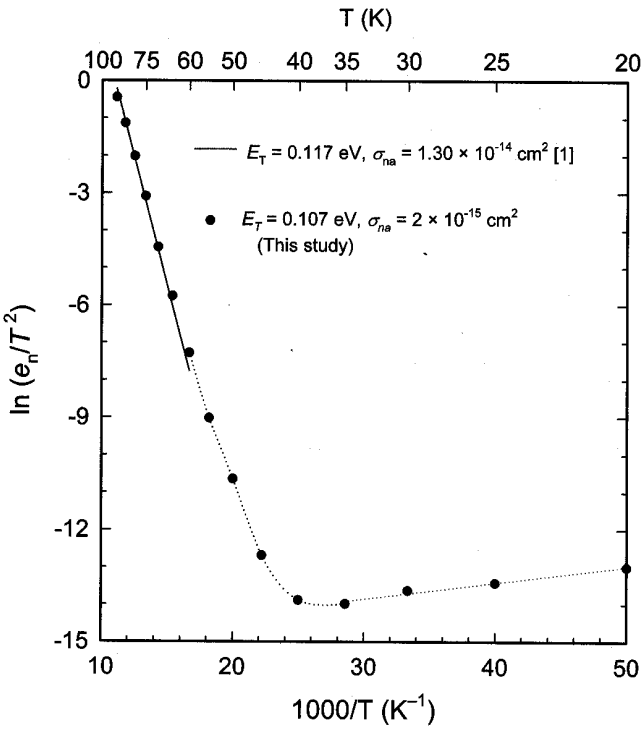

Fig. 2 Arrhenius plot of the data obtained in this study compared to data obtained in a previous study [1] in 10^{16} doped n-GaAs.

temperature independent mechanism, and the effects of the temperature independent mechanism are not observed. However, if the sample is cooled to below 40 K, the thermal emission process becomes slower than the temperature independent process. This causes the peak due to the thermal emission process to be replaced by one due to the temperature independent process.

We can also deduce that the temperature independent process is not significantly affected by the electric field in the depletion region, since the E2' peak does not show field-effect broadening.

After some experimentation, it was found that the temperature independent peak of the E2 defect disappeared when an inner shroud was fitted to the cryostat. Since there were no windows on the outer shroud of the cryostat, there was no light that could be shielded off by the inner shroud. The only radiation in the cryostat that might be blocked by the inner shroud is thermal radiation from the outer shroud. These results suggest that thermal radiation from the outer shroud is responsible for the temperature independent mechanism.

In order to investigate the possible effect of thermal radiation in more detail, a few measurements were performed with the top of the inner shroud heated to different temperatures. In this way it would be possible to investigate the effect of varying intensity thermal radiation on the sample. The results obtained in such a measurement are shown in Fig. 3, which shows some isothermal DLTS scans obtained at a measurement temperature of 33 K. In these scans, both the E1 and the E2 defects are observed. The position of the E1 does not change significantly, indicating that the sample temperature remained constant during the measurement. However, the position of the E2 level moves depending on the temperature of the top of the inner shroud. We therefore deduce that the E2' peak we observed, was due to thermal radiation from the outer shroud of the cryostat.

According to Wien's law, the peak emission of a black body radiator at 350 K is about 8 μm. This wavelength corresponds to a photon energy of 0.15 eV, which is approximately equal to the energy of the E2 below the conduction band (0.14 eV). Therefore, it seems plausible that the observed emission from the E2 may be due to these photons. It also explains why this phenomenon was not observed with the EL2 defect, which lies much deeper below the conduction band at 0.8 eV. From the above we expect that this phenomenon should be observed with other shallow defects where direct transitions are allowed.

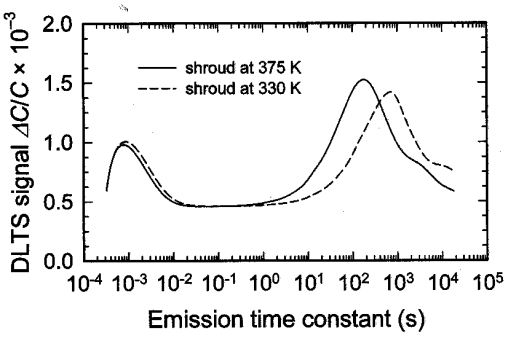

Fig. 3 Isothermal DLTS spectra recorded for the E1 and the E2 at 33 K with the top of the inner shroud heated to different temperatures.

4 Conclusion

We have shown that, under certain conditions, a temperature independent mechanism operates in addition to the usual thermal emission from the E2. At low temperatures, this temperature independent mechanism dominates over the thermal emission process, consequently only a single, temperature independent peak is observed. We have shown that this process is due to thermal radiation from the outer shroud of the cryostat, and expect the phenomenon to be observed in other shallow defects.

Acknowledgements The financial assistance of the NRF is gratefully acknowledged.

References

[1] S.A. Goodman, F.D. Auret, and W.E. Meyer, Nucl. Instr. and Meth. in Phys. Res. B **90**, 349 (1994).
[2] D.V. Lang, J. Appl. Phys. **45**, 3014 (1974)
[3] S.A. Goodman, F.D. Auret, and G. Myburg, Proc. Ninth Int. Conf. on Ion Beam Modification of Materials, Eds J.S. Williams, R.G. Elliman, and M.C. Ridgway (Elsevier, Amsterdam, 1995) p.866.
[4] D. Pons and S. Makram-Ebeid, J. Phys. (Paris) **40**, 1161 (1979).
[5] S.A. Goodman, F.D. Auret, and W.E. Meyer, Jpn. J. Appl. Phys. **33**, 1949 (1994).

7

Field dependence of the thermally activated emission rate

7.1 Introduction

In Section 2.2.3 a number of mechanisms according to which an applied electric field can enhance the emission of trapped carriers from a defect were discussed. It was mentioned that it is possible to determine a number of properties of a defect from the field dependency of its emission rate. For instance, the extent to which a defect displays the Poole-Frenkel effect is an indication of the approximate range of the defect's potential. This information can then be used to estimate the charge state of the defect and to determine whether the defect is an acceptor or a donor. At higher electric fields, many defects exhibit field-dependent emission enhancement that corresponds well with the phonon-assisted tunnelling model. In this case, curve-fitting routines can be used to determine the coupling constant between the lattice and the defect, the Huang-Rhys factor.

From a device viewpoint, it is also important to know the field-dependent emission properties of a defect. Since the application of an electric field may change the carrier emission rate of a defect by more than an order of magnitude, the electric field in a device may have significant impact on the way in which defects influence device performance.

The digital isothermal DLTS technique is ideally suited to the determination of the field dependence of the emission rate. The main advantage of this technique over the LIA-based technique is that all measurements are performed at the same temperature. It is therefore not necessary to use interpolation to estimate the emission rate of a defect at a given temperature. Furthermore, since the temperature remains constant, isothermal DLTS allows the temperature to be determined more accurately than with scanned temperature DLTS.

7.2 Publications

The digital DLTS system described in this thesis was used to determine the field dependence of a number of defects in different materials. The results of these studies are reported in the following publications, copies of which are included after this chapter. In all cases the isothermal DLTS measurements, the modelling and the curve fitting was performed by the present author.

1. Auret FD, Goodman SA and Meyer WE 1998 Field enhanced emission kinetics of an as-grown defect in RMBE grown n-GaN. *Proc. 24th Int. Conf. Phys. Semicond.* ed D Gershoni (Singapore: World Scientific)

2. Goodman SA, Auret FD, Meyer WE, Koschnick FK, Spaeth J-M, Beaumont B and Gibart P 1998 Deep level defects introduced in n-GaN by 5.4 MeV He-ions *Proc. 24th Int. Conf. Phys. Semicond.* ed D Gershoni (Singapore: World Scientific)

3. Goodman SA, Auret FD, Koschnick FK, Spaeth J-M, Beaumont B and Gibart P 1999 Field-enhanced emission rate and electronic properties of a defect introduced in n-GaN by 5.4 MeV He-ion irradiation *Appl. Phys. Lett.* **74** 809

4. Deenapanray PNK, Meyer WE and Auret FD 1999 Electric-field-enhanced emission and annealing behaviour of electron traps introduced in n-Si by low-energy He-ion bombardment *Semicond. Sci. Technol.* **14** 41

FIELD ENHANCED EMISSION KINETICS OF AN AS-GROWN DEFECT IN RMBE GROWN n-GaN

F.D. AURET, S.A. GOODMAN AND W.E. MEYER

Department of Physics, University of Pretoria, Pretoria, 0002, South Africa
E-mail: fauret@scientia.up.ac.za

We report on the enhanced emission kinetics of an as-grown defect in MBE grown n-GaN. This defect which is positioned 0.247 ± 0.005 eV below the conduction band and has an apparent capture cross-section of 3×10^{-13} cm^2. It exhibits an emission rate which depends on the electric field strength in the space-charge region. The emission rate increases from 6 s^{-1} at a field of 1×10^7 Vm^{-1} within the space-charge region to 10 s^{-1} when the electric field strength within this region is 5×10^7 V m^{-1}. This field dependence could not be explained by the Poole-Frenkel enhanced emission from a coulombic well, indicating that this defect is not a donor. This result does not support previously published results regarding the nature of this defect.

1 Introduction

An electric field can have a pronounced effect on emission from defects in semiconductors [1]. The negative aspect usually associated with electric field enhanced emission is that it results in inaccurate activation energy measurements and since the electric field increases with the doping density, this effect is especially pronounced in semiconductors with a carrier density above 10^{17} cm^{-3}. However, electric field assisted emission from deep level defects often assists in providing a better insight into several aspects of the defects being characterized. Firstly, if the Poole-Frenkel model for emission from a Coulomb potential can describe the enhanced emission data well, then it implies that the defect is a donor in n-type material, or an acceptor in p-type material. For example, the characteristic Poole-Frenkel field enhancement has been instrumental in identifying the inverted order of acceptor and donor levels of monatomic hydrogen in Si [2]. Secondly, it has been shown that the enhanced emission from some defects, including the well-known EL2 and some radiation-induced defects in GaAs, can be described by phonon-assisted tunneling. By fitting the experimental data to this model, the Huang-Rhys factor of the defect can be extracted from which one finds an indication of the lattice relaxation associated with carrier capture and emission.

In this paper, we investigate the electric field dependence of the emission rate of a defect in n-GaN grown by means of reactive molecular beam epitaxy (RMBE).

2 Experimental

For this study, 2 μm thick GaN epitaxial layers were grown on a 250 Å AlN buffer layer on sapphire by reactive molecular beam epitaxy (RMBE). The samples were cleaned in boiling aqua regia and degreased. Hereafter the oxide layer was removed using a 50% HCl solution for 10 seconds. Composite Ti/Al/Ni/Au (150 Å/2200 Å/ 400 Å/500 Å) ohmic contacts were deposited, followed by a 5 minute annealing at 500 °C in an inert atmosphere. Schottky contacts, 0.5 mm in diameter, were formed by resistively depositing 3000-Å gold through a mask. The carrier density of the material was determined by CV measurements as 2×10^{17} cm^{-3}.

Defect characterization was performed by means of a lock-in amplifier-based (LIA) deep level transient spectroscopy (DLTS) system. The DLTS signatures (energy level, E_T, and the apparent capture cross-section, σ_{na}) were determined at a quiescent reverse bias (V_r) of 1.0 V and a filling pulse (V_p) if 0.5 V. Isothermal DLTS, with a constant reverse bias and an incrementing filling pulse was used to determine the field dependence of the emission rate of the EM1. The results were analyzed according to the method of Zohta et al [3].

3 Results and discussion

The DLTS spectrum of the material shown in Figure 1 shows one dominant defect level, the EM1, which had an E_T and σ_{na} of 0.247 eV and 3×10^{-13} cm^2 respectively. The EM1 is presumably the same as the E_1 defect observed in RMBE grown GaN by Fang et al [4] with an E_T and σ_{na} equal to 0.21 eV and 1.26×10^{-14}. We ascribe the higher activation energy obtained by us to the lower electric field used in our measurements. Fang et al. speculated that, based on comparison between their data and that obtained for electron irradiated GaN, that E_1 is related to N-vacancies in GaN. Look et al. [5] have used Hall effect measurements to show that the N-vacancy in GaN is a donor-type defect.

In an attempt to determine the nature of the main defect observed in our study, the field dependence of the EM1 emission rate was determined. The results of these measurements are shown in Figure 2. In order to establish the potential associated with this defect the experimental data was modelled making use of various simple defect potential models. Since one-dimensional calculations grossly overestimate the field enhancement, we considered Poole-Frenkel enhancement from three-dimensional potentials only [6].

As shown in Figure 2, the data could not be explained by Poole-Frenkel enhancement from a coulombic well [7]. This dependence would imply that there is a coulombic attraction between the carrier and the defect, indicating that it is a donor in n-type material [8]. This is a strong indication that the defect is an acceptor.

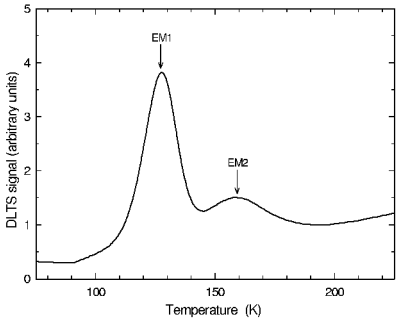

Figure 1. DLTS spectra of the as-grown sample. The spectrum was recorded at 46 Hz with V_r = 1.0 V and V_p = 1.2 V.

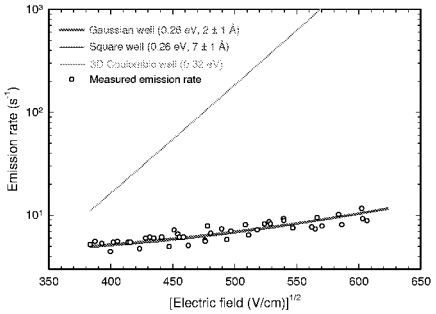

Figure 2. The experimental and modeled emission kinetics of the EM1 defect as a function of electric field strength in the space charge region.

A much better fit was obtained for a spherically symmetric square well [7] (depth 0.26 eV and radius 7 ± 2 Å) and a gaussian well [9] (depth 0.26 eV and characteristic width of 2 ± 0.5 Å). The difference between the field enhanced emission due to the gaussian well and that due to the square well was not large enough to allow a distinction to be made. However in both cases the dimensions of the well are of the order of a lattice parameter, therefore we conclude that the defect is a point defect. The slightly higher value of E_T determined from the modeling as compared to the experimental value is an indication that the defect energy determination was influenced by the high electric field in the highly doped material.

As mentioned previously, Fang et al. found a defect, the E_1, which we believe to be the same as the EM1 we observed. They suggest that the E_1 is related to the N-vacancy which is a donor-type defect. However, our results indicate that the EM1 defect is an acceptor. Therefore we have to assume that, either the EM1 we measured is not the same as the E_1, or the E_1 is not a donor and therefore not a N-vacancy.

4 Summary

We have determined the electronic properties of an as-grown defect in RMBE grown GaN which is positioned 0.247 eV below the conduction band with an apparent capture cross-section of 3×10^{-13} cm^2. Modeling of the emission kinetics in field strengths ranging from 1×10^5 to 4×10^5 V/cm has shown that the defect potential can not be described by a one- or a three-dimensional coulombic well. However, a square well with a depth of 0.26 eV and a radius of 7 ± 1 Å and a gaussian well of depth 0.26 eV and characteristic width 2.0 ± 1 Å both describe the enhanced emission very well. Hence we conclude from the physical dimensions of the modelled potential wells and the fact that EM1 does not exhibit the proportional

dependence on $F^{½}$ characteristic of a coulombic well that EM1 is a point defect which has acceptor like character.

Acknowledgments

We gratefully acknowledge the financial assistance of the South African Foundation for Research Development. We thank G. Myburg for assistance with the ohmic contact fabrication.

References

1. J. Frenkel, *Phys. Rev.* **54**, 657 (1938).
2. N.M. Johnson, C. Herring and C.G. van de Walle, *Phys. Rev. Lett.* **73**, 130 (1994).
3. Y. Zohta, and M.O. Watanabe, *J. Appl. Phys.* **53**, 1809 (1982).
4. Z-Q. Fang, D.C. Look, W. Kim, Z. Fan, A. Botchkarev and H Morkoç, *Appl. Phys. Lett.* **72** 2277 (1998).
5. D.C. Look, D.C. Reynolds, J.W. Hemsky, J.R. Sizelove, R.L. Jones, and R.J. Molnar, *Phys. Rev. Lett*. **79**, 2273 (1997).
6. N. Baber, and M.Z. Iqbal, *J. Appl. Phys.* **62**, 4471 (1987).
7. J. L. Hartke, *J. Appl. Phys.* **39**, 4871 (1968).
8. J. Bourgoin and M. Lannoo, Point Defects in Semiconductors II, Experimental Aspects, ed. M. Cardona (Springer Series vol. 35, Springer Verlag, 1983)
9. Q.S. Zhu, K. Hiramatsu, N. Sawaki, I. Akasaki, and X.N. Liu, *J. Appl. Phys.* **73**, 771 (1993).

DEEP LEVEL DEFECTS INTRODUCED IN n-GaN BY 5.4 MeV He-IONS

S.A. GOODMAN, F.D. AURET AND W.E. MEYER
Department of Physics, University of Pretoria, Pretoria, 0002, South Africa
E-mail: sgoodman@scientia.up.ac.za

F.K. KOSCHNICK AND J.-M. SPAETH
Fachbereich Physik, University of Paderborn, Paderborn, Germany

B. BEAUMONT AND P. GIBART
CRHEA-CNRS Valbonne, France

We have used deep level transient spectroscopy (DLTS) to characterise a deep level defect, the ER3, in unintentionally doped OMVPE grown GaN exposed to high energy (5.4 MeV) He-ions. The ER3 defect was introduced at a rate of 3270 ± 50 cm^{-1} and, under low electric field conditions, it has an energy level of 0.196 ± 0.004 eV below the conduction band and an apparent capture cross-section of 3.5 ± 1 × 10^{-15} cm^2. We found that the emission rate of the defect depends on the electric field strength in the space-charge region. This field dependence of the emission rate could be modelled according to the Poole Frenkel distortion of a square well with a radius of 20 ± 2 Å or a Gaussian well with a characteristic width of 6.0 ± 1 Å. Hence, we conclude that the ER3 is a point defect which appears to have acceptor like character.

1 Introduction

Gallium nitride, a direct wide bandgap semiconductor, has attracted considerable attention because of its applications in blue, green and ultraviolet light emitting diodes, detectors, and blue lasers. Because of its low thermal generation rates and high breakdown fields, an inherent property of wide bandgap semiconductors, it also has applications in the field of high temperature and power electronics [1]. The fabrication of electronic devices requires the definition of the device active area, which, for epitaxially based processes, is typically accomplished by mesa etching or implant isolation. It was found that He implantation-induced damage produced high resistivity GaN at a fluence that is compatible with photoresist masking techniques [2]. He-ion irradiation has the advantage over electron irradiation in its ability to isolate selected areas for device definition and is also suitable for carrier lifetime tailoring [3].

In this paper, we present the introduction rate and electrical properties of a deep level defect introduced by 5.4 MeV He-ions in n-GaN.

2 Experimental

For this study, 5μm thick GaN epitaxial layers were grown on a 250 Å buffer layer on sapphire by metal-organic vapour phase epitaxy (MOVPE) and exposed to 5.4 MeV He-ions from an ^{241}Am radio-nuclide source. The samples were cleaned in boiling aqua regia and degreased [4]. Hereafter the oxide layer was removed using a 50% HCl solution for 10 seconds [5]. Composite Ti/Al/Ni/Au (150 Å/2200 Å/ 400 Å/500 Å) ohmic contacts [6] were deposited, followed by a 5 minute annealing at 500 °C in an inert atmosphere. Schottky contacts, 0.5 mm in diameter, were formed by resistively depositing 3000 Å of gold through a mask.

Defect characterisation was performed by means of a lock-in-amplifier-based (LIA) deep level transient spectroscopy (DLTS) system. The DLTS signatures (energy level, E_T, and the apparent capture cross-section, σ_{na}) were determined at a quiescent reverse bias (V_r) of 1.0 V and a filling pulse (V_p) of 0.5 V. Isothermal DLTS, with a constant reverse bias and an incrementing filling pulse was used to determine the field dependence of the emission rate of ER3. The results were analyzed according to the method of Zohta et al [7].

3 Results and discussion

The DLTS spectrum of the as-grown material [Figure 1 curve (a)] contained two defect levels. The E02 had an E_T and σ_{na} of 0.27 eV and 8.85 × 10^{-15} cm^2 respectively while the E05 had an E_T and σ_{na} of 0.607 eV and 1 × 10^{-14} cm^2 respectively. The E02 and E05 defects are presumably the same as the E1 and E2 levels detected previously [8] in as-grown hydride vapour-phase epitaxially grown material.

After irradiation with He-ions, the DLTS spectrum [curve (b)] shows an additional defect, ER3, introduced at a rate of 3270 ± 200 cm^{-1} and positioned 0.196 ± 0.004 eV below the conduction band with an apparent capture cross-section of 3.5 × 10^{-15} cm^2. The electronic properties of the ER3 are similar to a defect found by Fang et al [9] in electron irradiated GaN, for which E_T and σ_{na} were 0.18 eV and 2.5 × 10^{-15} cm^2 respectively. The small discrepancy in the activation energy of the defects can be accounted for by field enhanced emission from the defect reported by Fang et al as their "signature" was determined under higher field conditions.

The field dependence of the emission from the defect is shown in Figure 2. In order to establish the potential associated with this defect the experimental data was modelled making use of various simple defect potential models. Since one-dimensional calculations grossly overestimate the field enhancement [10], we considered Poole-Frenkel enhancement from three dimensional potentials only.

As shown in Figure 2, the data could not be explained by Poole-Frenkel enhancement from a coulombic well [11]. This dependence would imply that there

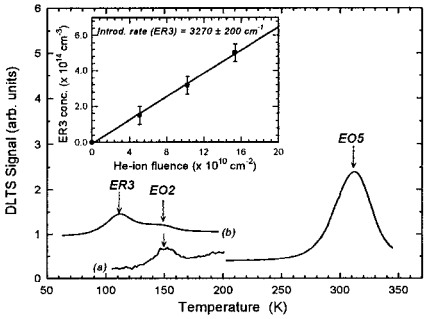

Figure 1. DLTS spectra of the unirradiated n-GaN [curve (a)] and the material exposed to 5.4 MeV He-ions [curve(b)]. The inset depicts the concentration of the He-ion induced defect ER3 a function of the incident He-ion fluence.

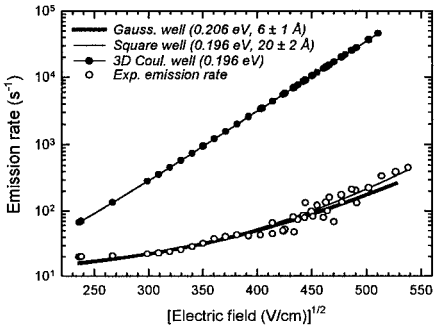

Figure 2. The experimental and modeled emission kinetics of defect ER3 as a function of electric field strength in the space charge region.

is a coulombic attraction between the carrier and the defect, indicating that it is a donor in n-type material [12]. We therefore assume that the defect is an acceptor. Further evidence for the acceptor nature of the ER3 are direct capture cross-section measurements which indicate a very low capture cross-section of 1×10^{17} cm^{-2}.

A much better fit was obtained for a spherically symmetric square well [11] (depth 0.196 eV and radius 20 ± 2 Å), while the best fit was obtained assuming a gaussian well [13] (depth 0.206 eV and characteristic width of 6.0 ± 1 Å). The difference between the field enhanced emission due to the gaussian well and that due to the square well was not large enough to allow a distinction to be made. However in both cases the dimensions of the well are of the order of a lattice parameter, therefore we conclude that the defect is a point defect.

We believe that the ER3 is the same defect as E previously observed by Fang et al. [9] who speculated that the defect may be related to the N-vacancy. However, Look et al. [14] have shown that the N-vacancy is a donor. This contradiction warrants further investigation.

4 Summary

We have determined the electronic properties of a defect introduced at a rate of 3270 ± 200 cm^{-1} by 5.4 MeV He-ions in n-GaN grown by OMVPE and is positioned 0.196 ± 0.004 eV below the conduction band. A defect with similar electronic properties and a considerably lower introduction rate has been observed after electron irradiation [9]. Modeling of the emission kinetics in field strengths ranging from 4.9×10^4 to 3×10^5 V/cm has shown that the defect potential is not a one- or a three-dimensional coulombic well. However, a square well with a depth of 0.196 eV and a radius of 20 ± 2 Å and a gaussian well of depth 0.206 eV and

characteristic width 6.0 ± 1 Å both describe the enhanced emission very well. Hence we conclude from the physical dimensions of the modelled potential wells and the fact that ER3 does not exhibit the proportional dependence on $F^{½}$, that ER3 is a point defect which has acceptor-like character.

Acknowledgments

We gratefully acknowledge the financial assistance of the South African Foundation for Research Development and the Forschungszentrum Jülich, International Bureau. We thank G. Myburg for assistance with the ohmic contact fabrication.

References

1. H. Morkoc, S. Strite, G.B. Gao, M.E. Lin, B. Sverdlov, and M. Burns, *J. Appl. Phys.* **76**, 1363 (1994).
2. S.C. Binari, H.B. Dietrich, G. Kelner, L.B. Rowland, K. Doverspike, and D.K. Wickenden, *J. Appl. Phys.* **78**, 3008 (1995).
3. D.C. Sawko, and J. Bartko, *IEEE Trans. Nucl. Sci.* **30**, 1756 (1983).
4. P. Hacke, T. Detchprohm, K. Hiramatsu, and N. Sawaki, *Appl. Phys. Lett.* **63**, 2676 (1993).
5. J.K. Sheu, Y.K. Su, G.C. Chi, W.C. Chen, C.Y. Chen, C.N. Huang, J.M. Hong, Y.C. Yu, C.W. Wang, and E.K. Lin, *J. Appl. Phys.* **83**, 3172 (1998).
6. S. Ruminov, Z. Liliental-Weber, J. Washburn, K.J. Duxstad, E.E. Haller, Z.-F. Fan, S.N. Mohammed, W. Kim, A.E. Botchkarev, and H. Morcoc, *Appl. Phys. Lett.* **69**, 1556 (1996).
7. Y. Zohta, and M.O. Watanabe, *J. Appl. Phys.* **53**, 1809 (1982).
8. P. Hacke, T. Detchprohm, K. Hiramatsu, N. Sawaki, K. Tadatomo, and K. Miyake, *J. Appl. Phys.* **76**, 304 (1994).
9. Z.-Q. Fang, J.W. Hemsky, D.C. Look, and M.P. Mack, *Appl. Phys. Lett.* **72**, 448 (1998).
10. N. Baber, and M.Z. Iqbal, *J. Appl. Phys.* **62**, 4471 (1987).
11. J. L. Hartke, *J. Appl. Phys.* **39**, 4871 (1968).
12. J. Bourgoin and M. Lannoo, Point Defects in Semiconductors II, Experimental Aspects, ed. M. Cardona (Springer Series vol. 35, Springer Verlag, 1983)
13. Q.S. Zhu, K. Hiramatsu, N. Sawaki, I. Akasaki, and X.N. Liu, *J. Appl. Phys.* **73**, 771 (1993).
14. D.C. Look, D.C. Reynolds, J.W. Hemsky, J.R. Sizelove, R.L. Jones, and R.J. Molnar, *Phys. Rev. Lett.* **79**, 2273 (1997).

APPLIED PHYSICS LETTERS VOLUME 74, NUMBER 6 8 FEBRUARY 1999

Field-enhanced emission rate and electronic properties of a defect introduced in *n*-GaN by 5.4 MeV He-ion irradiation

S. A. Goodman[a] and F. D. Auret
Physics Department, University of Pretoria, Pretoria, 0002, South Africa

F. K. Koschnick and J.-M. Spaeth
Fachbereich Physik, Universität GH Paderborn, Paderborn, Germany

B. Beaumont and P. Gibart
CRHEA-CNRS Valbonne, France

(Received 22 July 1998; accepted for publication 3 December 1998)

A deep level defect ER3, introduced in *n*-GaN by high energy (5.4 MeV) He ions, was characterized by deep level transient spectroscopy (DLTS). This defect, 0.196 ± 0.004 eV below the conduction band, with an apparent capture cross-section of $3.5\pm1\times10^{-15}$ cm^2, is introduced uniformly in the region profiled by DLTS at a rate of 3270 ± 200 cm^{-1}. The emission rate of this defect depends on the electric field strength in the space-charge region. This emission rate is modeled according to the Poole–Frenkel distortion of a square well with a radius of 20 ± 2 Å or alternatively, a Gaussian well with a characteristic width of 6.0 ± 1 Å. Hence, we conclude that ER3 is a point defect which has a field dependence not explained by the classical Poole–Frenkel enhancement. © *1999 American Institute of Physics.* [S0003-6951(99)02906-X]

Gallium nitride, a direct wide band gap semiconductor, has attracted considerable attention because of its applications in blue, green, and ultraviolet light emitting diodes, detectors, and blue lasers.[1] Because of its low thermal generation rates and high breakdown fields, an inherent property of wide band gap semiconductors, it also has applications in the field of high temperature and power electronics.[2] The fabrication of electronic devices requires the definition of the device active area. For epitaxially based processes, active area definition is typically accomplished by using mesa etching or implant isolation. Both H and He implantation damage has been used in GaN-based microelectronic processes.[3,4] It was found that He implantation-induced damage produced high resistivity GaN at a fluence that is compatible with photoresist masking techniques.[3] He-ion irradiation has the advantage over electron irradiation in its ability to isolate selected areas for device definition and also in carrier lifetime tailoring.[5] Deep level transient spectroscopy[6] (DLTS) is commonly used to study the electrical properties of deep levels within the space charge region of a Schottky barrier diode (SBD). It is generally assumed that the emission of carriers from deep levels is a purely thermal process. However, this may not always be the case and inaccurate defect characteristics may be calculated if one assumes only thermal emission. On the other hand, accurate measurements of the field enhancement of emission rates can lead to a model of the localized defect potential of the deep center thus providing vital insight into the nature of the defect states in the semiconductor.[7]

In this letter, we present the introduction rate, electrical properties, and the dependence of the emission rate on electric field strength of a deep level defect introduced by 5.4 MeV He ions in *n*-GaN.

For this study, GaN epitaxial layers 5 μm thick grown at 1080 °C on a 250 Å GaN buffer layer on sapphire by metal-organic vapor phase epitaxy (MOVPE) were exposed to 5.4 MeV He ions from a ^{241}Am radio-nuclide source. The nominally undoped GaN epitaxial layer had a free carrier concentration of approximately $2.2\pm0.2\times10^{16}$ cm^{-3}. After boiling the samples in aqua-regia for ten minutes the samples were degreased.[8] Prior to ohmic contact fabrication the oxide layer was removed from the sample surface using a HCl:H_2O (1:1) solution for 10 s.[9] The composite ohmic contact layer[10] was Ti/Al/Ni/Au (150 Å/2200 Å/400 Å/500 Å). The contact fabrication was followed by a five minute anneal at 500 °C in an inert gas atmosphere. Gold (Au) SBDs, 0.5 mm in diameter and 3000-Å-thick were resistively deposited, these diodes had a reverse leakage current of the order of 10^{-10} A at 1 V and ideality factors between 1.05 and 1.10. The samples were exposed to 5.4 MeV He ions by placing them on an ^{241}Am foil. The activity of the radionuclide being 192 μCi cm^{-2} and the dose rate was 7.1×10^6 cm^{-2} s^{-1}. A two-phase lock-in-amplifier-based (LIA) deep level transient spectroscopy (DLTS) system was used for the defect characterization. All DLTS ''signatures'' (activation energy, E_T and apparent capture cross-section, σ_{na}) were determined using a quiescent reverse bias (V_r) of 1.0 V and a filling pulse (V_p) of 0.5 V. DLTS depth profiling was performed by recording spectra at fixed quiescent reverse bias (V_r) but incrementing the forward bias (V_p) in small steps from one scan to the next. The approach of Zohta *et al.*[11] was then used to obtain the defect concentration as a function of depth below the interface. In order to simplify the determination of the emission kinetics of ER3 at different electrical field strengths in the space-charge region, isothermal DLTS was used.

Prior to He-ion irradiation, the MOVPE grown material contained two defects, $E02$ and $E05$ as illustrated in curve

[a]Electronic mail: sgoodman@nsnpert.up.ac.za

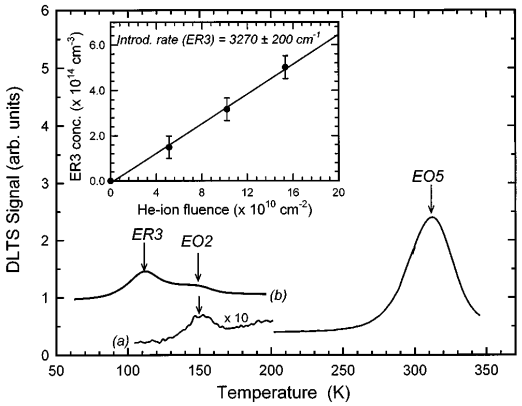

FIG. 1. DLTS spectra of the unirradiated n-GaN [curve (a)] and the material exposed to 5.4 MeV He ions [curve (b)]. The inset depicts the concentration of the He-ion induced defect ER3 as function of the incident He-ion fluence.

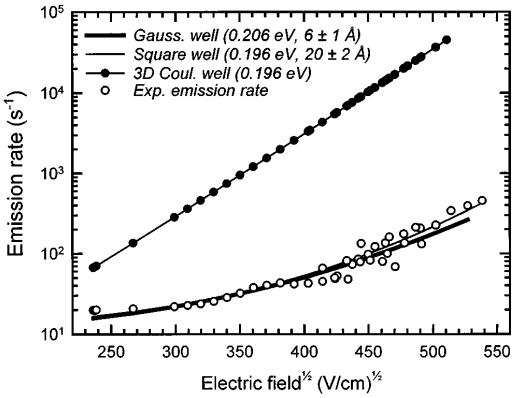

FIG. 2. The experimental and modeled emission kinetics of defect ER3 as a function of electric field strength in the space charge region.

(a) of Fig. 1. Defect $E02$, which is positioned 0.27 eV below the conduction band ($E_c-0.27$ eV) with an apparent capture cross-section of 8.5×10^{-15} cm^2, is believed to be the same as defect, $E1$[11] with a DLTS signature of 0.264 ± 0.01 eV and 1.6×10^{-15} cm^{-2} detected in as-grown hydride vapor-phase epitaxially grown material. A defect, E_2, has been detected in *unirradiated* MOVPE grown n-GaN, with an activation energy of 0.18 eV.[12] Defect $E05$, which has an activation energy of 0.607 eV with an apparent capture cross-section of 1×10^{-14} cm^2 is presumably the same as defect $E2$[13] detected in as-grown hydride vapor-phase epitaxially grown material with an activation energy of 0.580 ±0.017 eV with an apparent capture cross section of 2.9×10^{-15} cm^2.

After exposing n-GaN to 5.4 MeV He ions an additional defect, $ER3$ [curve (b), Fig. 1] was observed, this defect has a ''low field'' (7.6×10^4 V/cm) DLTS ''signature'' of $E_c-0.196\pm0.004$ and σ_{na} $3.5\pm1\times10^{-15}$ cm^2. There has been very few detailed investigations on the influence of particle irradiation on the electrical and optical properties of n-type GaN. Fang *et al.*,[14] irradiated n-GaN with 1 MeV electrons to a dose of 5×10^{14} and $\sigma_{na}1\times10^{15}$ cm^{-2}. A defect labeled E, for which the apparent parameters E_T and σ_{na} are 0.18 eV and 2.5×10^{-15} cm^2, respectively, was introduced at a rate of 0.2 cm^{-1}. It was speculated, taking into account the possibility of a temperature dependent capture cross-section, that this defect could possibly be the nitrogen vacancy (V_N, $E_c-0.07$ eV). The electronic properties of this defect and ER3 are similar. The small discrepancy in their activation energy could be accounted for by slight field enhanced emission of the defect reported by Fang *et al.*[14] as their defect ''signature'' was determined under higher electric field conditions.

In Fig. 2 the experimentally measured emission rate of ER3 as a function of the square root of the electric field in the space charge region is shown. In order to establish the potential associated with this defect the experimental data was modeled making use of various simple defect potential models. It must be noted, that the one-dimensional calculation grossly overestimated the field enhancement, as is well known.[15] Therefore, we firstly, consider the three-dimensional Poole–Frenkel description of electric field assisted thermal emission from a Coulombic well. According to this model,[16] the emission rate can be described by

$$e(F)=e(0)\left\{\left(\frac{kT}{\beta\sqrt{F}}\right)^2\left[1+\left(\frac{\beta\sqrt{F}}{kT}-1\right)\times e^{(\beta\sqrt{F}/kT)}\right]+\frac{1}{2}\right\}, \tag{1}$$

where $e(0)$ is the emission rate at zero electric field, k is Boltzmann's constant, T is the absolute temperature, and

$$\beta=\left(\frac{q^3}{\pi\epsilon}\right)^{1/2}. \tag{2}$$

It is evident from Fig. 2 that this particular potential does not suitably explain the experimentally measured emission enhancement. It must be noted that the characteristic dependence of the emission rate (e) on electric field (F) in the case of the one-dimensional Poole–Frenkel effect for a Coulombic well, namely that $\log e$ is proportional to $F^{1/2}$, is frequently used by experimentalists to distinguish between donor and acceptor defects. The linearity of this dependence is characteristic of a charge leaving a center of opposite sign. In n-type material this would imply a donor type defect, whereas, in p-type material this would imply an acceptor type defect.[7] It must be noted that the determination of the electronic type should be approached with caution as was expressed in the paper by Buchwald *et al.*,[17] who reported on the revised Poole–Frenkel effect for EL2 in GaAs.

Second, the Gaussian well was considered as a possible potential description for ER3. The enhanced emission rate in this case is[18]

$$e(F)=2\pi e(0)+\left\{\exp\left(\frac{V_0\exp(-r_0^2/\alpha^2)}{kT}\right)\frac{kT}{qFr_0}\times\left[\exp\left(\frac{qFr_0}{kT}\right)-1\right]+1\right\}, \tag{3}$$

where r_0 is the top of the distorted well where $\delta E/\delta r=0$. The resulting equation is nonlinear in r_0, F, α, and V_0, and has, therefore, been solved iteratively for each set of these

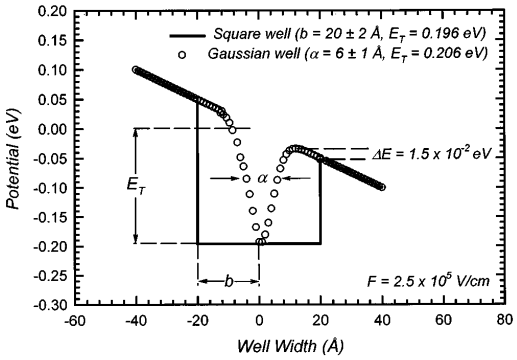

FIG. 3. The reduction in potential for a Gaussian and a square well, when the electric field strength in the space charge region is 2.5×10^5 V/cm.

values before calculating $e(F)$ using Eq. (3). A good fit is obtained when a characteristic width of 6.0 ± 1 Å and a potential of 0.206 eV is used.

Third, the spherically symmetric square well potential of radius b was investigated. The variation of emission rate $[e(f)]$ with electric field of a square well of radius b is[16]

$$e(F)=e(0)\{(kT/2qFb)[\exp(qFb/kT)-1]+1/2\}. \quad (4)$$

Using a potential equal to the experimentally determined activation energy, namely, 0.196 eV and a well with a radius of 20 ± 2 Å, a good fit is obtained between the experimentally measured emission rates and the modeled points.

It would appear that the square well and the Gaussian well with their particular physical dimensions discussed both provide an adequate description of defect ER3 detected after high energy He-ion irradiation. In an attempt to understand how both potentials describe the experimental results, a comparison of the distortion of these potentials at a reasonably high (2.5×10^5 V/cm) electric field strength was investigated. Figure 3 schematically represents the distortion of a square and a Gaussian well. It is clear from this figure that using either a Gaussian or a square well with the specified physical attributes can adequately describe the enhanced emission kinetics of ER3. The fact that the field enhanced emission from ER3 can not be adequately described by a Coulombic well indicates that ER3 is not a donor type defect but an acceptor type defect. The existence of another acceptor type defect not expected to exist in large numbers in as-grown material, namely, N_1 was experimentally shown by Look *et al.*[19]

In summary, we have determined the electronic properties of a defect introduced at a rate of $3270\pm200\,\mathrm{cm}^{-1}$ by 5.4 MeV He ions in n-GaN grown by organometallic vapor phase epitaxy (OMVPE). This defect which is positioned 0.196 ± 0.004 eV below the conduction band is introduced uniformly in the region probed by DLTS. A defect with similar electronic properties and a considerably lower introduction rate has been observed after electron irradiation.[12] Modeling of the emission kinetics in field strengths ranging from 4.9×10^4 to 3×10^5 V/cm has shown that the defect potential is not a one- or a three-dimensional Coulombic well. However, a square well with a depth of 0.196 eV and a radius of 20 ± 2 Å and a Gaussian well of depth 0.206 eV and characteristic width 6.0 ± 1 Å both describe the enhanced emission very well. Hence we conclude from the physical dimensions of the modeled potential wells and the fact that ER3 does not exhibit the proportional dependence on $F^{1/2}$ that is classically used to determine the electronic type of the defect.

The authors gratefully acknowledge the financial assistance of the South African Foundation for Research Development and the Forschungszentrum Jülich, International Bureau. They thank G. Myburg for assistance with the ohmic contact fabrication and W. E. Meyer for assistance with the isothermal DLTS measurements.

[1] S. Nakamura and G. Fasol, *The Blue Laser Diode* (Springer, New York, 1997).
[2] H. Morkoc, S. Strite, G. B. Gao, M. E. Lin, B. Sverdlov, and M. Burns, J. Appl. Phys. **76**, 1363 (1994).
[3] S. C. Binari, H. B. Dietrich, G. Kelner, L. B. Rowland, K. Doverspike, and D. K. Wickenden, J. Appl. Phys. **78**, 3008 (1995).
[4] S. J. Pearton, C. B. Vartuli, J. C. Zolper, C. Yuan, and R. A. Stall, Appl. Phys. Lett. **67**, 1435 (1995).
[5] D. C. Sawko and J. Bartko, IEEE Trans. Nucl. Sci. **30**, 1756 (1983).
[6] D. V. Lang, J. Appl. Phys. **45**, 3023 (1974).
[7] J. Bourgoin and M. Lannoo, *Point Defects in Semiconductors II, Experimental Aspects*, edited by M. Cardona, Springer Series, Vol. 35 (Springer, New York, 1983).
[8] P. Hacke, T. Detchprohm, K. Hiramatsu, and N. Sawaki, Appl. Phys. Lett. **63**, 2676 (1993).
[9] J. K. Sheu, Y. K. Su, G. C. Chi, W. C. Chen, C. Y. Chen, C. N. Huang, J. M. Hong, Y. C. Yu, C. W. Wang, and E. K. Lin, J. Appl. Phys. **83**, 3172 (1998).
[10] S. Ruminov, Z. Liliental-Weber, J. Washburn, K. J. Duxstad, E. E. Haller, Z.-F. Fan, S. N. Mohammed, W. Kim, A. E. Botchkarev, and H. Morcoç, Appl. Phys. Lett. **69**, 1556 (1996).
[11] Y. Zohta and M. O. Watanabe, J. Appl. Phys. **53**, 1809 (1982).
[12] W. Götz, N. M. Johnson, H. Amano, and I. Akasaki, Appl. Phys. Lett. **65**, 463 (1994).
[13] P. Hacke, T. Detchprohm, K. Hiramatsu, N. Sawaki, K. Tadatomo, and K. Miyake, J. Appl. Phys. **76**, 304 (1994).
[14] Z.-Q. Fang, J. W. Hemsky, D. C. Look, and M. P. Mack, Appl. Phys. Lett. **72**, 448 (1998).
[15] N. Baber and M. Z. Iqbal, J. Appl. Phys. **62**, 4471 (1987).
[16] J. L. Hartke, J. Appl. Phys. **39**, 4871 (1968).
[17] W. R. Buchwald and N. M. Johnson, J. Appl. Phys. **64**, 958 (1988).
[18] Q. S. Zhu, K. Hiramatsu, N. Sawaki, I. Akasaki, and X. N. Liu, J. Appl. Phys. **73**, 771 (1993).
[19] D. C. Look, D. C. Reynolds, J. W. Hemsky, J. R. Sizelove, R. L. Jones, and R. J. Molnar, Phys. Rev. Lett. **79**, 2273 (1997).

Semicond. Sci. Technol. **14** (1999) 41–47. Printed in the UK PII: S0268-1242(99)94350-X

Electric-field-enhanced emission and annealing behaviour of electron traps introduced in n-Si by low-energy He ion bombardment

P N K Deenapanray†‡, W E Meyer‡ and F D Auret‡

† Department of Electronic Materials Engineering, Australian National University, Canberra, ACT 0200, Australia
‡ Department of Physics, University of Pretoria, Pretoria 0002, South Africa

Received 15 May 1998, in final form 8 September 1998, accepted for publication 30 September 1998

Abstract. The isochronal annealing and electric-field-enhanced emission properties of three defects (EHe203, EHe584 and EHe211), observed in low-energy He-ion bombarded n-Si, were studied using deep level transient spectroscopy. EHe203 ($E_C - 0.20$ eV) and EHe584 ($E_C - 0.58$ eV) were thermally stable up to ~400 °C after which their removal was accompanied by the introduction of a secondary defect EHe211 ($E_C - 0.21$ eV). EHe211 was thermally stable at 650 °C. The emission rate of EHe203 was significant for electric fields above 4×10^4 V cm^{-1}, and was enhanced by over 3 orders of magnitude for a corresponding three-fold increase in electric field. The emission rate of EHe211 was only weakly field dependent over the electric field range studied, while that of EHe584 remained constant for electric fields between 3×10^4 and 9×10^4 V cm^{-1}. EHe584 has been proposed to be an acceptor-type defect. It was found that square wells of radii 57 Å and 40 Å described the potentials induced by EHe203 and EHe211, respectively, reasonably well. Alternatively, Gaussian potential wells with $\alpha = 20$ Å and $V_0 = 0.30$ eV (EHe203) and $\alpha = 12$ Å and $V_0 = 0.35$ eV (EHe211) could be used to fit our experimental data.

1. Introduction

Low-energy (0.2–2000 keV) noble gas ions (NGIs) are widely used during several microelectronics device fabrication steps, including ion beam etching, reactive ion etching and sputter deposition for metallization. The energetic ions create damage in the exposed semiconductor lattice through momentum transfer. This damage alters the electrical, optical and structural properties of the semiconductor and of devices fabricated thereon. For instance, the introduction of donor-type defects close to the crystal surface alters the barrier properties of Schottky barrier diodes fabricated on low-energy NGI-bombarded Si [1, 2]. Photoluminescence studies have shown that energy shifts in the no-phonon peak of the intrinsic I_1 defect (or W, 1.018 eV) occurred after bombarding Si with low-energy NGIs [3–5]. Those mass-dependent systematic line shifts were attributed to the incorporation of NGIs into the intrinsic defect, constituting a family of deep optical defects. Several conflicting models have been proposed for the structure of these NGI-related defects [6–8]. Using *ab initio* molecular dynamics modelling, Estreicher *et al* [9, 10] have recently proposed that the 1018 meV line was due to the neutral divacancy and that the shifted I_1 peaks were due to the incorporation of NGIs into the neutral divacancies. Despite these numerous studies, data concerning the electrical and annealing properties of deep level defects in low-energy NGI-bombarded Si are scarce.

Deep level transient spectroscopy (DLTS) [11] is commonly used to study the electrical properties of deep levels within the depletion region of a diode. It is commonly assumed that the emission of carriers from deep levels is a purely thermal process and that the internal electric field has no influence on the results. This is, however, not true and one is always cautioned against inaccurate findings from emission rate data if its dependence on electric field is not taken into account [11, 12]. The sensitivity of the emission rate to an applied electric field can be used to probe the range of a defect potential. Hence, an accurate measurement of the electric-field-enhanced emission rate from a deep level can provide valuable insight into the structure of processing-induced defects in semiconductor materials [13–15]. The successful assignment of a particular potential to a defect can be used as an input for further computer modelling of the defect structure [16].

Several studies to investigate the enhanced emission properties from defect levels in Si have made use of various defect potential models including, among others, the Poole–Frenkel coulombic well [17, 18], square well [18] and phonon assisted tunnelling [19, 20]. The one-dimensional

0268-1242/99/010041+07$19.50

Poole–Frenkel coulombic well, which relies on the linear dependence of the logarithm of the emission rate ($\ln(e)$) on the square root of electric field ($F^{1/2}$), has been the most widely used model since it enables one to distinguish whether a defect is an acceptor or donor [17]. This model has been used to describe the emission of electrons from the oxygen-related thermal donors [21] and chalcogen double donors [22] in silicon. A refinement on the one-dimensional model is the three-dimensional (3D) Poole–Frenkel coulombic potential well [18]. Walker and Sah [23] have used the spherical square well defect potential to study the electric-field-enhanced emission rate from deep levels observed in 1 MeV electron-irradiated silicon. The Gaussian well potential, which is less rigid than the square well model, has been used to study the vacancy-phosphorus-induced potential in InGaP [24].

In this paper we present results concerning the effect on an electric field on electron emission from three defects (EHe203, EHe584 and EHe211) observed in low-energy He-ion-bombarded n-Si. We show that the emission rates from EHe203 and EHe211 were enhanced by an externally applied electric field and that the effect was more pronounced for EHe203. The annealing properties of the defects are also reported. Furthermore, we demonstrate that the secondary defect EHe211 was introduced at the expense of EHe203 and EHe584 by annealing above ~400 °C.

2. Experimental procedure

Epitaxial Si, doped to 5×10^{15} P cm^{-3}, grown on an n$^+$-substrate by chemical vapour deposition, was used to investigate the annealing behaviour and electric-field-enhanced emission from EHe203, EHe584 and EHe211. The epitaxial side of the samples were bombarded with 1 keV He ions to a dose of 1×10^{12} cm^{-2} at room temperature. After chemical cleaning, Pd Schottky contacts 100 nm thick and 0.77 mm in diameter were deposited through a metal contact mask on the bombarded samples by resistive evaporation. Ohmic contacts (In–Ga eutectic mixture) were made on the n$^+$-side of the samples prior to electrical measurements.

Zero-bias (ZB) isochronal annealing was performed under Ar flow for 20 min periods from 100 to 650 °C in steps of 50 °C. DLTS spectra were recorded after each annealing cycle to monitor the defect annealing properties and the introduction of secondary defects. Difference DLTS (DDLTS) [25] was used to study the emission properties of the electron traps under externally applied electric fields. DDLTS yielded information about the defects located in a narrow spatial region, and was realized by subtracting DLTS spectra recorded at filling pulse amplitudes V_p and $V_p + \delta V_p$ (using a fixed quiescent bias V_r). The electric field dependence of the emission rates of EHe203 and EHe584 was measured on a sample annealed at 450 °C. By using $V_r = 5$ V and changing V_p from 0.5 to 5 V, the electric field could be varied between 5×10^4 and 1.5×10^5 V cm^{-1}. For EHe211, the electric field was varied between 2.5×10^4 and 4.5×10^4 V cm^{-1} by using $V_r = 2$ V and $0.5 \text{ V} \leqslant V_p \leqslant 2.3$ V. Because of the lower quiescent bias required to probe EHe211, we have used forward bias conditions to extend the electric field range. A sample annealed at 550 °C was used to measure the emission properties of EHe211.

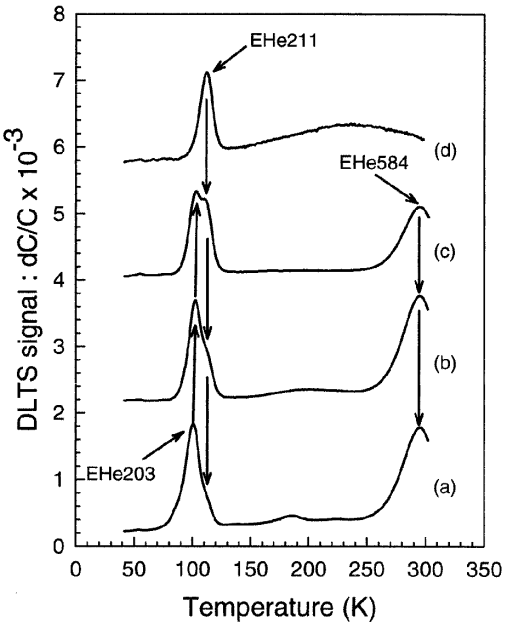

Figure 1. Curves a, b, c and d show the DLTS spectra of 1 keV He-ion-bombarded epitaxially grown n-Si (5×10^{15} cm^{-3}) after ZB isochronal annealing at 350, 450, 500 and 650 °C. The annealing was done under Ar flow for 20 min periods and in steps of 50 °C. EHe203 and EHe584 have a similar annealing behaviour. The high-temperature broad peak in curve d could be due to the degraded Schottky barrier diode or the presence of extended defects which introduced a continuous band of defects in the bandgap.

Free carrier compensation occurs in ion-beam-bombarded n-Si as a result of either the introduction of acceptor-type defects or dopant passivation in the form of dopant–defect pairs. This bombardment-induced lowering in dopant levels results in a corresponding decrease in the effective electric field experienced by deep traps. We have, therefore, computed the effective electric field in our samples using experimentally determined free carrier concentrations from variable-temperature capacitance–voltage (CV–T) measurement.

3. Results

3.1. Isochronal annealing behaviour

Figure 1 shows the DLTS spectra of 1 keV He-ion-bombarded n-Si after ZB isochronal annealing at 350, 450, 500 and 650 °C (curves a, b, c and d, respectively). It is evident from this figure that the annealing behaviours of EHe203 and EHe584 were similar. The high-temperature broad peak observed in figure 1, curve d, could be due to either the degraded metal–semiconductor interface at 650 °C or the presence of extended defects which introduced a continuous band of defects in the bandgap [26]. The variations in the peak DLTS intensities at a depth of 0.5 μm below the Pd–n-Si interface of EHe203 and EHe211 are illustrated in

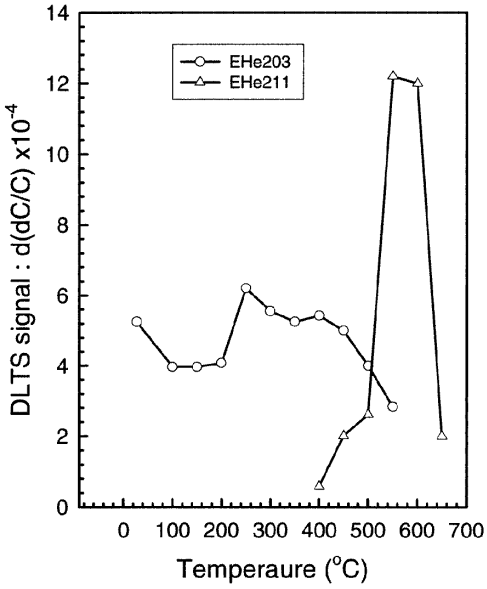

Figure 2. Variation in the peak DLTS intensities at a depth of 0.5 μm below the Pd–n-Si interface of EHe203 (open circles) and EHe211 (open triangles). The fading EHe203 signal peak above 550 °C was masked by the intense EHe211 peak and could not, therefore, be measured. It is clear that the removal of EHe203 was accompanied by the introduction of EHe211.

figure 2. The DLTS peak of EHe203 became weak above 550 °C and was masked by the dominant EHe211 signal peak. Figures 1 and 2 clearly demonstrated that the ZB isochronal annealing of EHe203 and EHe584 above 400 °C resulted in the simultaneous introduction of EHe211, which was thermally stable at 650 °C.

3.2. Dependence of emission rates on electric field

The emission rate of EHe584 showed virtually no electric field dependence. We observed a variation of 5% (within experimental error) in its value after changing the electric field from 3×10^4 to 9×10^4 V cm^{-1}. The variations in the emission rates of EHe203 and EHe211 as a function of applied electric field are shown in figures 3(a) and 3(b), respectively. The depth profiles of EHe203 and EHe211 (not shown) were determined using the method of Zohta and Watanabe [27]. Since the spatial distribution of EHe211 was shallower than that of EHe203, a smaller quiescent bias ($V_r = 2$ V compared with 5 V for EHe203) was used to study the electric field dependence of the emission property of EHe211. Figure 3(a) revealed that the emission rate of EHe203 was significantly enhanced by an electric field, while that of EHe211 showed a weak electric field dependence (figure 3(b)) over the electric field ranges covered in this study.

The low-field defect energy and apparent capture cross-section (E_t, σ_a) of the defects, commonly referred to as their DLTS 'signature', were extracted from the conventional DLTS Arrhenius plots [28] for the lowest electric fields. For

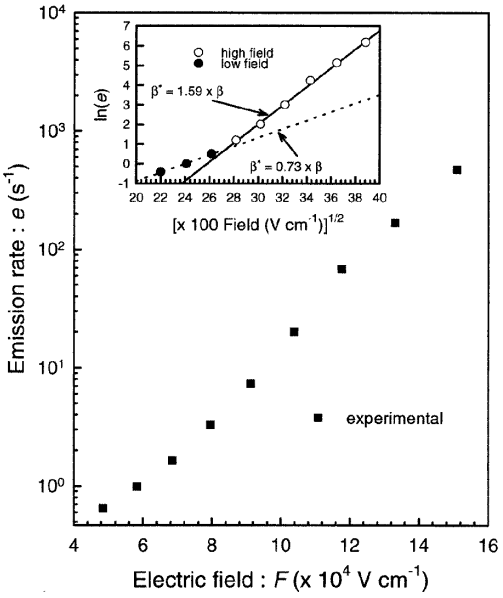

(a)

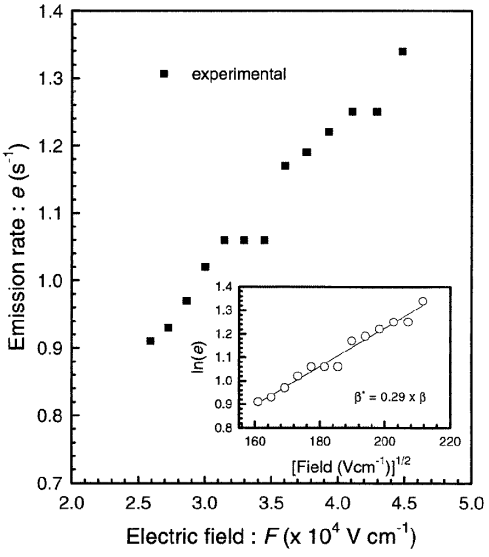

(b)

Figure 3. Variations in the emission rates of (a) EHe203 and (b) EHe211 as a function of externally applied electric field. The insets show linear plots of $\ln(e)$ versus $F^{1/2}$ for both defects, but the slopes did not yield the theoretical value of β for a singly charged defect. The emission rate data for EHe203 and EHe211 were measured at 85 and 100 K, respectively.

EHe203 and EHe211 the 'signatures' were 0.20 ± 0.03 eV, $(7.2 \pm 0.5) \times 10^{-16}$ cm^2 and 0.21 ± 0.03 eV, $(3.2 \times 0.5) \times 10^{-16}$ cm^2, respectively. The low-field 'signature' of EHe584 was 0.58 ± 0.03 eV and $(1.0 \pm 0.5) \times 10^{-15}$ cm^2. We have recently shown that the formation of EHe203

was independent of the presence of O, whereas EHe584 was introduced only in our O-containing samples. We have also proposed that the three electron traps investigated here were due to higher-order vacancy clusters [28–30]. The experimental data shown in figures 3(*a*) and 3(*b*) were simulated by employing the simple Poole–Frenkel coulombic, square and Gaussian defect potential models. The theoretical principles concerning the effects of an electric field on carrier emission from deep defect levels having potential wells of Coulomb, square and Gaussian forms have been described in [15] and will not be further discussed.

3.3. Coulombic potential well

According to the one-dimensional Poole–Frenkel formalism for a singly charged defect, a plot of $\ln[e(F)]$ versus $F^{1/2}$ should yield a straight line with slope β/kT [15, 17]. The plots of $\ln[e(F)]$ versus $F^{1/2}$ for EHe203 and EHe211 are depicted in the insets of figures 3(*a*) and 3(*b*), respectively. Although the experimental data could in both cases be closely fitted using linear regressions, the slopes of the linear fits did not yield the theoretical value of β for a singly charged defect. Figure 3(*a*) yielded experimental values β^* equal to 0.73β and 1.59β for the low- and high-field conditions, respectively, while figure 3(*b*) showed that a value of $\beta^* = 0.29\beta$ could be extracted. It followed that neither EHe203 nor EHe211 behaved according to the one-dimensional Poole–Frenkel formalism for a singly charged defect.

In order to simulate the expected field-dependent emission properties of EHe203 and EHe211 for one-dimensional Poole–Frenkel coulombic wells (figures 4 and 5, respectively), we have equated the zero-field emission rates ($e(0)$) of the traps to thermal emission rates (e(th)). The thermal emission rates, e(th), of EHe203 and EHe211 were calculated from their low-field 'signatures' using

$$e(\text{th}) = v_{th}\sigma_a N_C \exp(-E_t/kT) \qquad (1)$$

where v_{th} is the electron thermal velocity and N_C is the effective density of states in the conduction band. From curve a in figure 4 it is observed that the experimental data for EHe203 were a few orders of magnitude lower than the simulated data. In this case, the discrepancy between the experimental and simulated results could be reduced by using $\sigma_a \approx 10^{-18}$ cm^2 (curve b in figure 4), and changes in E_t did not have a significant effect (curve c in figure 4). Similarly, curves a, b and c of figure 5 further showed that the electric-field-enhanced emission rate from EHe211 could not be approximated by the one-dimensional Poole–Frenkel coulombic potential model. For any combination of E_t and σ_a, the increase in emission rate with increasing electric field was higher than the corresponding experimental increments.

A more comprehensive description of the electric-field-enhanced emission property from a singly charged particle (defect) can be described by the 3D coulombic well formalism [15, 18]. The field-assisted emission rates for 3D coulombic wells are illustrated by curves d and e in figures 4 and 5 for EHe203 and EHe211, respectively, Curve f in figure 4 corresponds to the simulation of the emission property for a double donor and is further discussed below. These curves showed that the electric-field-assisted emission

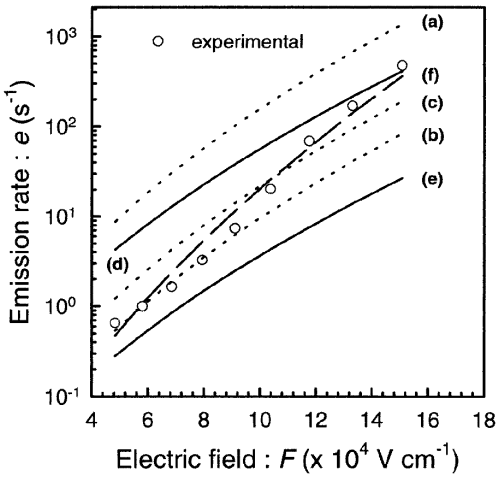

Figure 4. Experimental emission rate data (symbols) for EHe203 at a temperature of 85 K. Curves a–c (dotted lines) and d–f (full lines) are the modelled emission rates according to the Poole–Frenkel effect for one-dimensional and 3D coulombic potential wells, respectively. For the modelling we have used a low-field capture cross-section of 7.2×10^{-16} cm^2 (except for curve c) and the following values of E_t: curves a and c, $E_t = 0.20$ eV; curve b, $E_t = 0.22$ eV; curve d, $E_t = 0.19$ eV; curve e, $E_t = 0.21$ eV. Curve f is the emission rate data for a double donor for $E_t = 0.224$ eV. A value of $\sigma_a = 1 \times 10^{-16}$ cm^2 was used to model curve c. Curve c can be made to match curve b in the low-field region by using $\sigma_a = 5 \times 10^{-17}$ cm^2.

obtained for 3D coulombic wells were weaker than for the one-dimensional Poole–Frenkel effect, but nevertheless did not fit the experimental data. We have thus concluded that neither EHe203 nor EHe211 had pure coulombic wells associated with them.

3.4. Square and Gaussian wells

In contrast to the Coulombic well, a spherically symmetric square well potential (radius b) gives rise to a more rapid variation of emission rate with electric field [15, 18]. The depth of the square well was assigned by assuming that the measured thermal activation energy of the trapped electron (n-Si) was the ground-bound-state energy in the well [23]. A potential well which may be geometrically more realistic than the square well is the Gaussian well (depth of V_0 and a characteristic width α) [15, 24].

Curve b in figure 6 (dotted line) showed that a square well with $b = 57$ Å gave a reasonable fit to the experimental data for EHe203. The somewhat large value of b suggested that EHe203 was most probably not a point-like defect. The effect of varying the dimension of the square well is demonstrated by curves a and c. When fitting the Gaussian potential model to the experimental data of EHe203, values of 20 Å and 0.30 eV for α and V_0 ($E_t = 0.197$ eV), respectively (full line in figure 6) gave an identical fit to the square well model with $b = 57$ Å.

For EHe211 (figure 7), a value of $b = 40$ Å for a square well of depth 0.35 eV gave a reasonable fit to the experimental

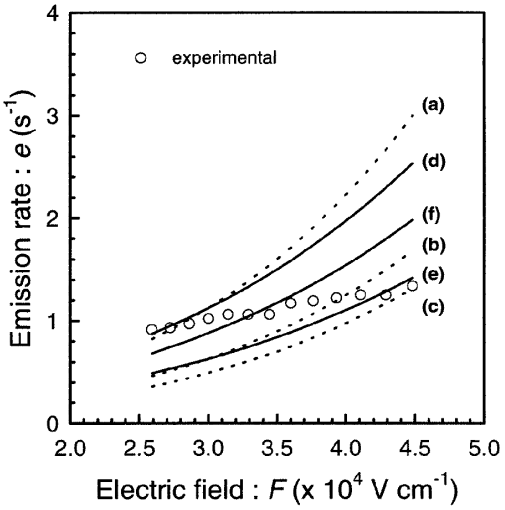

Figure 5. Experimental emission rate data (symbols) for EHe211 at a temperature of 100 K. Curves a–c (dotted lines) and d–f (full lines) are the modelled emission rates according to the Poole–Frenkel effect for one-dimensional and 3D coulombic potential wells, respectively. For the modelling we have used a low-field capture cross-section of 3.2×10^{-16} cm^2 (except for curves c and f) and the following values of E_t: curves a and c, $E_t = 0.23$ eV; curve b, $E_t = 0.235$ eV; curve d, $E_t = 0.215$ eV; curve e, $E_t = 0.22$ eV; curve (f), $E_t = 0.21$ eV. The effect of varying the capture cross-section is shown by curves c and f for which we have used $\sigma_a = 1.4 \times 10^{-16}$ cm^2.

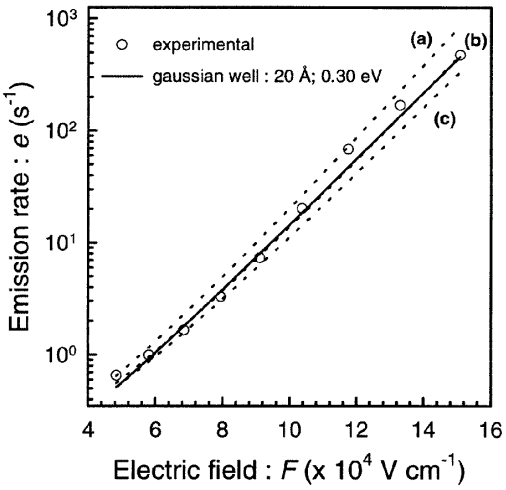

Figure 6. Modelled curves for a square well with three different dimensions for EHe203 (dotted lines). A value of $E_t = 0.185$ eV was used for curves a–c while the values of b were 60, 57 and 55 Å, respectively. The open circles represent the experimental data for EHe203 at 85 K. The curve drawn with a full line (overlaps with curve b) demonstrates that the experimental emission rate could also be simulated using the Gaussian potential model for $\alpha = 20$ Å, $V_0 = 0.30$ eV and $E_t = 0.197$ eV.

data (curve b). The size of this potential well suggested that EHe211 was also not a point-like defect. The influence of changing the radius of the square well is illustrated by curves a and c. Similarly to EHe203, the experimental data for EHe211 could also be quite well fitted using the Gaussian well model. In this case, the dimensions of the Gaussian well were $\alpha = 12$ Å and $V_0 = 0.35$ eV ($E_t = 0.198$ eV), as shown by the full line in figure 7.

4. Discussion

The isochronal annealing behaviours of EHe203 and EHe584 were similar. Their concentrations as reflected by their peak DLTS intensities decreased after annealing above 400 °C. In this temperature range, the introduction of a secondary defect EHe211 was observed, and we have concluded that it was introduced, at least partially, at the expense of EHe203 and EHe584. This conclusion could be further supported by our isochronal annealing studies of 5.4 MeV α-particle- and Si-implanted epitaxially grown n-Si [28–30]. In those studies we had proposed that EHe203 was a vacancy cluster larger than the divacancy (V_x, $x > 2$) and EHe584 was a complex vacancy cluster involving O atoms (V_yO_z, $y > 2$). The annealing behaviour of EHe211 together with its high-temperature stability prompted us to believe that it was most probably a vacancy cluster larger than those responsible for EHe203 and EHe584. Annealing above 400 °C would cause the dissociation of EHe203 and EHe584 into smaller vacancy aggregates which would then diffuse and recombine to form

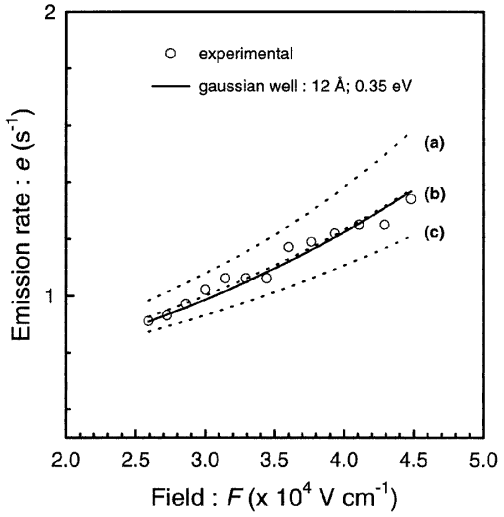

Figure 7. Modelled curves for a square well with three different dimensions for EHe211 (dotted lines). A value of $E_t = 0.197$ eV and $\sigma_a = 3.2 \times 10^{-16}$ cm^2 was used for curves a–c while the values of b were 45, 40 and 35 Å, respectively. The open circles represent the experimental emission rate for EHe211 at 100 K. The curve drawn as a full line (overlaps with curve b) demonstrates that the experimental emission rate could also be simulated using the Gaussian potential model for $\alpha = 12$ Å, $V_0 = 0.35$ eV and $E_t = 0.198$ eV.

the more thermally stable EHe211. It was recently shown that the reaction $V_{n-1} + V \rightarrow V_n$ was exothermic at least up

to $n = 7$ and that, except for the ring hexavacancy (V_6), V_n had several deep levels in the bandgap [10, 31].

The emission rate of EHe584 remained constant for electric fields in the range 3×10^4–9×10^4 V cm^{-1}. On the other hand, EHe203 showed significant electric-field-enhanced emission, whereby increasing the field threefold increased its emission rate by approximately 3 orders of magnitude. The emission rate of EHe211 was weakly field dependent between 2.5×10^4 and 4.5×10^4 V cm^{-1}.

The models that were explored to explain the emission enhancement of EHe203 and EHe211 were based on the Poole–Frenkel effect. Phonon-assisted tunnelling is characterized by the onset of a field-enhanced emission above a critical electric field (F_c). Since our experimental data did not show such a feature, it was clear that they could not be explained by pure phonon-assisted tunnelling.

The Poole–Frenkel effect has been widely used in the past to determine unambiguously whether a defect was of donor or acceptor type. It has, however, been demonstrated by Buchwald and Johnson [31] that short-range perturbations to the long-range coulombic tail, such as an energy barrier to carrier capture, could dramatically decrease the effect of externally applied electric fields on coulombic centres. Therefore, a null effect for the Poole–Frenkel effect did not unambiguously determine the defect type. In this study, because the emission property of EHe584 was electric field independent, and did not follow the Poole–Frenkel formalism, this defect was proposed to be acceptor type.

The potentials associated with EHe203 and EHe211 could not be explained using the coulombic potential model for a singly charged well (figure 3). Figures 4 and 5 revealed that large discrepancies (more pronounced for a one-dimensional well) existed between our experimental and simulated results when using the coulombic potential model. It is pointed out to the reader that the experimental value β^* can be used as an indication of the charge state of a defect. For example, a value of $\beta^* = \sqrt{2}\beta$ meant that the defect being investigated was a double donor (n-type semiconductor) [33]. Curve f in figure 4 revealed that EHe203 showed a field-enhanced emission property which was quite adequately described by the 3D Poole–Frenkel formalism for a double donor using $E_t = 0.224$ eV.

The potential wells induced by EHe203 and EHe211 were reasonably well explained using the square potential well formalism (figures 6 and 7, respectively). The radii of these wells ($b = 57$ Å for EHe203 and $b = 40$ Å for EHe211) revealed that the two defects had medium- to long-range potentials associated with them. Since the range of potentials for point-like defects usually extends only a few atomic spacings ($b < 10$ Å) [23], the experimental fit using the square potential well was in good agreement with our previous proposition that EHe203 and EHe211 were complex vacancy clusters [28–30]. Based on the above discussion, it can obviously be argued that the dimensions of the potential well associated with EHe211 ought to be larger than those of EHe203. We point out that the square well formalism does not account for defect charge states larger than unity [18]. Hence, we have speculated that the larger potential range of EHe203 was due to its higher charge state compared to EHe211.

The Gaussian potential well model also fitted the experimental data (figures 6 and 7) quite closely. However, the wells had small characteristic widths ($\alpha = 20$ Å and 12 Å) and depths $V_0 > E_t$ ($V_0 = 0.30$ eV and 0.35 eV) had to be used for modelling the field-assisted emission data. On the one hand, it might be tempting to conclude that these characteristic widths should correspond to those associated with point-like defect potential wells, which would be contradictory to the above explanations. On the other hand, it can be argued that, although the wells had small characteristics widths, they also had relatively larger depths V_0 (i.e. the electrons were not in the ground-bound-state of the Gaussian wells). One is, therefore, cautioned that since the Gaussian potential well has two moments (α, V_0) compared with one for the square potential well (b), a correlation between the dimensions of the Gaussian wells and the proposed physical structure of EHe203 and EHe211 was not straightforward. Furthermore, figures 6 and 7 revealed that, if the electrons were assumed to be in the ground-bound-state of the Gaussian potential wells ($E_t = V_0$), then the values of E_t required to model our experimental results adequately would have been larger than the measured low-field thermal activation energies of EHe203 and EHe584. However, similarly to what was observed using the square well model, our simulations showed that the width of the Gaussian potential well associated with EHe211 was smaller than that of EHe203.

5. Conclusions

In this paper we presented results concerning the isochronal annealing behaviour and electric-field-enhanced emission properties of three electron traps (EHe203, EHe584 and EHe211) introduced in 1 keV He-ion-bombarded epitaxially grown n-Si. EHe203 and EHe584 were found to behave similarly under ZB annealing. The removal of EHe203 and EHe584 by annealing above 400 °C was accompanied by the introduction of the secondary defect EHe211, which was thermally stable at 650 °C. The emission rate of EHe584 was independent of electric field and we have proposed that the defect was acceptor type. The emission rate of EHe203 was, on the other hand, significantly enhanced by an electric field. It showed an emission enhancement of approximately 3 orders of magnitude for a corresponding threefold increase in electric field. EHe211 showed only a weak field dependence. The potential wells associated with EHe203 and EHe211 could not be explained using the Poole–Frenkel coulombic potential model for a singly charged defect. However, the emission property of EHe203 followed that of a double-donor coulombic centre reasonably well.

The field-assisted emissions of EHe203 and EHe584 were described using the square well model with $b = 57$ Å and 40 Å, respectively. The size of the wells showed that the two defects had medium- to long-range potentials typical of non-point-like defects. This confirmed our previous propositions that EHe203 and EHe211 were complex vacancy clusters. The shorter potential range of EHe211 has been attributed to its smaller charge state. Gaussian potential wells with small characteristic widths but large depths ($V_0 > E_t$) could also be used to explain the emission properties of the two defects.

References

[1] Ashok S, Krautle H and Beneking H 1984 *Appl. Phys. Lett.* **45** 431
[2] Grussel E, Berg S and Andersson L P 1980 *J. Electrochem. Soc.* **127** 1573
[3] Weber J 1991 *Physica* B **170** 201
[4] Burger N, Thonke K, Sauer R and Pensl G 1984 *Phys. Rev. Lett.* **52** 1645
[5] Davis R J, Habermeier H-U and Weber J 1985 *Appl. Phys. Lett.* **47** 1295
[6] Sawyer W D, Weber J, Nabert G, Schmalzlin J and Habermeier H-U 1990 *J. Appl. Phys.* **68** 6179
[7] Kirkpatrick C G, Noonan J R and Streetman B G 1976 *Radiat. Eff.* **30** 97
[8] Minaev N S, Mudryi A V and Tkachev V D 1981 *Phys. Status Solidi* b **108** K89
[9] Estreicher S K, Weber J, Derecskei-Kovacs A and Marynick D S 1997 *Phys. Rev.* B **55** 5037
[10] Estreicher S K, Hastings J L and Fedders P A 1997 *Appl. Phys. Lett.* **70** 432
[11] Lang D V 1974 *J. Appl. Phys.* **45** 3014
[12] Tasch A F Jr and Sah C T 1970 *Phys. Rev.* B **1** 800
[13] Bourgoin J and Lannoo M 1983 *Point Defects in Semiconductor II, Experimental Aspects* (New York: Springer) pp 191–202
[14] Wang K L and Li G P 1983 *Solid State Commun.* **47** 233
[15] Auret F D, Goodman S A and Meyer W E 1995 *Semicond. Sci. Technol.* **10** 1376
[16] Estreicher S K and Fedders P A 1997 *Mater. Sci. Forum* **258–263** 171
[17] Frenkel J 1938 *Phys. Rev.* **54** 647
[18] Hartke J L 1968 *J. Appl. Phys.* **39** 4871
[19] Henry C H and Lang D V 1977 *Phys. Rev.* B **15** 989
[20] Pons D and Makram-Ebeid S 1979 *J. Phys. (Paris)* **40** 1161
[21] Kimerling L C and Benton J L 1981 *Appl. Phys. Lett.* **39** 410
[22] Pensl G, Roos G, Holm C and Wagner P 1986 *Mater. Sci. Forum* **10–12** 911–16
[23] Walker J W and Sah C T 1973 *Phys. Rev.* B **8** 5597
[24] Zhu Q S, Hiramatsu K, Sawaki N, Akasaki I and Liu X N 1993 *J. Appl. Phys.* **73** 771
[25] Lefevre H and Schultz M 1977 *Appl. Phys.* **12** 45
[26] Schröter W, Kronewitz J, Gnauert U, Riedel F and Seibt M 1995 *Phys. Rev.* B **52** 13 726
[27] Zohta Y and Watanabe M O 1982 *J. Appl. Phys.* **53** 1809
[28] Auret F D, Deenapanray P N K, Goodman S A, Meyer W E and Myburg G 1998 *J. Appl. Phys.* **83** 5576
[29] Deenapanray P N K, Auret F D and Ridgway M C 1998 *J. Appl. Phys.* **53** 1809
[30] Deenapanray P N K, Auret F D, Ridgway M C, Goodman S A and Myburg G 1998 *Mater. Res. Soc. Symp. Proc.* to be published
[31] Hastings J L, Estreicher S K and Fedders P A 1997 *Mater. Sci. Forum* **258–263** 509
[32] Buchwald W R and Johnson N M 1988 *J. Appl. Phys.* **64** 958
[33] Buchwald W R, Gerardi G J, Poindexter E H, Johnson N M, Grimmeiss H G and Keeble D J 1989 *Phys. Rev.* B **40** 2940

8

DLTS observation of the transformation of bistable defects

8.1 Introduction

Most defects in semiconductors have, for a given charge state, a single fixed atomic configuration. Consequently, the deep levels due to these defects remain detectable under a wide range of experimental conditions, and their properties do not depend on the history of the sample. However, there are deep levels that are easily removed and re-introduced by relatively small changes in experimental conditions. An example of such conditions that may remove and re-introduce these defects is annealing under forward or reverse bias (i.e. in the presence or absence of electrons). This behaviour of defects suggests that these defects have more than one structural configuration in at least one charge state. Defects having two structural configurations are called configurationally bistable, while those with more than two structural configurations are referred to as being multistable.

From a technological point of view, these defects are important since their complex behaviour may lead to erratic behaviour of devices manufactured on material containing the defect, as illustrated by the Thermal Donors in Silicon (Chantre, 1989). From a scientific point of view, these defects allow the measurement of certain parameters (e.g. transformation activation energy) that can shed more light on the accuracy of theoretical models. In the long term, defect metastability may become interesting as an information storage technology.

The standard method used to detect defect bistability by means of DLTS, is to compare two DLTS temperature scanned spectra, recorded upwards in temperature, after cooling the sample under zero and reverse-bias conditions respectively. Any differences between these two spectra are probably due to defects changing their configurations due to the applied bias, before the sample was cooled down. See, for instance, Levinson (1985). However, during the recording of a spectrum, an LIA DLTS system continuously exposes the sample to filling pulses. Since these filling pulses also change the charge state of the defect, they may also transform the defect to another configuration. LIA DLTS is therefore not the ideal technique to characterise metastable defects.

However, in a digital DLTS system, it is possible to make “one shot” measurements, where only a single filling pulse is applied, therefore almost eliminating the danger of unintentionally transforming the defect. In this study, we used the digital DLTS system to characterise the electronic and metastable properties of an α-particle induced defect in epitaxially-grown boron-doped p-type silicon. A copy of two papers that followed from the research is included at the end of the chapter.

Originally, Mamor discovered and characterised the defect by means of an LIA DLTS system. However, due to the limitations of the LIA DLTS system, data could only be recorded over a limited range, and significant scatter and systematic errors were evident. The present author repeated the measurements and calculations with the digital DLTS system described in this work, provided the results in the publication, and wrote a significant portion of the paper (amongst others, all of the experimental section involving isothermal DLTS and the characterisation of the metastable properties of the defect, as well as most of the discussion of the metastable properties of the defect.)

8.1.1 Configurationally bistable defects

Configurationally bistable defects are defects in which at least one charge state has two possible atomic configurations that achieve a local minimum in the total energy of the defect. (The total energy of the defect is the sum of the electronic and the elastic energy.) The best way to describe configurational defect metastability is by making use of a configuration coordinate (CC) diagram. This diagram is a schematic graph of the total energy of the defect, drawn for every relevant charge state of the defect as a function of the configuration coordinate. The configuration coordinate represents the degree to which the atoms comprising the defect are in either of the two configurations.

For most monatomic defects (e.g. a substitutional dopant in Si), the position of the minimum energy on the CC-axis does not depend on the charge state of the defect. However, for some defects (e.g. the DX centre in AlGaAs) a change in charge state causes a significant lattice relaxation. The CC diagrams corresponding to a “normal” and a large lattice relaxation defect are shown in Figure 8.1(a) and (b) respectively.

It is clear from their CC diagrams that the defects (a) and (b) discussed in the previous paragraph both have a unique stable atomic arrangement for a given charge state. This does not have to be the case. Consider the CC diagrams shown in Figure 8.1(c) and (d). These defects have two different stable structural configurations in at least one charge state and are referred to as being *bistable*. In one charge state, the configuration with the higher energy is called the metastable configuration, while the other is

called the stable configuration. The two configurations are separated by a barrier. If the defect is in some way placed in the metastable configuration, it will in time decay to the stable configuration. This transformation is generally thermally activated.

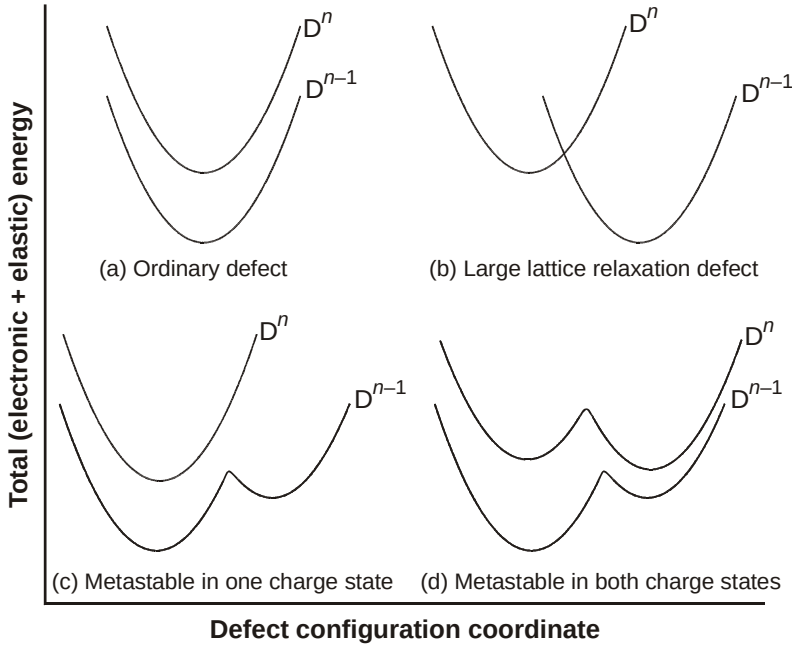

Figure 8.1 *Configuration coordinate diagrams for a number of different types of defects. (After Chantre, 1989).*

Some defects exhibiting metastable properties are the Thermal Donor in Si (Chantre, 1987), which seems to be bistable in only one charge state [as illustrated in Figure 8.1(c)], and Fe–Al and C–C pairs Greulich-Weber (1991) and Song (1988) in Si which seem to display bistability in all charge states [Figure 8.1(d)]. Multistable defects, having more than one metastable state, have also been observed in Si by Zhan (1993).

8.1.2 Charge state controlled metastability

In order for the phenomenon to be observable by means of DLTS, the stable configuration of a defect should change with charge state, and there should be a significant barrier for conversion between the charge states. Consider the CC shown in Figure 8.2. The defect has two possible structural configurations in both its neutral (0) and ionised states. However, in the neutral state, configuration A is stable, while in its ionised state, configuration B is energetically more favourable. In the following explanation it is assumed that the activation energy in both directions is such that at 300 K the transformation barriers $E_a(0)$ and $E_a(+)$ are easily surmounted, but at 100 K the defect is effectively "frozen" in its current state.

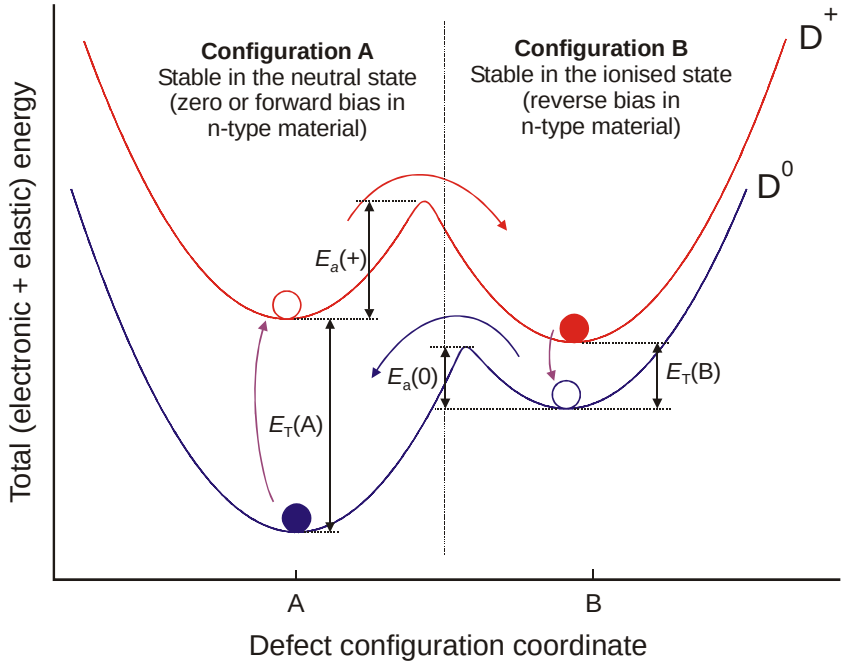

Figure 8.2 *Schematic diagram of a defect having two configurations, each configuration being stable in a different charge state. E.g. in the neutral state (lower curve) the defect is stable in configuration A, while in its ionised state, it is stable in configuration B (After Chantre, 1989).*

When the sample is at 300 K, the defect can be switched between configurations A and B by changing the charge state of the defect between its ionised and neutral states. In the area beneath a Schottky contact, this can be done by applying a suitable bias. For an n-type semiconductor, a forward bias would fill the defect level with an electron, leaving the defect in our example in its neutral state. Since configuration A is more stable in the neutral state, most of the defects will be in configuration A. Similarly a reverse bias would allow the defect level to emit an electron, thereby leaving the defect in its positively ionised state, which favours configuration B.

If the sample is cooled down to 100 K without changing the bias conditions, the stable configuration (either A or B, depending on the applied bias) will be frozen in. If, at this low temperature, the emission and capture rate of the defect is much higher than the transformation rate, the charge state of the defect can now be changed by changing applied bias, in principle without affecting the defect's configuration.

Once the defect has been transformed to the required configuration, it may be studied by means of DLTS. In the idealised case, one would expect to observe a DLTS peak associated with each of the configurations. However, in order to observe the DLTS peak, the associated defect has to remain stable while it is occupied by a carrier. There are a number of defects (including the one discussed by Mamor, 1998) where one of the transformation processes cannot be separated from carrier emission from the defect. In these cases, only one state can be observed by means of DLTS.

Although the most common technique to isolate and characterise charge-state controlled bistable defects is DLTS combined with bias-on/bias-off annealing cycles, other techniques to modulate the Fermi level (e.g. incident light or doping) are also used, see for instance Kaczor (1993)

8.1.3 Characterisation of metastable defects

In order to characterise a metastable defect completely, one would like to know the atomic structure in the various configurations as well as the physical mechanisms by means of which the defect transforms. As an intermediate step, the transformational properties of the defect can be summarised on a CC diagram. This implies determining the electronic energy levels in each configuration as well as the kinetics of the transformation.

Usually, the transformation occurs via first-order kinetics, with the transformation rate R thermally activated, according to

$$R = R_0 e^{-E_a / kT}$$

where E_a is the activation energy. The preexponential factor R_0 can be physically related to the attempt frequency of the process and can be used to deduce the physical mechanism leading to the temperature dependence. Some mechanisms identified so far are (Chantre, 1989):

i) elementary atomic jump ($R_0 \sim 10^{12}\ s^{-1}$)
ii) free-carrier capture by multiphonon emission ($R_0 \sim 10^{7}\ s^{-1}$)
iii) free-carrier emission ($R_0 \sim 10^{13}\ s^{-1}$)

8.1.4 Example: The C–C pair in Si

The physical structure of most metastable defects has not yet been identified. However, a well-researched example is the C–C pair in Si, reported by Song (1988), which consists of an interstitial carbon atom paired with a substitutional carbon atom. This defect can exist in two configurations called A and B, which differ only by a simple bond switching transformation, as shown in Figure 8.3.

Configuration A is stable for both the positively charged $(C_iC_s)^+$ and negatively charged $(C_iC_s)^-$ states, but for the neutral $(C_iC_s)^0$ state, Configuration B is stable. In their paper, Song et al. give a detailed discussion of how the properties of this defect were determined using DLTS, electron paramagnetic resonance (EPR) and optical detection of magnetic resonance (ODMR) results.

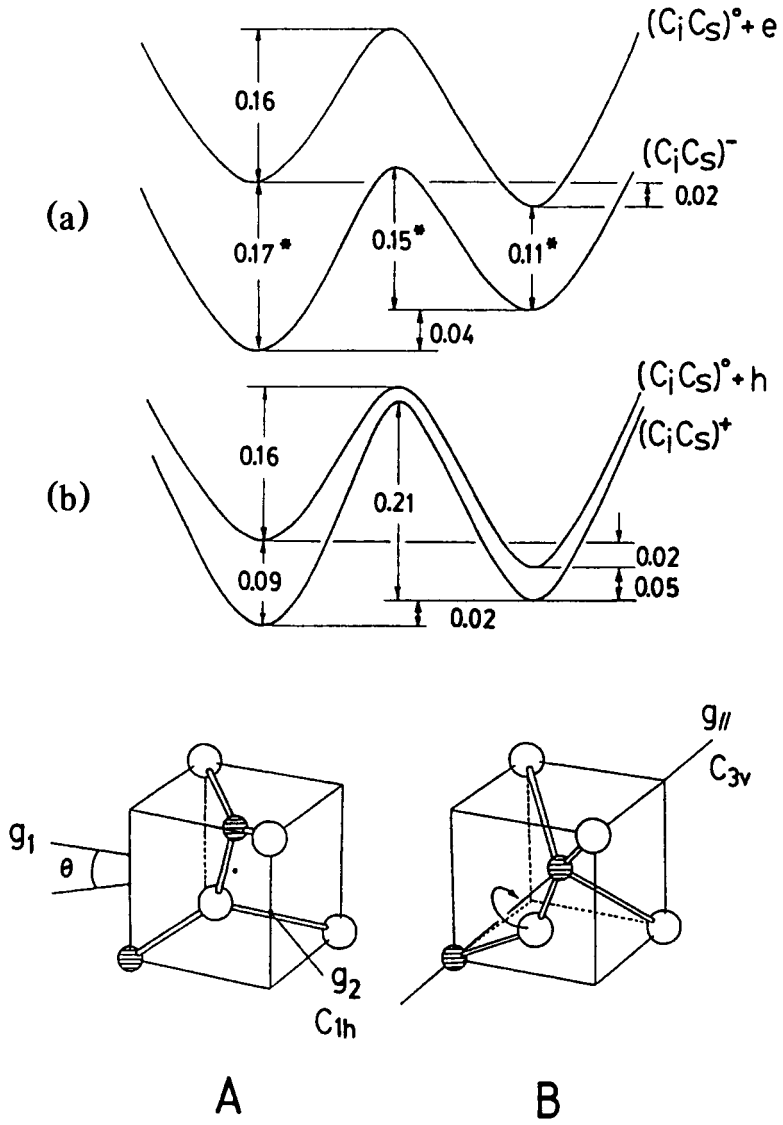

Figure 8.3 *C-C diagrams and sketches showing the metastable transformation of the C-C pair in Silicon. (Song, 1988)*

8.2 Experimental

8.2.1 Introduction

In this section, the results of an investigation into the metastable behaviour of an α-particle induced defect in epitaxially grown boron-doped p-type silicon are presented. The defect was originally detected and characterised by a conventional LIA-based DLTS system. During analysis of the data, it became clear that, due to the defect transforming during the repetitive filling pulse applied by the LIA-

based DLTS system, it was difficult to characterise the defect completely. The characterisation process was repeated, this time with the digital DLTS system, which yielded more reliable results, especially at higher temperatures where the defects would transform too fast for an LIA-based DLTS system to detect. Since single transients could be recorded and arbitrary long filling pulses could be applied, the digital system allowed for experimental conditions to be tailored to measure the transformation kinetics of the defect in a temperature range that was not accessible to the LIA-based system. These results from the digital system were used to augment the results obtained from the analogue system. See Figure 4 in Mamor (1998) and associated discussion.

8.2.2 Sample preparation

The sample was prepared according to the standard procedure mentioned in Chapter 5. After evaporation of the titanium Schottky contacts, the sample was irradiated through the contacts by 5.4 MeV α-particles from an americium 241 (Am-241) radionuclide to a fluence of 1×10^{12} cm^{-2}.

8.2.3 Determining the defects' DLTS signatures

The LIA DLTS spectrum of the sample is shown in Figure 8.4. Here it can be seen that defect Hα2 exhibits metastable properties – when the sample is cooled down under zero bias the Hα2 peak disappears (dotted line, State A), only to reappear when the sample is heated to 300 K and cooled down under reverse bias (solid line, State B). Because the Hα1 peak partially overlaps with the Hα2 peak, it is not possible to observe Hα2 in isolation without some processing. In order to isolate Hα2, the "zero-bias" scan (containing only Hα1) was subtracted from the "reverse-bias" scan (containing both Hα1 and Hα2, leaving a scan containing only Hα2, indicated by the dashed line in Figure 8.4.

The defects' DLTS signatures were determined in the usual way from Arrhenius plots in which $\ln(e/T^2)$ is plotted as a function of $1/T$ (see Section 2.2.1). The data for the Hα2 was obtained from the subtracted scans.

At higher temperatures, the Hα2 (state B) peak was quickly transformed by removal of the reverse bias. This also occurred during the relatively short DLTS filling pulse. It was found that, in the LIA-based DLTS system, where the sample was continuously exposed to the filling pulses, the cumulative effect of these filling pulses would soon remove the Hα2 completely. This process limited the maximum temperature at which the sample could be measured by an LIA-based system to approximately 220 K. On the other end of the scale, the lowest temperature at which the sample could be measured was limited to 200 K by the maximum period at which the LIA could still record a signal. Due to these two constraints, the temperature range over which data for an Arrhenius plot could be collected by the LIA-system was limited to a 20 K range between 200 and 220 K.

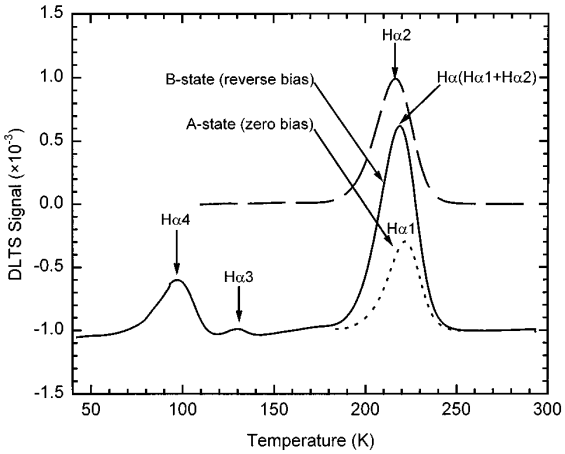

Figure 8.4 *LIA DLTS of the Hα2 peak measured after cool down under forward and reverse bias respectively, showing its metastable properties. (Mamor, 1998)*

Since the digital DLTS system only needed to record a single transient, only a single filling pulse was required, thereby minimising the transformation due to the DLTS filling pulse. Furthermore, the digital system could record much longer transients than the LIA-based system, so it was possible to measure at much lower temperatures as well. The results of these measurements are shown in Figure 8.5. For comparison, the values obtained from the LIA-based system are also shown. Although these points lie in the same vicinity as those obtained from the digital system, they show more scatter and, as discussed earlier, they cover a much narrower range.

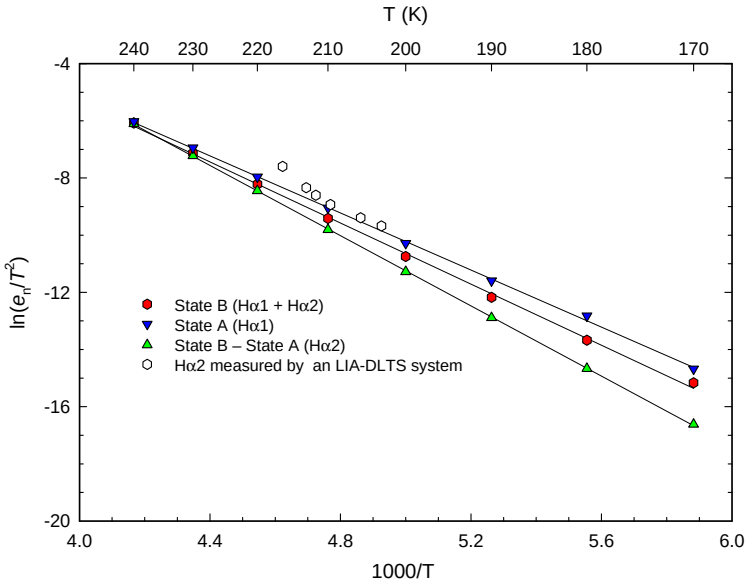

Figure 8.5 *Arrhenius plots of the Hα1, Hα2 and (Hα1 + Hα2) peaks as obtained by the digital DLTS system (filled symbols). The graph also shows the points determined by means of a conventional LIA-DLTS system (open circles).*

8.2.4 Determination of the transformation kinetics

In an LIA DLTS system, the standard procedure to measure the transformation rate of a metastable defect from state B to state A is to first transform the defect completely to state B. The peak height of state B is then measured by means of DLTS. Hereafter the sample is now repeatedly annealed for a specified period under conditions favouring state A, and the peak height due to the defects remaining in state B is measured after every annealing cycle. If the peak height is plotted as a function of total annealing time, one should obtain an exponential decay curve from which the decay constant can be determined.

By repeating this procedure at different temperatures, these decay constants can be used to determine the activation energy of the defect as described in Section 8.1.3.

Although the technique above seems quite straightforward, it relies on a number of assumptions:

1. Since it takes a finite time to heat the sample to the annealing temperature, the annealing time is never exact. This is particularly significant at higher temperatures when the transformation rate of the defect is high, and the time required to reach the annealing temperature is significant compared to the annealing time.

2. As described earlier, depending on the temperature at which the defect is measured, the defect may transform during the DLTS scan.

8.2.4.1 The transformation B → A

By means of the digital DLTS system, it was possible to measure the amplitude of the DLTS transient due to the defects at the annealing temperature. During this procedure, the sample was first annealed under reverse bias for a sufficient time to convert all the defects to state B. The transformation B → A was now allowed to occur by applying a single forward-bias transformation pulse to the defect. The pulse also filled the defect, and was therefore followed by a DLTS transient. This transient was not of interest, and was allowed to decay. Hereafter a second much shorter measuring pulse was applied and the resulting transient was recorded. By varying the length of the first pulse, and measuring the amplitude of the second transient, it was possible to determine the transformation rate of the defect.

It is interesting to note that the procedure described above leads to the rather counterintuitive result namely that, over the pulse length range of interest, longer filling pulses caused smaller DLTS transients.

8.2.4.2 The transformation A → B

By using the digital DLTS system, it was possible to observe the transformation of the defect more directly. It was observed from TSCAP measurements that the transformation A → B is associated with the emission of a hole. However, it was not clear whether the emission of the hole occurred as part of or directly after the transformation process. However, DLTS measurements show that hole emission from the B state occurred much faster than the transformation A → B; therefore, the emission of the hole (as

detected by DLTS) could be used as a reliable measure of the transformation. It was thus possible to observe this transformation directly by means of DLTS, as long as the DLTS filling pulse was long enough to convert a significant fraction of the defect to state A.

8.2.5 Discussion

The results of this research was published in the papers Mamor (1998) and Mamor (2000). The extended range allowed by the digital DLTS system is clearly shown in Figure 8.5, where the results obtained by the digital system are shown using solid symbols while the LIA-results are shown using open symbols. The results obtained by the digital system agreed well with those obtained by means of the analogue system. It is clear that the digital system extended the range and accuracy of the measurements significantly.

8.3 Publications

The results of this study on the Hα1 and Hα2 defects were published in the following publications. All digital DLTS measurements and associated calculations and discussion of the metastability were by the present author.

1. Mamor M, Auret FD, Goodman SA, Meyer WE and Myburg G 1998 Electronic and transformation properties of a metastable defect introduced in epitaxially grown boron-doped p-type Si by alpha particle irradiation *Appl. Phys. Lett.* **72** 3178

2. Mamor M, Willander M, Auret FD, Meyer WE and Sveinbjörnsson E 2000 Configurationally metastable defects in irradiated epitaxially grown boron-doped p-type Si *Phys. Rev. B* **63** 045201

APPLIED PHYSICS LETTERS VOLUME 72, NUMBER 24 15 JUNE 1998

Electronic and transformation properties of a metastable defect introduced in epitaxially grown boron-doped *p*-type Si by alpha particle irradiation

M. Mamor,[a] F. D. Auret, S. A. Goodman, W. E. Meyer, and G. Myburg
Physics Department, University of Pretoria, Pretoria 0002, South Africa

(Received 17 December 1997; accepted for publication 14 April 1998)

Titanium (Ti) Schottky barrier diodes on epitaxially grown boron-doped p-type Si films with a free carrier density of $6-8\times10^{16}$ cm^{-3} were irradiated with alpha particles at room temperature using an americium-241 (Am-241) radio nuclide. We report the electronic and transformation characteristics of an α-particle irradiation-induced defect $H\alpha2$ in epitaxially grown p-Si with metastable properties. The energy level and apparent capture cross section, as determined by deep-level transient spectroscopy, are $E_v+0.43$ eV and 1.4×10^{-15} cm^2, respectively. This defect can be removed and re-introduced using a conventional bias-on/off cooling technique. © *1998 American Institute of Physics.* [S0003-6951(98)03424-X]

Several investigations of the metastability of defects in as-grown Si as well as in as-grown GaAs and InP have been reported in the last few years by several workers.[1–4] The metastable configuration can normally be detected by deep-level transient spectroscopy (DLTS). Using the bias-on bias-off cooling technique and annealing cycles, these metastable defects are configurationally transformed to different energy states, which can usually be detected by DLTS. A significant number of metastable defects investigated in Si,[5] GaAs,[6] and InP,[4] were introduced by electron irradiation. In ultrafast quenched (laser irradiated) boron-doped Si a defect has been detected by capacitance spectroscopy (the C center after Chantre[7]) with metastable characteristics. This center was shown to exist in either of two configurations A or B, depending on its charge state. More recently, minority carrier injection combined with the bias-on bias-off cooling technique has led to the detection of a metastable defect in α-irradiated GaAs.[8] Hence, it is reasonable to expect that irradiation with other particle types would also introduce metastable defects in bulk grown Si as well as in epitaxially grown Si.

In this letter we demonstrate that, apart from a metastable electron irradiation induced defect in Si,[5] a prominent defect in α-irradiated epitaxially grown boron-doped Si is also metastable.

In this study, we used Schottky barrier diodes (SBDs) as the contact structure to the epitaxially grown Si. The Si samples studied were grown by chemical vapor deposition (CVD). Circular titanium contacts, 0.77 mm in diameter and 200 nm thick, were deposited by electron-beam evaporation onto p-Si at rate of 10 Å/s, through a metal contact mask. A metal shield was positioned to prevent stray electrons originating from filament from reaching the Si layers. The free carrier concentration (N_A-N_D) induced by boron doping of the epitaxial Si layers, as determined by capacitance–voltage $(C-V)$ measurements, was $6-8\times10^{16}$ cm^{-3}. An americium 241 (Am-241) radionuclide with an activity of 192 μCi cm^{-2} was used to irradiate the samples with 5.4 MeV α particles at a fluence rate of 7.1×10^6 cm^{-2} s^{-1}. As it is assumed that the measured capacitance transient varies exponentially with time, it is important that the densities of introduced deep levels are small compared to those of shallow levels. The trap density (N_T) should not be greater than 10% of the free carrier density (N_A-N_D) to ensure exponential transients.[9]

The α-particle induced defects in the Si epilayer were characterized by DLTS[10] using a lock-in amplifier (LIA) based system. The energy level (E_t) in the band gap and apparent capture cross section (σ_a) of defects were determined from Arrhenius plots of T^2/e vs $1/T$, where e is the emission rate at a temperature T.

The data for the Arrhenius plots were measured by means of an isothermal DLTS technique. The DLTS capacitance transient was measured by a Boonton 7200 capacitance meter and digitized by an HP 3458A multimeter. The digitized transient was analyzed with a ''simulated lock-in amplifier'' technique. This technique has the advantage that, depending on the signal quality, only a single transient is required to determine the emission rate of a defect at a given temperature. Furthermore, compared to an analogue lock-in amplifier, the digitally simulated lock-in amplifier allows for a wider range of emission rates to be observed, thus extending the temperature range over which the Arrhenius data could be measured. Unwanted transformation of the defect before the DLTS measurement was minimized by keeping the sample at the bias conditions under which it was annealed until the temperature for DLTS measurements was reached. The bias conditions for DLTS were applied only directly before the DLTS measurements were made. Since the isothermal DLTS technique described above requires only a single transient, the sample experienced only a single pulse that could transform the defect. In order to further minimize the risk of the defect being transformed by this single pulse, the rising edge of the DLTS filling pulse was shaped carefully to avoid overshoot, and the pulse was kept reasonably short (0.1 ms). By employing these techniques, it was possible to see both defect peaks at temperatures as high as 240 K. However, at 240 K the peak height of the subtracted spectrum was lower than in the other measurements,

[a]Electronic mail: mmamor@scientia.up.ac.za

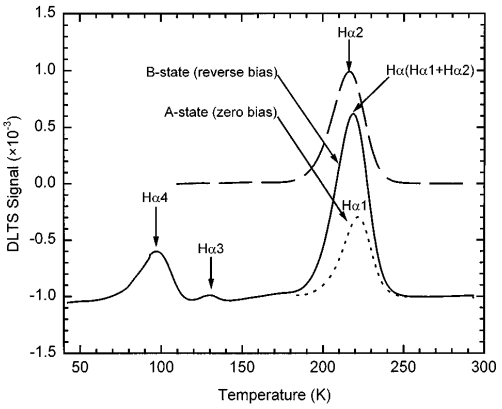

FIG. 1. DLTS spectra of p-type Si irradiated with alpha particle at a fluence of 9.3×10^{11} cm^{-2} (f=4.6 Hz, V_r=2 V, and V_p=1.8 V), illustrating the results of cooling with the bias-off (A state) and with applied reverse-bias (B state). The DLTS spectra derived from subtracting the two DLTS spectra (state A and B) is also shown.

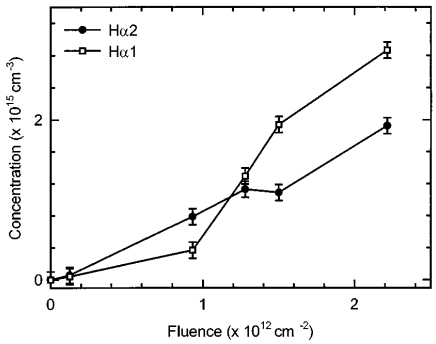

FIG. 2. Concentration of the $H\alpha1$ and $H\alpha2$ defects vs the fluence of irradiation.

indicating that some transformation did occur during the DLTS filling pulse.

No defects with concentrations above 2×10^{12} cm^{-3} could be detected by DLTS in the control (unirradiated) samples. Figure 1 shows three typical spectra after α-particle irradiation with the same fluence ($\approx9.3\times10^{11}$ cm^{-2}). The DLTS spectra that characterize the two different configurations of the defect are shown in this figure. The metastable defect (undetectable: A state) was not observed by DLTS after irradiation under normal bias conditions. The spectrum labeled state A is obtained if the specimen is cooled to the initial measurement temperature without an applied bias. The spectrum labeled state B is obtained if the specimen is cooled with a reverse-bias applied. The DLTS peak derived from the subtraction of the two DLTS spectra for the same fluence is also shown in Fig. 1. The two hole traps labeled $H\alpha1$ and $H\alpha2$ arise from two different defects. The transformation behavior of the $H\alpha2$ level is observed after zero-bias/reverse-bias cool down cycles: cooling down the sample at zero-bias causes the removal of the $H\alpha2$ signal. In contrast, cooling down at reverse-bias causes the re-introduction of defect $H\alpha2$.

In the A state, the $H\alpha1$ level has a hole emission activation energy of (0.53 ± 0.01 eV) and an apparent hole capture cross section of 1.6×10^{-13} cm^2. In the B state, peak $H\alpha$ contains contributions of $H\alpha1$ and $H\alpha2$ and has an activation energy of (0.46 ± 0.01) eV and a capture cross section of 5.3×10^{-15} cm^{-2}. An activation energy of (0.43 ± 0.01) eV and a capture cross section of 1.4×10^{-15} cm^2 were determined for $H\alpha2$. It appears that the defects labeled $H\alpha1$ and $H\alpha2$ detected in this study have the same signature as the defect detected in the same material after electron irradiation.[11]

The defect concentration profiles showed that the concentrations of $H\alpha1$ and $H\alpha2$ were very similar and constant in the region profiled (10–112 nm below the SBD interface) for each fluence investigated in this study. The introduction rates of individual defects $H\alpha1$ and $H\alpha2$ have been studied versus the fluence of α-particle irradiation in the range 1.2×10^{11}–2.2×10^{12} cm^{-2}, using the fixed-bias variable-pulse difference DLTS depth profiling in conjunction with the approach of Zohta *et al.*[12] Figure 2 shows that the concentration of $H\alpha1$ and $H\alpha2$ increases with an increase in the incident particle fluence (up to 2.2×10^{12} cm^{-3}). This suggests that these defects are either radiation-induced complexes related to impurities in the crystal of which the concentrations are higher than 2×10^{15} cm^{-3}, or a lattice defect complex independent of impurities. The DLTS signatures, the emission rates, and the introduction rates of these defects after alpha irradiation are summarized in Table I.

We assume the metastability observed in this study is caused by the reversible transformation of the states labeled A and B. In order to examine the transition $A\rightarrow B$, the sample was first cooled from 300 K to a temperature T under zero-bias; then it was annealed for a time t at reverse-bias, and finally cooled to 130 K. The changing magnitude of $H\alpha2$ was used to determine the changing population of this A state. A similar procedure was used to study the reverse transformation $B\rightarrow A$. The results obtained after this isochronal annealing are illustrated in Fig. 3. These results show that both transformations $A\rightarrow B$ and $B\rightarrow A$ occur in a single stage, but not in the same temperature range. The first transformation ($A\rightarrow B$) takes place at a higher temperature (240–265 K) than the second transformation ($B\rightarrow A$) (185–215 K). The anneal time t was then varied at a fixed temperature T (chosen around the transition temperatures) to explore the configurational transformation kinetics. The isothermal annealing kinetics were found to be first order. Arrhenius plots for both transitions are shown in Fig. 4 (open symbols). Since a hole is emitted during the transformation from $A\rightarrow B$ (see discussion later), it was possible to observe this

TABLE I. Electronic properties and the introduction rate of the prominent hole traps, $H\alpha1$ and $H\alpha2$, introduced during alpha particle irradiation of epitaxially grown p-Si.

Defect label	Int. rate (cm^{-1})	E_t (eV)	σ_a (cm^2)	e_n[a] at 220 K (s^{-1})
$H\alpha1$	1300	0.53	1.6×10^{-13}	10
$H\alpha2$	885	0.43	1.4×10^{-15}	17
$H\alpha(H\alpha1+H\alpha2)$	⋯	0.46	5.3×10^{-15}	13

[a]Emission rate at 220 k.

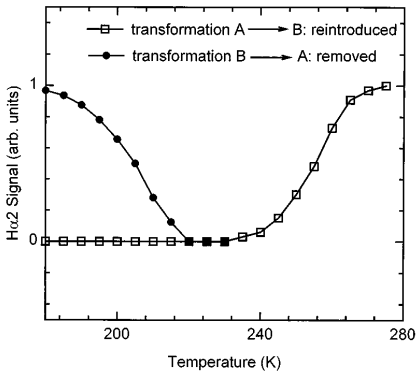

FIG. 3. Change in $H\alpha 2$ peak height as a function of temperature for both transformations $A \rightarrow B$ and $B \rightarrow A$. [isochronal (5 min) annealing]. All data points have been normalized to the maximum value of this signal.

transformation directly using DLTS. Using this technique, we measured the transformation rate from state A to state B directly. By varying the filling pulse width and measuring the DLTS peak height, we could determine the transformation rate from state B to state A as well. These measurements were performed in the temperature range 260–340 K, the results of which are indicated by solid symbols in Fig. 4. The observed reaction rates can be summarized by the following relations:

$$R = (4 \times 10^{12}\ \mathrm{s}^{-1}) \exp\left(-\frac{0.79}{kT}\right) \quad \text{for } A \rightarrow B, \tag{1}$$

$$R = (7 \times 10^{9}\ \mathrm{s}^{-1}) \exp\left(-\frac{0.52}{kT}\right) \quad \text{for } B \rightarrow A. \tag{2}$$

The rate constant above for the transformation $A \rightarrow B$ is between that expected for carrier emission and atomic jump (10^{12}–$10^{13}\ \mathrm{s}^{-1}$), but the rate constant for the transformation $B \rightarrow A$ is slightly larger than expected for carrier capture via multiphonon emission ($R_0 \approx 10^{7}\ \mathrm{s}^{-1}$), but smaller than expected for carrier emission ($R_0 \approx 10^{12}\ \mathrm{s}^{-1}$).[13]

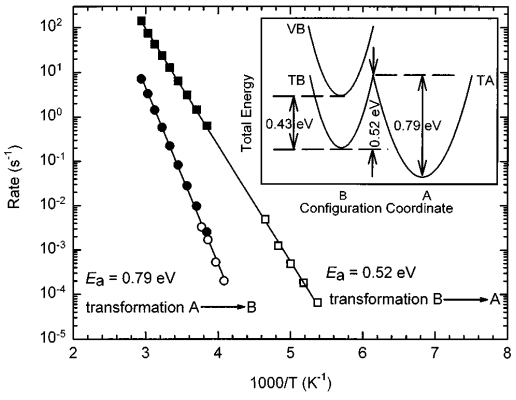

FIG. 4. Arrhenius plots of $A \rightarrow B$ and $B \rightarrow A$ transformation rates. The open and filled symbols correspond to data measured from annealing cycles and direct DLTS measurements, respectively. The configuration-coordinate (CC) diagram for the $H\alpha 2$ defect is shown in the inset.

A configuration-coordinate (CC) diagram of the $H\alpha 2$ defect, compatible with the above data, is shown in the inset of Fig. 4. The energy barrier for the transition from the A state to the B state is 0.79 eV and that for the reverse transformation 0.52 eV. This energy difference between the states explains the transformation temperatures as shown in Fig. 3. Because no DLTS peak associated with hole emission from state A was detected, the level associated with the empty defect in state A (VA) is not shown. However, because state B is stable under reverse bias, the total energy of the empty defect in state A should be the same or higher than that for state B. Consequently, the activation energy for hole emission from state A should be at least 0.70 eV.

In principle, there could be two different mechanisms for the transformation from state A to state B: the defect could either first emit a hole ($E_a = 0.79$ eV) and then transform via a fast process, or the defect could first transform with the hole still captured ($E_a = 0.79$ eV) and then emit the hole in a fast step. In both cases the rate of the transformation is determined by a step with an activation energy of 0.79 eV, and a hole is emitted during the transformation process. Since in state A the emission of a hole is either preceded or followed directly by a transformation to state B, it is not possible to observe a DLTS peak associated with state A.

In summary, we have reported the discovery of a new configurationally metastable defect, $H\alpha 2$, in boron-doped epitaxially grown p-type silicon following α-particle irradiation. The results presented here indicate that $H\alpha 2$ can be reversibly transformed using conventional bias-on/bias-off annealing temperature cycles. $H\alpha 2$ has an energy level at (0.43 ± 0.01) eV above the valence band. The physical nature of this defect is still unknown. To this end, the correlation between results obtained from different measurement techniques and using Si with different levels of dopant and other impurities could provide useful information about the physical nature of these defects and therefore more experiments are required.

The authors gratefully acknowledge the financial assistance of the Foundation for Research Development.

[1] A. Chantre, Mater. Res. Soc. Symp. Proc. **104**, 37 (1988).
[2] C. A. Londos, Phys. Rev. B **34**, 1310 (1986).
[3] W. R. Buchwald, G. J. Gerardi, E. H. Pointdexter, N. M. Johnson, H. G. Grimmeiss, and D. J. Keeble, Phys. Rev. B **40**, 2940 (1989).
[4] M. Levinson, M. Stavola, J. L. Benton, and L. C. Kimerling, Phys. Rev. B **28**, 5848 (1983).
[5] A. Chantre and L. C. Kimerling, Appl. Phys. Lett. **48**, 1000 (1986).
[6] T. I. Kol'chenko and V. M. Lomakoi, Semiconductors **28**, 501 (1994).
[7] A. Chantre, Phys. Rev. B **32**, 3687 (1985).
[8] F. D. Auret, R. M. Erasmus, S. A. Goodman, and W. E. Meyer, Phys. Rev. B **51**, 17521 (1995).
[9] W. E. Philips and J. R. Lowney, J. Appl. Phys. **54**, 2786 (1983).
[10] D. Lang, J. Appl. Phys. **45**, 3014 (1974).
[11] M. Mamor, F. D. Auret, S. A. Goodman, W. E. Meyer, and G. Myburg (unpublished).
[12] Y. Zohta and M. O. Watanabe, J. Appl. Phys. **53**, 1809 (1982).
[13] A. Chantre, Appl. Phys. A: Solids Surf. **48**, 3 (1989).

PHYSICAL REVIEW B, VOLUME 63, 045201

Configurationally metastable defects in irradiated epitaxially grown boron-doped *p*-type Si

M. Mamor* and M. Willander
Physics department, Physical Electronics and Photonics, (MC2), Chalmers University of Technology and Gothenburg University, S-412 96 Gothenburg, Sweden

F. D. Auret and W. E. Meyer
Physics Department, University of Pretoria, Pretoria 0002, South Africa

E. Sveinbjörnsson
Solid State Electronics Laboratory, Department of Microelectronics ED, Chalmers University of Technology S-412 96 Gothenburg, Sweden

(Received 25 April 2000; published 22 December 2000)

In this work, we investigate the metastability of the defect $H\alpha 2$ introduced in epitaxially grown boron-doped *p*-type Si by high energy (5.4 MeV) He-ion irradiation. Deep level transient spectroscopy (DLTS) and thermally stimulated capacitance (TSCAP) measurements were used to study the electronic properties of the defect in each configuration. The analyses indicate that this metastable defect can exist in either of two configurations (A or B) and can be reversibly transformed using conventional bias-on/bias-off annealing temperature cycles. The energy barriers for transition between these two configurations (A to B and B to A) are determined as 0.79 and 0.52 eV, respectively. In addition, we have compared the electronic properties of $H\alpha 2$ to those introduced during high-energy (12 MeV) electron irradiation and 250 keV proton irradiation. It is shown that defect $HE2$ introduced during electron irradiation of the same epitaxially grown *p*-Si and a defect $HP2$ introduced during 250 keV proton-irradiated boron doped float-zone (FZ) *p*-Si exhibit the same metastability as $H\alpha 2$ and provide further evidence that $H\alpha 2$ is hydrogen-related metastable defect.

DOI: 10.1103/PhysRevB.63.045201 PACS number(s): 71.55.−i, 61.80.Jh, 61.72.Ji, 61.72.Hh

I. INTRODUCTION

Most point defects in semiconductors are observed in only one configuration. However, it is possible that a defect may exist in more than one configuration, the stable configuration or a metastable configuration depending on the charge state of the defect. The alternate (metastable) configuration of a defect can be detected experimentally through its electronic properties. Under certain experimental conditions, usually bias-on/bias-off annealing cycles, the metastable defect is configurationally transformed to different energy states which can be detected by deep level transient spectroscopy (DLTS) or thermally stimulated capacitance (TSCAP) measurements. A thorough study of configurationally bistable defects in semiconductors has been reported by Levinson.[1]

Metastable defects are important in electronic materials because the degree to which they modify semiconductors may be reversibly altered, depending on the electric field and temperature conditions. The existence of configurationally metastable defects was first revealed by electron paramagnetic resonance (EPR) studies of the oxygen-vacancy pair in Si.[2] Later DLTS and TSCAP studies have also shown the presence of an unusual metastable defect in electron-irradiated *n*-type Si as well as in *n*-type GaAs and InP.[3–5] A defect with metastable characteristics has also been observed in boron-doped float-zone (FZ) *p*-Si single crystals, which is tentatively identified as the substitutional boron-vacancy complex.[6,7] A defect with metastable characteristics has also been detected in aluminum-doped and boron doped silicon substrates[8,9] following ultrafast quenching (laser irradiation). Recently, a defect with metastable characteristics has also been detected in boron-doped, Czochralski-grown, Si that was electron irradiated at 80 K and is assumed to be the oxygen related metastable defect.[10] Metastable defects, however, are not limited only to the above illustrations. The DX centers in $Al_xGa_{1-x}As$ and $GaAs_xP_{1-x}$ (Ref. 11) also show metastable properties. It has been reported that alpha-particle irradiation also introduces a metastable defect in GaAs.[12] Recently, using DLTS, we observed a new metastable defect $H\alpha 2$ introduced in boron-doped, epitaxially grown Si following room temperature alpha-particle irradiation.[13] This defect was found to exhibit reversible transformation between two configurations. Only in one configuration (which will be denoted as B), was the metastable defect directly observed by DLTS.

In this paper, we report the DLTS and TSCAP detection of configurationally metastable defects introduced in highly boron-doped *p*-Si epitaxially grown by chemical vapor deposition (CVD) following room temperature, He-ion irradiation. With new complementary investigation on this metastable defect using TSCAP, we report the observation of the metastable configuration ''A.'' As a result, we demonstrate here evidence that the defect $H\alpha 2$ can exist in either of two configurations designated A and B and exhibits two defect energy levels in the band gap. In order to investigate what kind of impurities might be involved in the configurationally metastable defect and the physical origin of this defect, we have compared the electronic properties of $H\alpha 2$ to those introduced during high energy (12 MeV) electron irradiation and 250 keV proton irradiation. As a result of its electronic and metastable properties, a defect $HE2$ introduced during electron irradiation of the same epitaxially grown *p*-Si and a

defect $HP2$ introduced during 250 keV proton-irradiated boron doped float-zone (FZ) p-Si exhibit the same metastability as $H\alpha 2$. In addition, we report on a study of the electronic properties of other defects introduced during He-ion irradiation of epitaxially grown p-Si. The He ions and electron irradiation-damage-induced defects in epitaxially grown Si are of additional interest due to the use of epitaxial materials for many devices fabrication.

In Sec. II we describe the experimental procedures involved. Section III describes the results obtained and comprises a discussion, after which some conclusions are presented in Sec. IV.

II. EXPERIMENTAL PROCEDURES

In our research we used Schottky barrier diodes (SBD's) as the diode contact structure to the boron-doped Si. Titanium SBD's on a p-type Si layer (doped to $6-8\times10^{16}\,\mathrm{cm}^{-3}$ with boron) grown epitaxially by chemical vapor deposition (CVD) on a p^+ Si(001) substrate, were irradiated with high energy (5.4 MeV) He ions at a fluence of $9.3\times10^{11}\,\mathrm{cm}^{-2}$, using an Americium radio-nuclide and 12 MeV electrons at a fluence of $1.6\times10^{12}\,\mathrm{cm}^{-2}$. In addition float-zone, boron-doped samples were irradiated with 12 MeV electrons and 250 keV protons to a total dose of $10^{13}\,\mathrm{cm}^{-2}$ and $7\times10^{12}\,\mathrm{cm}^{-2}$, respectively. DLTS, using a lock-in amplifier-based system, was used to study the defects. The bias and pulse sequence consisted of a reverse bias V_r on which pulses with amplitude V_p were superimposed. DLTS and TSCAP were also used to determine the electronic properties of the defects in each configuration, and the configurational transformation kinetics. The DLTS defect signatures (energy level in the band gap, E_t, and apparent capture cross section, σ_a) were calculated from the Arrhenius plots of $\ln(T^2/e)$ vs. $1/T$, where e is the emission rate at the DLTS peak temperature T. The data for the Arrhenius plots were also measured by means of an isothermal DLTS technique. Details on these experiments have been given elsewhere.[13]

III. RESULTS AND DISCUSSION

In Fig. 1 we present the DLTS spectra of Si irradiated with 5.4 MeV He ions [curves (a)]. For comparison, we also include spectra recorded from identical Si samples irradiated with 12 MeV electrons at a fluence of $1.6\times10^{12}\,\mathrm{cm}^{-2}$ [curves (b)]. The DLTS spectra for both samples were recorded under identical bias and pulse conditions: A filling pulse of amplitude $V_p=1.8$ V was superimposed onto a quiescent reverse bias of $V_r=2$ V. The spectra were taken after cooling the sample under zero bias (bias-off, configuration A) and after cooling with applied reverse bias (bias-on, configuration B) as shown in this figure. Curves (a) show the metastable behavior of the $H\alpha 2$ defect following He-ion irradiation. The transformation behavior of the $H\alpha 2$ level is observed after zero-bias/reverse-bias cool down cycles: cooling down the sample under zero-bias (configuration A: dotted line) causes the removal of the $H\alpha 2$ signal. Cooling down the sample under reverse-bias causes the reintroduction of defect $H\alpha 2$ (configuration B: solid line). The DLTS peak derived from the subtraction of the two DLTS spectra for the same fluence is also shown in this curve (dashed line). The two hole traps labeled $H\alpha 1$ and $H\alpha 2$, which are reported here, arise from two different defect levels.

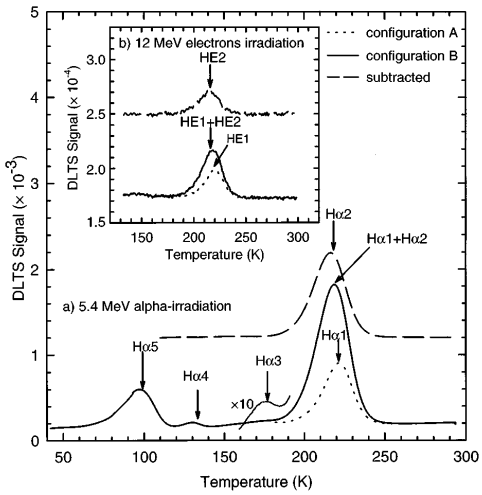

FIG. 1. DLTS spectra of p-type Si irradiated with 5.4 MeV He-ions at a fluence of $9.3\times10^{11}\,\mathrm{cm}^{-2}$, showing the result of cooling with applied zero-bias (configuration A: dotted line) and reverse-bias (configuration B: solid line). The DLTS spectrum derived from subtracting the two DLTS spectra (configuration A and B) is also shown (dashed line). The inset shows DLTS curve for 12 MeV electron irradiated p-type Si at a fluence of $1.6\times10^{12}\,\mathrm{cm}^{-2}$, showing the result of cooling with zero-bias (A) and applied reverse-bias (B).

The inset of Fig. 1 [curves (b)] shows DLTS spectra that characterize the two different configurations of the defect $HE2$ following 12 MeV electron irradiation. It appears that the defects labeled $H\alpha 1$ and $H\alpha 2$ have the same signature as the defects $HE1$ and $HE2$. Therefore, it is tempting to conclude that $H\alpha 1$ and $H\alpha 2$ are the same as $HE1$ and $HE2$, respectively.

The temperature dependence of the hole-emission rate was studied by means of an isothermal DLTS system. The results are shown in the Arrhenius plot [Fig. 2]. In configuration A, the $H\alpha 1$ level has a hole emission activation energy of 0.53 ± 0.01 eV and a hole capture cross section of $(1.6\pm0.5)\times10^{-13}\,\mathrm{cm}^2$. In configuration B, peak $H\alpha$ contains contributions of both $H\alpha 1$ and $H\alpha 2$, and appears to have an activation energy of 0.46 ± 0.01 eV and a capture cross section of $(5.3\pm0.5)\times10^{-15}\,\mathrm{cm}^2$. An activation energy of 0.43 ± 0.01 eV and a capture cross section of $(1.4\pm0.5)\times10^{-15}\,\mathrm{cm}^2$ were determined for $H\alpha 2$. An Arrhenius plot of the thermal emission rate of the defects $H\alpha 3$ and $H\alpha 5$ is shown in the inset of Fig. 2. The DLTS signature and peak temperature of these radiation-induced defects are summarized in Table I. The signatures of $H\alpha 3$ and $H\alpha 5$ were determined under low electric-field conditions (i.e., $V_r=0.3$ V, $V_p=0.3$ V). The activation energies of defects $H\alpha 3$ and $H\alpha 5$ are the same as the C_i-O_i (Ref. 14) and

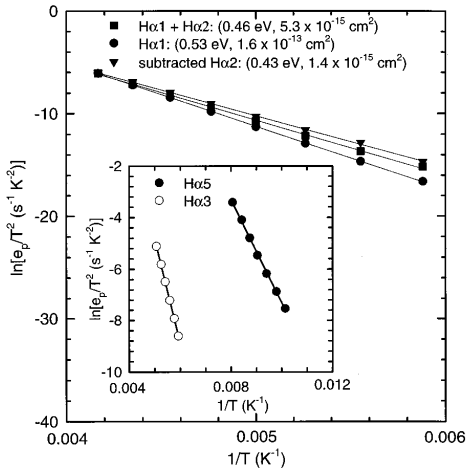

FIG. 2. Thermal emission rate data for the defect levels after cooling with bias-on (squares) and bias-off (circles). The thermal emission rate for the metastable defect is also shown (triangles). The thermal emission rates of defects $H\alpha3$ and $H\alpha5$ are shown in the inset.

divacancy[15] centers, respectively. A defect with a similar DLTS signature as $H\alpha1$ was detected;[16] however, the structure is as yet unresolved. The defect $H\alpha4$ was observed to anneal at room temperature after a few months with the appearance of a new defect $H^*\alpha4$ detected at $E_v+0.22$ eV.

Figure 3 shows DLTS scans of 250 keV proton-irradiated, FZ boron-doped, p-type Si and depicts the presence of the radiation-induced defects $HP1-HP5$. In this study we focus on the properties of defect $HP2$ that exhibits a metastable character. The solid line is a spectrum taken after cooling to 80 K with an applied reverse bias of 4 V applied to the sample. The temperature is then ramped up (about 5 K/min) and the spectrum is recorded. The dotted line shows a similar spectrum when the sample was cooled down to 80 K with zero bias applied to the sample. The only significant difference between the two spectra concerns the peak located at approximately 220 K, which is shifted depending on the bias during cooling. The peak has two contributions, hole emission from the state labeled B peaked at approximately 215 K (see broken line in Fig. 3) and hole emission from the state

TABLE I. Electronic properties of the prominent hole traps introduced during He-ion irradiation of epitaxially grown p-Si.

Defect label	E_t (eV)	σ_a (cm^2)	Peak temperature T_{peak}[a] (K)
$H\alpha1$	0.53	1.6×10^{-13}	223
$H\alpha2$	0.43	1.4×10^{-15}	215
$H\alpha(H\alpha1+H\alpha2)$	0.46	5.3×10^{-15}	220
$H\alpha3$	0.35	2.1×10^{-15}	174
$H\alpha5$	0.17	1.7×10^{-16}	102

[a]Peak temperature at a lock-in amplifier frequency of 4.6 Hz, i.e., a decay time constant of 92.3 ms.

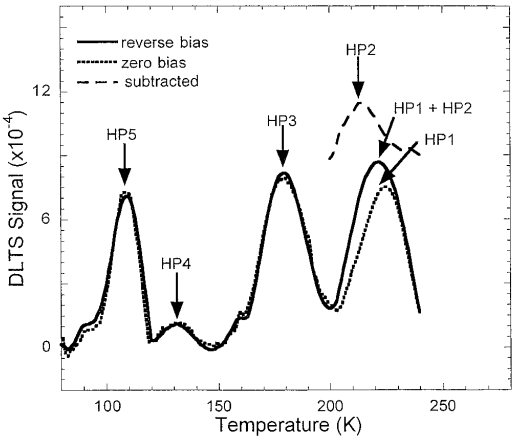

FIG. 3. DLTS spectra of a proton-irradiated, FZ, p-type silicon sample. Reverse bias$=2$ V, filling pulse$=1.8$ V and $e_p=10\,s^{-1}$. The broken line shows the signature of the metastable state B obtained by subtracting the dotted spectrum (zero bias during cooling) from the solid spectrum (reverse bias during cooling).

labeled A which is peaked at ≈225 K. The solid spectrum contains contributions from both states while the concentration of the B state is negligible after zero bias cooling (the dotted spectrum). The shift depends strongly upon the bias as well as the time needed to record the DLTS scan. For example if the ramp rate is reduced there is no significant difference between the two spectra and they become an intermediate between the two shown in Fig. 3. The reason for this is simply that the metastable transition takes place during the DLTS scan and a steady state between the population of the A state and the B state is reached before hole emission from the centers is recorded. The steady state ratio between the population of the states depends on the bias pulse applied during the DLTS measurement. For example, if the sample is kept at a reverse bias during the sweep and the filling pulse period is made as short as possible (10% duty cycle) the recorded spectrum is similar to the solid line in Fig. 3. If the situation is reversed and the filling pulse is on 90% of the time period, the recorded spectrum resembles the dotted line in Fig. 3. These bias-induced transformations of $HP2$ are charge state controlled and related to a reversible disappearance and reappearance of energy levels in the band gap.

The DLTS spectra were recorded in a somewhat unusual manner to enable detection of the metastable behavior. The transition rates, at these temperatures, from the metastable state B to state A are so high that if precautions are not taken the metastability is not observed at all.

The overall results agree very well with a study of the metastable defect $H\alpha2$ and $HE2$ in He-ion and electron-irradiated, epitaxially grown, boron-doped, p-type silicon, respectively. The hole emission rates of the metastable states are the same within experimental error and the bias dependence and transition rates between the metastable states are similar. Reference samples (FZ boron-doped p-type Si) from the same wafer without proton irradiation do not show any DLTS signatures of the metastable defect above the de-

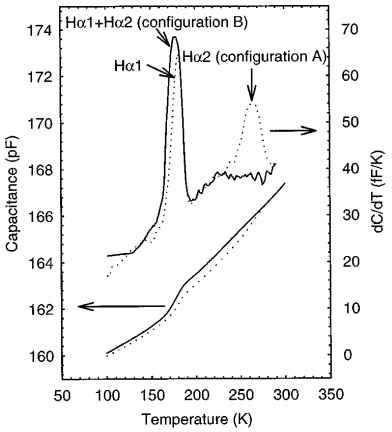

FIG. 4. TSCAP measurements of the sample shown in Fig. 1. The solid line was recorded after cooling under reverse bias while the dotted line was recorded after cooling under zero bias. In both cases the capacitance was measured at a bias of -1 V and the temperature was scanned at a rate of 3 K min^{-1}.

tection limit which is estimated to be at a concentration of 5×10^{11} cm^{-3}. The same applies to samples receiving 12 MeV electron irradiation using a fluence of 10^{13} cm^{-2}.

Concerning the differences in concentrations of the metastable defect after alpha irradiation as compared to electron and proton irradiation, we expect more damage with higher concentrations of point defects after high energy alpha irradiation as compared to low energy proton irradiation (only 250 keV) and electron irradiation. Since an alpha irradiation transfers more energy to the lattice than electron irradiation with the same kinetic energy, it is capable of forming disordered regions with a larger extent than the vacancy or interstitial defects typically observed after electron irradiation.

The remainder of this paper will concentrate on the metastability of $H\alpha2$ detected after He-ion irradiation. The metastability could also be observed by means of TSCAP measurements, as shown in Fig. 4. During these measurements, the sample was cooled under either zero or reverse bias in order to freeze in one of the metastable configurations of $H\alpha2$. After cooling to approximately 100 K, a short filling pulse was applied. Here, after a reverse bias of -1 V was applied, the temperature was increased at a constant rate of 3 K min^{-1} while the capacitance was recorded by means of an HP4192A Impedance Analyzer. Figure 4 shows the capacitance of the sample as a function of temperature, as well as its derivative dC/dT. The solid curve, which was recorded after cooling under a reverse bias of -1 V, shows hole emission from both $H\alpha1$ and $H\alpha2$ (in configuration B) at about 180 K as a rapid increase in the capacitance of the sample and a peak in the derivative curve. The dashed curve was recorded after cooling under zero bias conditions. Here the emission at 180 K is due to $H\alpha1$ only. $H\alpha2$, which has been transformed to configuration A, now emits carriers only once the temperature reaches 265 K, the same temperature at which it is transformed to configuration B. This indicates that the emission of holes from $H\alpha2$ in configuration A is closely linked to its transformation to configuration B.

The TSCAP results indicate that the transformation from configuration A to configuration B is closely associated with the emission of a hole. However, no hole emission could be observed from configuration A by means of conventional DLTS. The possible explanation for this behavior is that if the defect transforms before hole emission takes place, the hole would be emitted immediately by configuration B, because the transformation occurs at a temperature much higher than that at which configuration B starts to emit holes. This would imply that configuration A cannot be observed by means of DLTS because it transforms to state B before emitting a hole, i.e., the ionization energy of configuration A is too high for the defect to be observed by DLTS.

The transition from one configuration to the other was investigated in more detail by studying the thermally activated transformation kinetics between configurations A and B. We used the systematic method proposed by Levinson *et al.*[17,18] in their study of the metastable M center in InP. In order to examine the transition A→B, the sample was first cooled from 300 K to a temperature T at zero bias; then it was kept for a short time t at T under a fixed applied bias, and finally cooled rapidly to 130 K. The changes in the magnitude of $H\alpha2$ were used to determine the changing population of the defect in configuration A. In the same way, the reverse transition, B→A, was studied using reverse-bias cooling and zero-bias annealing. Isochronal (5 min) anneals were first performed to reveal the transformation temperature. The results obtained after this isochronal annealing (not shown here) revealed that both transitions A→B and B→A occur in only one stage, but not at the same temperature: The transformation A→B is observed at a higher temperature (240–265 K) than the transformation B→A (185–215 K). From our measurements, it seems that the transformation in both directions is complete. The reaction kinetics were then explored around the transformation temperatures by a series of isothermal anneals. The annealing reaction was found to be first order, as demonstrated in Fig. 5 for reaction A→B. Here, the normalized $H\alpha2$ peak height is plotted as a function of anneal time and temperature. The peak height of $H\alpha2$ as a function of time, $H\alpha2(t)$, was described by

$$H\alpha2(t)=H\alpha2(\infty)[1-\exp(-R_{A\to B}t)] \quad \text{A}\to\text{B}, \tag{1}$$

$$H\alpha2(t)=H\alpha2(\infty)[\exp(-R_{B\to A}t)] \quad \text{B}\to\text{A}, \tag{2}$$

where $H\alpha2(\infty)$ correspond to a peak height with $H\alpha2$ completely reintroduced.

We have also measured the transformation rate from configuration A to configuration B directly with DLTS, and from B to A by varying the filling pulse width and measuring the DLTS peak height.[13] The kinetics for the metastable defect transitions are consistent with the following relations:

$$R_{A\to B}=4\times10^{12}\exp[-(0.79\,\text{eV})/kT]\text{s}^{-1}, \tag{3}$$

$$R_{B\to A}=7\times10^{9}\exp[-(0.52\,\text{eV})/kT]\text{s}^{-1}. \tag{4}$$

Although DLTS does not provide information about the

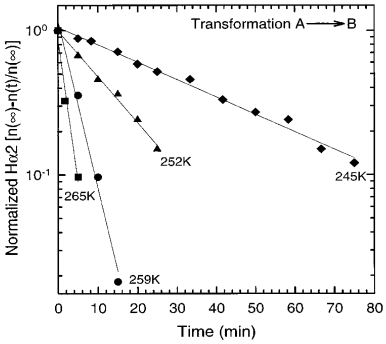

FIG. 5. Isothermal annealing kinetics for reaction A→B. For each point, the sample was cooled from 300 K to the indicated temperature with zero-bias, annealed at reverse-bias for the indicated time, and DLTS peak $H\alpha 2$ was monitored.

physical nature of defects, we nevertheless have some indications as to what $H\alpha 2$ may consist of. First, $H\alpha 2$ and $HE2$ metastable defects have up to now been reported only in high-energy He-ion and electron-irradiated, boron-doped p-Si that was epitaxially grown by CVD and not in FZ, boron-doped, p-type Si irradiated at the same condition. Second, the same metastable defect $HP2$ is also observed in float-zone, boron-doped, p-Si following proton irradiation. In view of these facts we suggest that the metastable defect $H\alpha 2$ is a hydrogen-related metastable defect due to the high concentration of hydrogen in our samples prepared by CVD and may consist of hydrogen linked to a lattice defect that was produced by the high energy bombardment.

IV. CONCLUSION

In summary, the results presented here demonstrate that one of the defects introduced in epitaxially grown, boron-doped, p-type silicon by high energy He-ion and high-energy electron irradiation, exhibits charge-state controlled metastability and can be reversibly transformed using conventional bias-on/bias-off temperature cycles. This metastable defect can exist in either of two configurations (A or B). In configuration B, $H\alpha 2$ has an activation energy E_t of 0.43 ± 0.01 eV and an apparent capture cross section σ_a of $(1.4\pm0.5)\times10^{-15}\,\mathrm{cm}^2$.

The physical nature of these defects can presently at best be speculated. However, in our previous study, we have observed that the defect concentration of $H\alpha 2$ increased linearly (up to $2\times10^{15}\,\mathrm{cm}^{-3}$) with increasing incident particle fluence, and no saturation effect has been seen for a fluence up to $2.2\times10^{12}\,\mathrm{cm}^{-3}$. The defect is either a radiation-induced complex related to impurities in the crystal of which the concentrations are higher than $2\times10^{15}\,\mathrm{cm}^{-3}$, or a lattice defect complex independent of impurities. Since the same metastable defect was produced by high-energy electron bombardment, it is likely to involve a lattice defect. The involvement of a lattice defect is also suggested by the nondetection of this metastable defect in similar materials irradiated with low-energy ions (<5 keV) created by the electron beam or Ar-ion bombardment. We should also notice that these metastable defects $H\alpha 2$ and $HE2$ were not observed in either He-ion or electron-irradiated, FZ boron-doped p-Si, and are present only in high-energy-particle-irradiated boron-doped, p-Si, that was epitaxially grown by CVD or in proton-irradiated, FZ boron-doped, p-Si. The overall results suggest that this defect $H\alpha 2$ may be either an interstitial complex, or a vacancy complexed with hydrogen.

ACKNOWLEDGMENTS

The authors thank Dr. A. Hallen, at the Royal Institute of Technology, Stockholm, Sweden for performing proton irradiation of the samples.

*Author to whom correspondence should be addressed. Present address: Institut für Physikalische Elektronik (IPE), Universität Stuttgart, Pfaffenwaldring 47, D-70569 Stuttgart, Germany; Electronic mail: Mohammed.Mamor@ipe.uni-stuttgart.de

[1] M. Levinson, J. Appl. Phys. **58**, 2628 (1985).
[2] G. D. Watkins, in *Lattice Defects and Radiation Effects in Semiconductors*, edited by F. A. Huntley (Institute of Physics, London, 1975), p. 1.
[3] O. O. Awadelkarim and B. Monemar, Phys. Rev. B **38**, 10 116 (1988).
[4] T. I. Kol'chenko and V. M. Lomakoi, Semiconductors **28**, 501 (1994).
[5] M. Stavola, M. Levinson, J. L. Benton, and L. C. Kimerling, Phys. Rev. B **30**, 832 (1984).
[6] C. A. Londos, Phys. Rev. B **34**, 1310 (1986).
[7] S. K. Bains and P. C. Banbury, J. Phys. C **18**, L109 (1985).
[8] A. Chantre and D. Bois, Phys. Rev. B **31**, 7979 (1985).
[9] A. Chantre, Phys. Rev. B **32**, 3687 (1985).
[10] C. A. Londos, Phys. Status Solidi A **133**, 429 (1992).
[11] D. V. Lang, in *Deep Centers in Semiconductors*, edited by S. T. Pantelides (Gordon and Breach, New York, 1986), Chap. 7, p. 489.
[12] F. D. Auret, R. M. Erasmus, S. A. Goodman, and W. E. Meyer, Phys. Rev. B **51**, 17 521 (1995).
[13] M. Mamor, F. D. Auret, S. A. Goodman, and W. E. Meyer, Appl. Phys. Lett. **72**, 3078 (1998).
[14] O. O. Awadelkarim, T. Gu, P. I. Mikulan, R. A. Ditizio, S. J. Fonash, K. A. Reinhardt, and Y. D. Chan, Appl. Phys. Lett. **62**, 958 (1993).
[15] B. J. Baliga and A. O. Evwaraye, J. Electrochem. Soc. **130**, 1916 (1983).
[16] P. K. Giri, S. Dhar, V. N. Kulkarni, and Y. N. Mohapatra, J. Appl. Phys. **81**, 260 (1997).
[17] J. L. Benton and M. Levinson, in *Defects in Semiconductors II*, edited by S. Mahajan and J. W. Corbett (North-Holland, New York, 1983), p. 95.
[18] M. Levinson, M. Stavola, J. L. Benton, and L. C. Kimerling, Phys. Rev. B **28**, 5848 (1983).

9

Negative-U defects in n-GaN

9.1 Introduction

A negative-U defect is a defect that can trap two electrons (or holes), with the second bound more strongly than the first. In semiconductors, negative-U ordering of defect levels leads to interesting metastability phenomena.

9.1.1 What is U?

Consider a hypothetical defect that can exist in three charge states: D^+, D^0 and D^-. I.e. if the defect is initially in the fully ionised D^+ state, it can capture two electrons. The first electron is captured according to $D^+ + e^- \rightarrow D^0$, and the second electron according to $D^0 + e^- \rightarrow D^-$. The first electron capture corresponds to a *donor* level, which is positive when it is above the Fermi level and neutral when it is below the Fermi level. Similarly, the second level corresponds to an *acceptor* level.

These two defect levels can be indicated on a band diagram as shown in Figure 9.1. Here the energy difference between the conduction band edge and the donor level is the binding energy of the first electron and the energy difference between the conduction band edge and the acceptor level is the binding energy of the second electron. Due to the Coulomb interaction between the electrons, one would expect the second electron to be more weakly bound than the first electron, and therefore the acceptor level is expected to lie above the donor level. The Coulomb interaction energy that is responsible for this phenomenon is frequently referred to as the Hubbard "correlation energy", after Hubbard (1963) who introduced it in his treatment of conductivity in narrow band semiconductors.

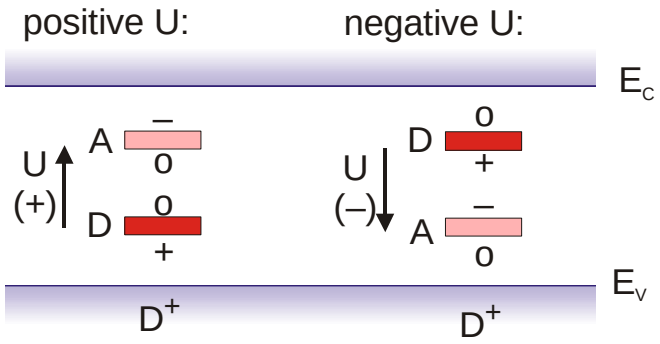

Figure 9.1 *A schematic energy-level diagram showing the behaviour of a defect D, having three charge states* D^-, D^0 *and* D^+.

Since the Coulomb interaction between two electrons is repulsive, it is quite reasonable to expect that *U* should always be positive. This is the case for most defects in semiconductors, however, some defects have been observed that behave as though the defect levels are inverted from their usual order, i.e. having a negative *U*. This implies that the second electron is *more tightly bound* than the first electron, as though there were an attractive potential between the electrons.

Negative-U behaviour is seen in a variety of physical and chemical systems ranging from disproportionation in electrochemical systems to defects in solids. An overview of a number of such systems including point defects as well as experimental evidence for these is given by Watkins (1984).

9.1.2 Mechanisms leading to negative-U behaviour

Some negative-U like properties of chalcogenide glasses were initially explained by Anderson (1975) using a model where, in addition to the restoring force the atoms exert on each other, the energy level of a state depends linearly on the displacement *x* between the two atoms. This model was expanded by Street (1975) and applied to point defects.

In the Anderson model, the potential energy of an atom is written in the form

$$V = -\lambda x(n_\uparrow + n_\downarrow) + \tfrac{1}{2}cx^2 , \tag{9.1}$$

where $n_\uparrow$ and $n_\downarrow$ are the occupancies (0 or 1) of the spin-up and spin-down bond orbitals. By setting $\partial V / \partial x = 0$ and substituting back in (9.1), it follows that, after relaxation, the potential energy is lowered by $-\lambda^2 / 2c$ for single occupancy and $-2\lambda^2 / c$ for double occupancy. The net effective correlation energy, defined by the energy difference between two singly occupied bonds and the disproportionated state (one empty and one doubly occupied bond) becomes

$$U_{\text{eff}} = U - \lambda^2 / c . \tag{9.2}$$

where *U* is the normal Hubbard correlation energy, that would be applicable if no lattice relaxation were present.

It follows that if λ^2 / c is large enough, the correlation energy would become negative, and the disproportionated state will be energetically more favourable than two singly occupied states.

9.1.3 Properties of negative-U defects

There are a number of unusual properties that a defect with negative-U properties will have. Firstly, the neutral D^0 state is no longer thermodynamically stable. If two isolated neutral defects come into contact with each other (via the conduction band), they can lower their energy by ionizing and releasing the energy $|U|$, in a process similar to the well-known chemical phenomenon of *disproportionation* of ions in a liquid solution:

$$2D^0 \rightarrow D^+ + D^- + |U|$$

Therefore, in the ground state, a negative-U defect will always be in either the positively or the negatively ionised states, and the neutral state is always an excited state.

It follows therefore, that the donor and acceptor levels as described above, cannot be detected in the usual manner. For instance, Hall measurements would detect a single level located halfway between the donor and the acceptor levels. In the case of DLTS, if the experimental conditions are carefully chosen, it is possible to see thermal emission from both levels.

9.2 DLTS of a negative-U defect

In order to investigate how the negative-U level ordering of a defect might influence the DLTS spectrum, we first need to carefully consider how a negative-U defect behaves when the Fermi level is changed.

9.2.1 Behaviour of a negative-U defect under changing Fermi level.

The diagram in Figure 9.2 shows the energy levels of a defect D having three charge states D^-, D^0 and D^+. The energy levels shown correspond to transitions between the D^- and D^0 level (having acceptor character) and the D^0 and D^+ levels (having donor character). In the top diagram, the levels have normal (positive U) ordering, where the energy level of the donor level is below that of the acceptor, while the lower diagram shows the energy levels with negative U ordering.

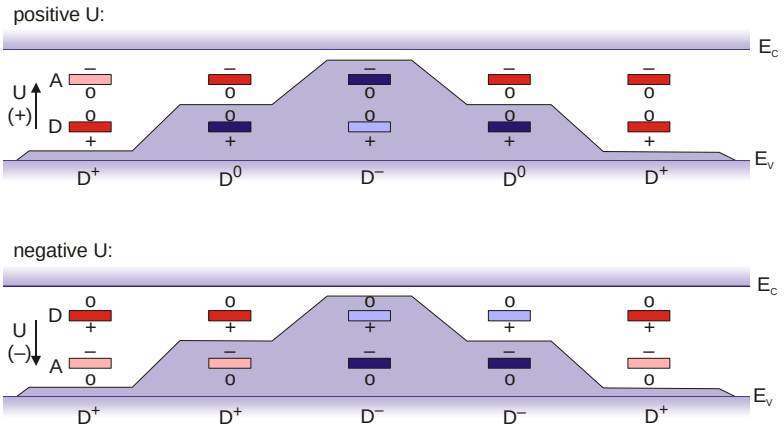

Figure 9.2 *A schematic energy-level diagram showing the behaviour of a defect D, having three charge states* D^-, D^0 *and* D^+.

Firstly consider what would happen if the Fermi level were moved from the valence band to the conduction band and back again. Initially, assume that the Fermi level is below both defect levels and that the defect is in the D^+ state (i.e. both acceptor and donor state empty), as shown at the left.

For positive U, if the Fermi level is now raised to above the donor level, it will capture an electron according to $D^+ + e^- \rightarrow D^0$. As the Fermi level is raised further, a second electron is captured when the Fermi level moves above the acceptor level, according to $D^0 + e^- \rightarrow D^-$, leaving the defect in the D^- state. If the Fermi level is now lowered again, the process is reversed, and the defect releases its first electron when the Fermi level falls below the acceptor level, and a second when the Fermi level falls below the donor level.

In the case of negative-U ordering, the matter becomes more complicated. Note that the first electron to be captured, corresponding to the donor level (i.e. $D^+ + e^- \rightarrow D^0$), has a *higher* energy than the second one. Furthermore, note that the acceptor level cannot capture an electron, because the defect is not in the D^0 state, as would be required by the reaction $D^0 + e^- \rightarrow D^-$. Therefore, as the Fermi level is raised, the defect does not capture an electron and remains in the D^+ state until the Fermi level reaches the donor level. Now the defect can capture one electron and go to its neutral D^0 state. However, as soon as the defect is in the D^0 state, the acceptor level becomes available, and since the acceptor level is also below the Fermi level, it will almost immediately capture a second electron, leaving the defect in its D^- state.

A similar situation occurs when the Fermi level is lowered. In this case, the defect does not emit an electron until the Fermi level is below the acceptor level. Once this electron is emitted, it is quickly followed by a second, since the donor level is now also above the Fermi level.

The result is that the defect with negative-U level ordering usually captures and emits two electrons in rapid succession. Furthermore, the Fermi level at which capture occurs is much higher than the Fermi level at which emission occurs. This behaviour leads to defect metastability. It is also clear that, since capture and emission of the two electrons occur in quick succession, the defect is in its unstable neutral condition for a very short time only.

9.2.2 DLTS of a negative-U defect

Figure 9.3 is a diagrammatic representation of the filling of a negative-U defect by a DLTS pulse. When a defect with negative-U level ordering is observed by means of DLTS using a relatively long filling pulse, the defect will behave in a similar fashion as we have just described – the filling pulse will fill the defect with two electrons. When the filling pulse is removed, the defect will eventually emit two electrons closely following each other. Since emission of the first electron takes much longer than emission of the second electron, the emission rate observed for this emission will essentially be that of the first electron. I.e. analysis of the DLTS signature will yield E_A .

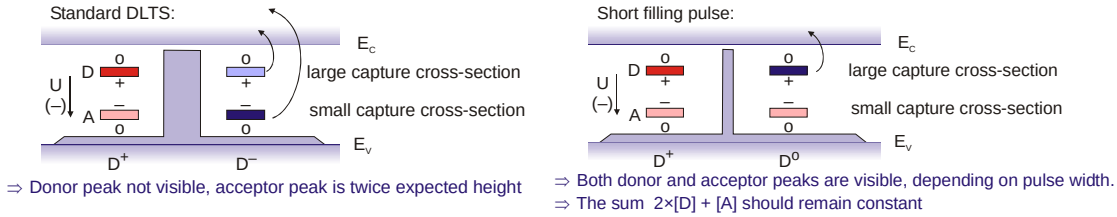

Figure 9.3 *A schematic energy-level diagram showing the behaviour of a defect D with negative U level ordering under a long and a short DLTS filling pulse.*

Since two electrons are involved, the DLTS peak will be twice as high as expected from the defect concentration. However, since the defect concentration is usually uncertain, this increase in peak height will not be noticed in a typical experimental study.

Consider, however, what would happen if a short filling pulse were applied. Since the donor level is positively charged when empty, it has a large capture cross section and will easily capture an electron. The acceptor level is neutral when empty, and will therefore have a lower capture cross-section. It follows that it might be possible, if a very short filling pulse is used, to fill mainly the donor level, leaving the acceptor level mostly empty. In this way, it could be possible to get a significant proportion of the defect in the excited D^0 state. Since the electrons in the donor state are less tightly bound than in the acceptor states, they will be emitted at a higher emission rate, as determined by E_D . Furthermore, since only a single electron was captured, only a single electron will be emitted per defect.

Thus, by varying the filling pulse length, it might be possible to vary the ratio between the number of defects that have captured only one electron, and those that have captured two electrons. In this case, the DLTS spectrum should show two peaks, one peak at high emission rates for single emission from the donor level, and a second peak with a lower emission rate, due to the emission of two electrons from the acceptor level.

As far as the peak height is concerned, the differing number of electrons per defect that are involved in each peak need to be considered. Since the acceptor level emits two electrons and the donor level only

a single electron it follows that peak heights h_A and h_D from the acceptor and donor levels respectively, should obey the relationship

$$2h_D + h_A = \text{const.} \tag{9.3}$$

The mechanism described above also leads to the paradoxical phenomenon that, after a certain filling pulse length, the height of the emission peak from the acceptor level actually *decreases* with *increasing* filling pulse length.

9.3 Negative U properties observed in a sputter-deposition induced defect in n-GaN.

The results of an investigation of sputter-deposition induced defects in OMVPE-grown n-GaN are published in the paper Auret (1999), included at the end of this chapter. In the following section, some of the aspects of this paper are discussed in more detail.

9.3.1 Introduction

Gallium nitride (GaN) is a direct, wide band gap semiconductor with a number of applications including blue and ultraviolet light emitting diodes, lasers and detectors as well as high temperature and power electronics. In the manufacturing of contacts to GaN, adhesion is a significant problem. The best adhesion results by far are obtained by sputter deposition. However, sputter deposition involves energetic particles that induce defects in the crystal lattice. In this paper, the properties of a specific defect, induced by sputter deposition of Au Schottky contacts, are discussed.

9.3.2 Experimental

The sample preparation was as described previously for GaN in Section 5.2.3. The initial measurements were performed on an LIA-DLTS system. However, after it became clear that the flexibility of the digital DLTS system was required, the measurements were continued on this system.

Since very fast pulses were required, the usual Agilent 32210 A pulse generator was used to trigger an Agilent 8110A pulse generator, which could provide much shorter pulses. Furthermore, since the internal bias filtering circuit of the Boonton 7200 would filter out such short pulses, a fast pulse interface as described in Section 4.3.1 was used to bypass the capacitance meter. By means of reed relays, the fast pulse interface could switch the sample directly to the output of the pulse generator and back in less than 1 ms, during which time the pulse was applied. During set up, care was taken to ensure that the timing of the relays was such that the sample was always connected to a reverse bias, and that there was no possibility of contact being lost due to contact bounce in the reed relays.

9.3.3 Results and discussion

Figure 9.4 shows an LIA-DLTS spectrum obtained from a sputter deposited Au Schottky contact on n-GaN. The top curve shows the DLTS spectrum of the sample, recorded after cooling the sample under a reverse bias. The second curve is of the same sample recorded under the same conditions, except that a 0.35 V forward bias was applied while the sample was at 60 K. The application of this pulse caused the ES1 peak to disappear from the spectrum that was subsequently recorded. Taking the sample to room temperature again and repeating the procedure, re-introduced the ES1 peak.

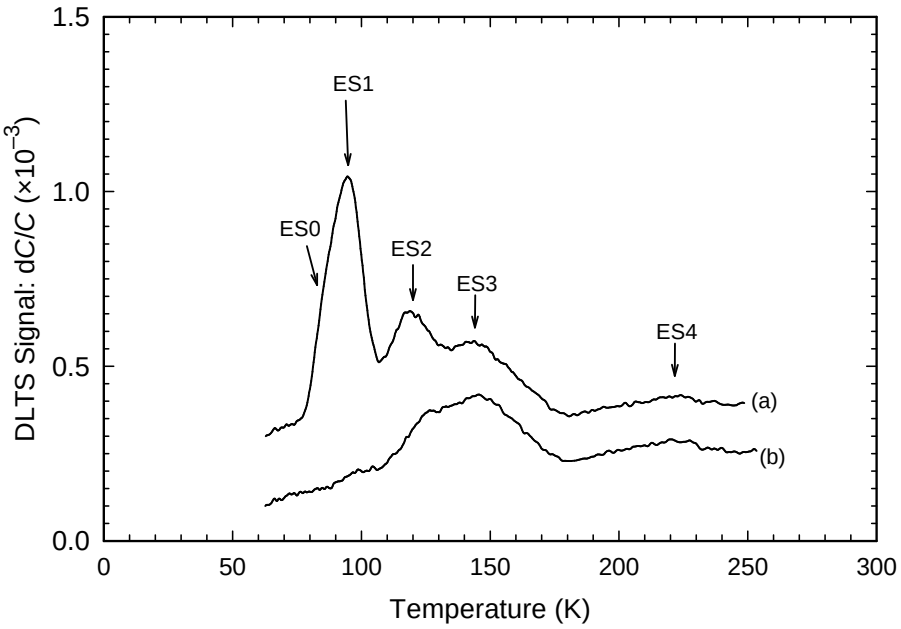

Figure 9.4 *DLTS spectra of a sputter deposited Schottky contact using* $V_r = 1.0$ V, $V_p = 1.35$ V *and* $f = 22$ Hz. *Curve (a) was recorded after cooling under reverse bias, while curve (b) was recorded after application of 0.35 V forward bias at 60 K.*

Figure 9.5 shows the isothermal DLTS spectrum obtained at 100 K, for differing pulse lengths. The spectrum shows interesting behaviour: The longer the filling pulse, the lower the amplitude of the DLTS peak. However, this is exactly the paradoxical behaviour one would expect from a negative-U defect, as discussed in section 9.2.2. As described in section 9.2.2, one possible explanation for this behaviour is that the ES1 level belongs to a defect that has another charge state in the band gap and that these levels display negative-U ordering. A short filling pulse fills only the donor level, and the associated electron is quickly released and therefore visible on the DLTS spectrum. However, when a forward bias is applied to the sample for a longer period, two electrons are captured. Since these electrons are now more tightly bound, the electrons are not emitted as fast as previously, causing the amplitude of the peak due to the donor level to decrease. As the pulse length of the filling pulse is increased, eventually all the defects will be filled with two electrons, and no transient due to the donor level will be observed.

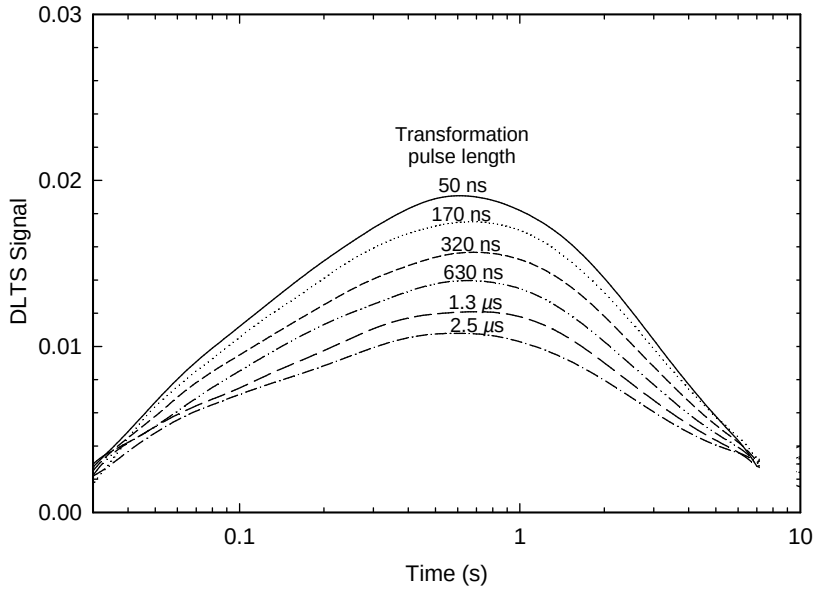

Figure 9.5 *An isothermal DLTS spectrum recorded by the digital DLTS system at 100 K (after cooling the sample from room temperature under reverse bias). The measurement conditions were* $V_r = 1.0$ V , $V_p = 1.5$ V .

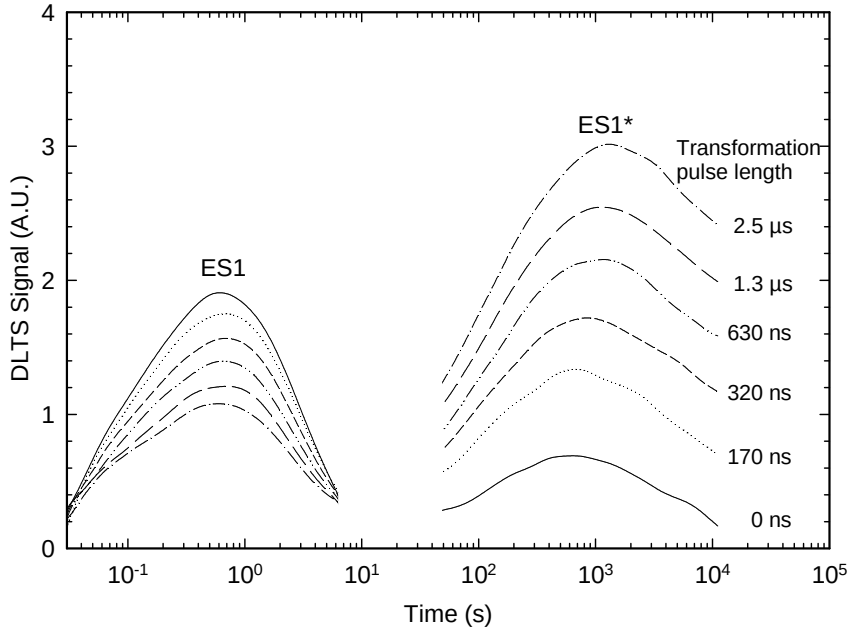

Figure 9.6 *An isothermal DLTS spectrum showing both the ES1 and the ES1* emission peaks after the application of transformation pulses of differing lengths. Recorded by the digital DLTS system at 100 K (after cooling the sample from room temperature under reverse bias). The measurement conditions were* $V_r = 1.0$ V , $V_p = 1.5$ V .

In this case, it seems likely that the emission rate of the peak associated with the acceptor level is so low, that it could not be detected by the LIA-DLTS system. However, since the digital DLTS system allows much longer transients to be measured, an attempt was made to detect this peak. The isothermal DLTS spectrum of the sample recorded up to 10 000 s at 100 K is shown in Figure 9.6.

The graph in Figure 9.6 shows a second peak, labelled the ES1*. The ES1* had a much lower emission rate, which explains why it could not be observed by LIA-DLTS. As expected, the height of the ES1* increased with increasing filling pulse width, and its maximum height was about twice the maximum height of the ES1.

In order to test whether the ES1 and the ES1* obey the relationship given in Equation (9.3), the DLTS transient was recorded after the application of differing lengths of transformation pulse. The exact procedure involved cooling the sample under reverse bias from room temperature to 100 K. Here after, a variable “transformation pulse” was applied. The sample was then left under reverse bias for approximately 100 seconds, after which a 50 ns filling pulse was applied and the transient recorded. The reason for this procedure was that the longer transformation pulses also filled other defects, with emission rates close to that of the ES1. By allowing the transient due to these defects to decay, and then applying a 50 ns filling pulse, the accuracy of this measurement was improved. Figure 9.7 shows the transients thus obtained.

From the transient, it is clear that there were two defect levels involved – one with a fast emission rate, and another with a slow emission rate. It can also be seen that the fast transient dominates after a short transformation pulse, while the slow transient dominates after a long transformation pulse.

The capacitance of the transient was measured 5 ms, 10s and 10 000 s after the start of the scan. The difference between the first two readings was assumed to be due to the ES1 and the difference between the second two readings was assumed to be due to the ES1*. The change in capacitance due to these two peaks for different pulse lengths is plotted in Figure 9.8.

Also plotted in Figure 9.8 is the sum of the capacitance change due to ES1 and twice the capacitance change due to ES1*. According to Equation (9.3), this should be a constant. It is interesting that, although the value remains more or less constant, there is a clear systematic sagging in the middle. It is not clear what the reason for this sagging might be.

A further prediction made by our negative-U model, is that ES1 should be a donor and ES1* should be an acceptor. As discussed in Section 2.2.3, the field dependence of the emission rate from a defect gives an indication of its charge state. The results of such a measurement are shown in Figure 9.9. Here the results were exactly as expected: Emission from the ES1 showed a significant dependence, that was well described by the three dimensional Poole-Frenkel effect, while emission from the ES1* showed very little field dependence. It is therefore reasonable to assume that the ES1 is a donor while the ES1* is an acceptor.

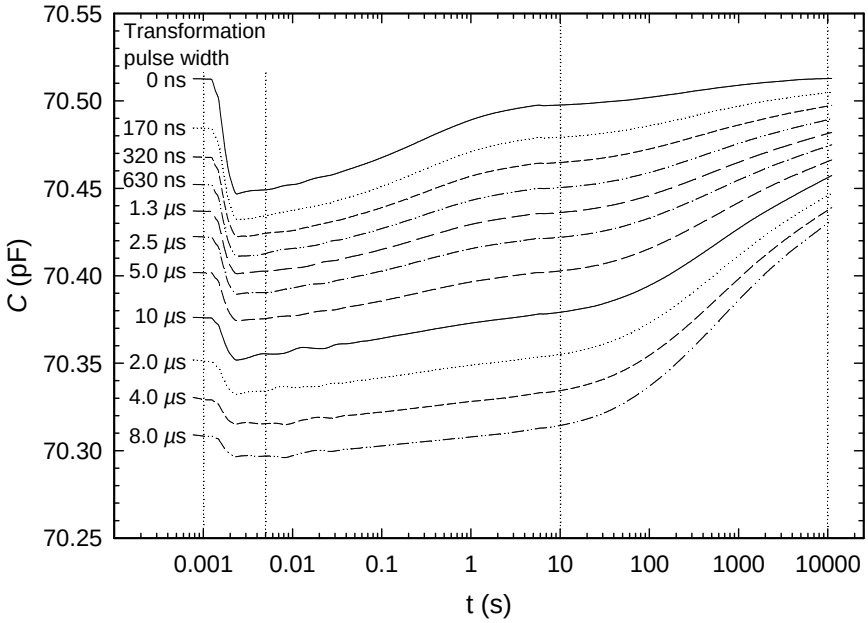

Figure 9.7 *Capacitance transients recorded from the sample after transformation pulses with differing lengths were applied to the sample. The measurements were taken at 100 K under a quiescent reverse bias of 1.0 V. The transformation pulse had an amplitude of 1.5 V and was applied 30 s before the start of the scan. The filling pulse also had an amplitude of 1.5 V, a pulse width of 50 ns, and was applied 1.5 ms after the start of the scan.*

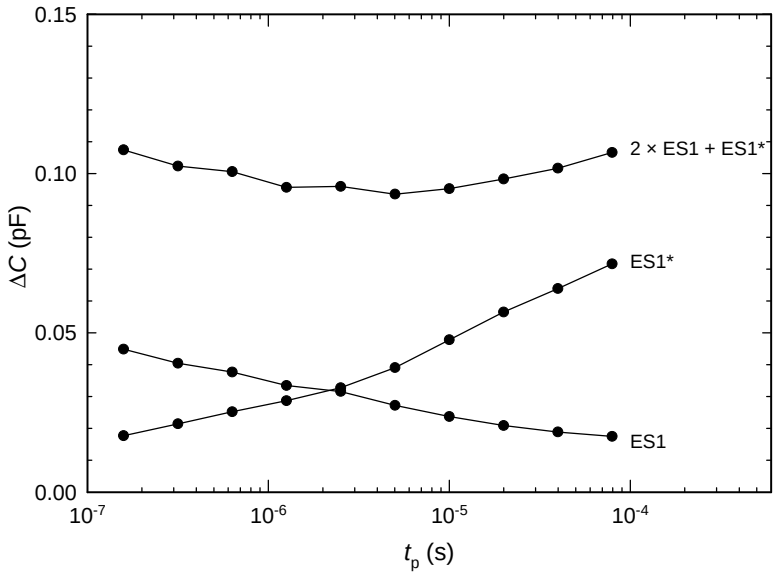

Figure 9.8 *Change in capacitance due to the ES1 and the ES1* after the application of differing transformation pulse lengths.*

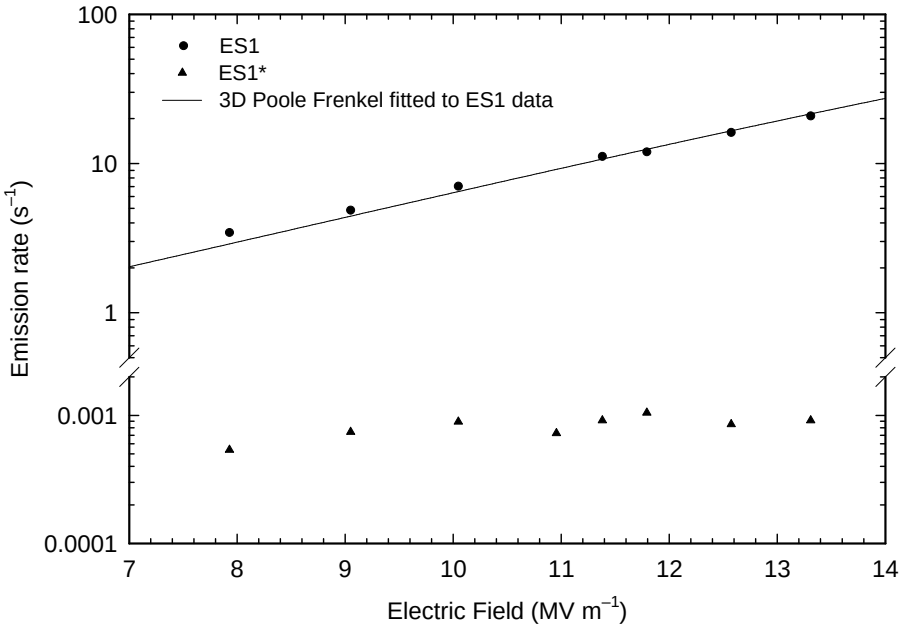

Figure 9.9 *Field dependence of the emission rate from the ES1 and ES1* level, as measured by DLTS.*

9.3.4 Conclusion

It is clear that the digital DLTS system provided a significant advantage over the analogue LIA-based DLTS system. The properties of the ES1 and ES1* levels of a sputter induced defect have been measured. ES1 and ES1* have the property that, depending on the length of the filling pulse, either ES1 or ES1* or both are visible. Over this range the quantity 2 × [ES1] + [ES1*] remains approximately constant. From the results it seems as though the ES1 and ES1* levels both belong to the same defect, that displays negative-U ordering of its energy levels. Field dependence of the emission rate from the ES1 and ES1* indicate that the ES1 is probably a donor and ES1* probably an acceptor. This is further evidence that points to negative-U properties of the defect.

9.4 Publications

The results of this investigation were published in the publication:

1. Auret FD, Meyer WE, Goodman SA, Koschnick FK, Spaeth J-M, Beaumont B and Gibart P (1999), Metastable-like behaviour of a sputter deposition induced electron trap in n-GaN *Physica B* **273-274** 92

ELSEVIER

Physica B 273–274 (1999) 92–95

PHYSICA B

www.elsevier.com/locate/physb

Metastable-like behaviour of a sputter deposition-induced electron trap in n-GaN

F.D. Auret[a,*], W.E. Meyer[a], S.A. Goodman[a], F.K. Koschnick[b], J.-M. Spaeth[b], B. Beaumont[c], P. Gibart[c]

[a]*Department of Physics, University of Pretoria, Pretoria 0002, South Africa*
[b]*Fachbereich Physik, Universität GH Paderborn, Paderborn, Germany*
[c]*CRHEA-CNRS, Valbonne, France*

Abstract

We show that a deep level, the ES1, introduced in n-GaN by sputter-deposition of gold Schottky contacts exhibits metastable-like behaviour during temperature cycling between 55 and 250 K. The ES1 has an energy level 0.22 ± 0.02 eV below the conduction band. We provide some evidence that indicates that the defect responsible for the ES1 has a second energy level, the ES1*, and that the metastable behaviour of the ES1 may be due to negative-U ordering of these two energy levels. Furthermore, field effect measurements indicate that the ES1 level has a donor character, while the ES1* level is probably an acceptor. © 1999 Elsevier Science B.V. All rights reserved.

Keywords: GaN; DLTS; Sputter deposition

1. Introduction

Gallium nitride, a direct, wide band-gap semiconductor, has a number of unique applications including blue, green and ultraviolet light emitting diodes, blue lasers, detectors and high temperature and power electronics devices [1,2]. An essential step in device manufacture is the deposition of a metal film that has to form ohmic or Schottky contacts to the semiconductor. This metal film is frequently deposited by means of sputter deposition. This technique has the advantage that it facilitates the stoichiometric deposition of compounds as well as the deposition of metals with a high melting point. In addition, sputter-deposited layers exhibit far better adhesion compared to layers deposited by other methods [3]. The main disadvantage of sputter deposition is that it involves energetic particles that may damage the crystal lattice and produce defects at and below the surface of the semiconductor [4]. In many cases these defects give rise to energy levels in the semiconductor band gap which are electrically active and may act as trapping or recombination levels. These defects can be observed by means of deep level transient spectroscopy (DLTS) [5].

Some defects in semiconductors exhibit charge state controlled metastable behaviour. That is, they can exist in different configurations, with the stable configuration depending on the charge state of the defect [6]. Such charge state controlled metastability allows for the reversible introduction and removal of defects in a semiconductor, and leads to a number of interesting phenomena, for instance the number and energy of the deep levels observed in a sample may depend on the bias conditions under which the sample was cooled. The metastability of defects is also of technologically importance, since the presence of a metastable defect in a device may lead to electrical properties that depend on the history of the sample, thus leading to unreliable device characteristics.

In this paper we discuss some of the metastable properties of defects introduced in n-GaN during sputter deposition of Au Schottky contacts.

* Corresponding author. Tel.: +27-12-420-2684; fax: +27-12-362-5288.

E-mail address: fauret@scientia.up.ac.za (F.D. Auret)

PII: S0921-4526(99)00414-7

2. Experimental procedure

We used epitaxial n-GaN grown by organo-metallic vapour-phase epitaxy (OMVPE), with a free carrier density of $2–3 \times 10^{16}$ cm^{-3} as determined by capacitance–voltage (CV) measurements. The samples were cleaned [7] by boiling them in aqua-regia. After rinsing the samples in de-ionized water, the samples were degreased in boiling trichloroethylene followed by rinsing in boiling isopropanol and in de-ionized water. Finally, the samples were dipped in a 50% HCl solution for 10 s. Ohmic contacts, consisting of 150 Å/2 200 Å/400 Å/500 Å layers of Ti/Al/Ni/Au [8], were deposited by means of electron beam evaporation and annealed at 500°C for 5 min in Ar. The samples were again degreased and dipped in a 50% HCl solution before deposition of the Schottky contacts. The Schottky contacts, 0.5 mm in diameter and 1 μm thick were sputter-deposited on the GaN through a metal contact mask [9]. For control purposes, Au SBDs were resistively deposited next to the sputter deposited SBDs.

The defects were characterized by means of a lock-in amplifier (LIA) based DLTS system, using a Boonton 7200 capacitance meter and a Stanford Research model SR830 LIA, which facilitates transient analysis at pulse frequencies as low as a few mHz. In order to measure single-shot events, an isothermal DLTS system was used. In this system, the capacitance transient from the Boonton 7200 was captured by an HP 3458 A multimeter and processed by a microcomputer. This isothermal DLTS system also allowed the measurement of DLTS transients lasting as long as a couple of hours. Therefore, it was possible to observe defects at temperatures much lower than those at which they are commonly observed by an LIA-based DLTS system.

The energy level in the band gap, E_T, and the apparent capture cross section σ_n of the defect (collectively known as the defect's 'signature'), were calculated from Arrhenius plots of T^2/e versus $1/T$, where e is the emission rate at temperature T.

In order to allow for measurements with short (down to 50 ns) filling pulses, a set of reed relays were used to connect the sample directly to the pulse generator and to disconnect the capacitance meter from the sample. To ensure that the sample was not inadvertently exposed to a filling pulse care was taken to ensure that the capacitance meter was only disconnected after the pulse generator was connected to the sample and no more contact-bounce was observed. Special precautions were taken to avoid any pulses being applied to the sample prior to the measurements. The absence of filling pulses was confirmed by monitoring the voltage across the samples with a fast (200 MHz) storage oscilloscope.

3. Results and discussion

The DLTS spectra of the resistively deposited control sample as well as the sputter-deposited diodes are shown in Fig. 1 curves (a) and (b), respectively. The energy levels and apparent capture cross sections of the sputter-induced defects are summarized in Table 1 [10].

Fig. 2 illustrates the metastable properties exhibited by the ES1 defect. Both curves (a) and (b) were recorded after cooling the sample under reverse bias. However, before curve (a) was recorded, the sample was exposed to a forward bias of 0.35 V. This forward bias pulse seems to reversibly remove the ES1 and ES2 defects. Both defects could be re-introduced by heating the sample under reverse bias to over 150 K. Further investigation using the isothermal DLTS system, showed that the height of the ES1 defect was decreased by an increase in the length of the filling pulse. This is contrary to the usual case, where an increase in the length of the filling pulse increases the height of the DLTS peak. It seems therefore that the capture of an electron in some way decreases the height of the ES1.

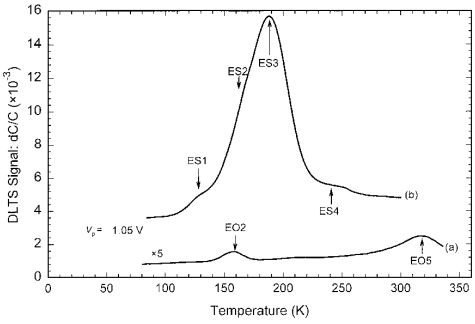

Fig. 1. DLTS spectrum of a resistively deposited control SBD (curve (a)) and a sputter deposited Schottky barrier (curve (b)) on epitaxial GaN ($V_p = 1.2$ V, $t_p = 0.2$ ms, $f = 46$ Hz).

Table 1
Electronic properties of sputter deposition induced defects in epitaxial n-GaN

Defect label	E_T (eV)	σ_a (cm^2)	T_{peak}[a] (K)
ES0	—	—	—
ES1	0.22 ± 0.02	$6.5 \pm 2.0 \times 10^{-16}$	< 120
ES2	0.30 ± 0.01	$4.4 \pm 1.0 \times 10^{-14}$	157
ES3	0.40 ± 0.01	$3.3 \pm 1.0 \times 10^{-13}$	192
ES4	0.45 ± 0.10	$8.1 \pm 2.0 \times 10^{-16}$	249

[a]Peak temperature at a lock-in amplifier frequency of 46 Hz, i.e. a decay time constant of 9.23 ms.

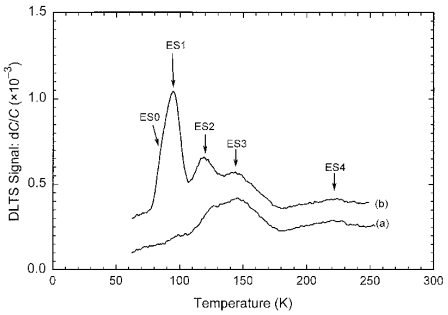

Fig. 2. DLTS spectra of a sputter deposited Schottky contact using $V_r = 1.0$ V, $V_p = 1.35$ V, $f = 0.22$ Hz. Curve (a) was recorded after cooling under reverse bias, while curve (b) was recorded after application of 0.35 V forward bias at 60 K.

One possible explanation for this behaviour is a phenomenon known as negative-U [11]. According to this explanation, the ES1 defect is one energy level of a defect that has two energy levels in the band gap (i.e. the defect can trap two electrons). If the defect has already captured one electron, the second electron the defect captures would be repelled by coulomb interactions with the first electron. This implies that the second electron should be less tightly bound than the first electron. This difference in binding energy is referred to as U, and is usually positive. However, in some defects, there may be some interaction with the lattice that causes the second electron to be more tightly bound than the first, i.e. U is negative. A classical case in which negative-U properties have been demonstrated is the boron interstitial in silicon [12].

In the case of the ES1 deep level, the short (50 ns) filling pulse is just long enough to fill the defect with one electron. After the defect has captured one electron, the capture cross section of the defect decreases dramatically, due to the change in the charge state of the defect. Therefore, the defect will not capture another electron as easily as it captured the first. After the filling pulse, the electron is easily emitted and gives rise to the ES1 peak observed in the DLTS spectrum.

If a long filling pulse is applied, the defect will capture a second electron. However, due to the negative-U ordering of these two energy levels, the second electron to be captured is more tightly bound than the first. Therefore this electron is emitted at a significantly lower rate than the first, and should give rise to another defect level with a lower emission rate, which we shall refer to as the ES1*. The first electron to be emitted is now rapidly followed by the emission of a second electron to be emitted (since the second electron is more weakly bound than the first). This implies that the ES1* should have twice the height of the ES1.

If a filling pulse with a length falling between the two extremes is applied, some of the defects will have captured a single electron, while others will have captured two electrons. Emission from these defects will give rise to both the ES1 and the ES1* DLTS peaks. It follows from the above argument that the heights of the peaks should be related by

$$2 \times [\mathrm{ES1}] + [\mathrm{ES1}^*] = \text{constant}. \quad (1)$$

In order to investigate the possibility of the ES1 belonging to a defect having negative-U properties, an attempt was made to look for evidence of a second energy level. Further investigations with the isothermal DLTS system showed that, as the peak due to the ES1 disappeared, a second peak with a much lower emission rate appeared. This second peak will be referred to as the ES1*. The isothermal DLTS spectrum obtained for the ES1 and ES1* after the application of different filling pulses is shown in Fig. 3. Here it can be clearly seen that the height of the ES1* (peak at 1000 s) increases as the height of the ES1 (peak at 0.6 s) decreases.

In order to confirm the relationship predicted by Eq. (1), the charge involved in each of the DLTS peaks was estimated by measuring the change in capacitance associated with each of the peaks. Fig. 4 shows this capacitance change for both peaks as a function of filling pulse length. Also shown is the value of $2 \times [\mathrm{ES1}] + [\mathrm{ES1}^*]$, which is approximately constant. The systematic deviation observed should still be investigated further, but it could be due to the field dependence of the emission rate or an inaccurate determining of the baseline position of partly overlapping peaks in Fig. 3.

In order to obtain some further insight into the properties of the ES1 and the ES1*, the field dependence of the emission rate from these defects was determined. This property is frequently used to estimate the shape of the potential well of a defect and to distinguish between

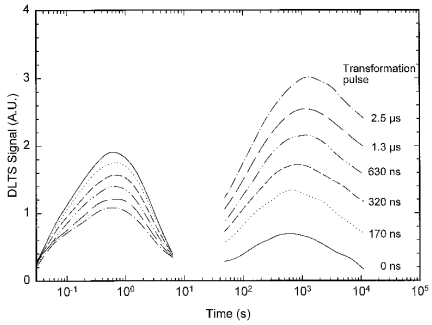

Fig. 3. Isothermal DLTS spectra obtained after the application of filling pulses with different lengths. Note that the height of the ES1 peak (at 0.6 s) decreases as that of the ES1′ (at 1000 s) increases. ($V_r = -1$ V, $V_p = 1.5$ V, $T = 100$ K).

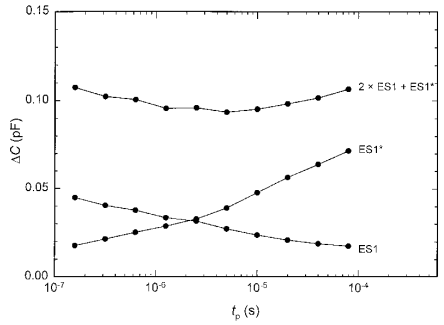

Fig. 4. Capacitance change associated with the ES1 and the ES1* after the application of different filling pules. The third curve corresponds to $2\times[ES1] + [ES1^*]$.

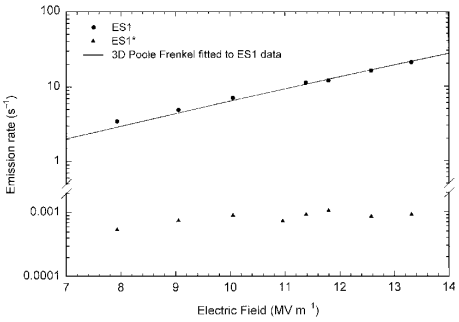

Fig. 5. Field dependence of the emission rate from the ES1 and ES1* defects as determined by means of isothermal DLTS at 100 K.

donor and acceptor levels [13]. The results of these measurements are shown in Fig. 5, which shows that the emission from the ES1 is strongly field dependent while the emission from the ES1* is much less dependent on the electric field.

If it is assumed that the field enhanced emission from the ES1 and ES1* is due to the Poole–Frenkel lowering of the barrier height, it follows that the potential well of the ES1 has to be much wider than that of the ES1*. A more quantitative approach can be followed by fitting the theoretical curve for the Poole–Frenkel field enhanced emission from a Coulombic well [13] to the field dependent emission data obtained for the ES1 (see Fig. 5). The excellent fit obtained indicates that the field enhanced emission from the ES1 is consistent with the Poole–Frenkel emission from a three-dimensional coulombic well, and therefore the ES1 is probably a donor. The weak dependence of the emission from the ES1* on the electric field, combined with the lower capture cross section, indicates that the ES1* is probably an acceptor.

4. Conclusions

We have reported some of the transformational properties of a sputter-induced metastable defect in n-GaN. The unusual transformational properties of the defect can be explained by assuming that the defect has two energy levels in the band gap, ES1 and ES1*, with negative-U ordering. The ES1 level is the same level that was previously reported in n-GaN with an energy level 0.22 ± 0.02 eV below the conduction band. We have used field effect measurements to show that this level is probably a donor. In contrast to the ES1, emission from the ES1* is much less sensitive to the electric field. It is therefore speculated that the ES1* is an acceptor. Although the evidence for the negative-U properties of this defect is not conclusive, it is hoped that further investigation could provide a definite answer.

Acknowledgements

We gratefully acknowledge financial assistance from the South African Foundation for Research Development. We also thank G. Myburg for ohmic contact metallization and C. Schutte and C. du Toit for sputter deposition.

References

[1] S. Nakamura, G. Fasol, The Blue Laser Diode, Springer, Berlin, 1997.
[2] K. Doverspike, A.E. Wickenden, S.C. Binarii, D.K. Gaskill, J.A. Freitas, Mater. Res. Soc. Symp. Proc. 395 (1996) 897.
[3] L.I. Maissel, in: L.I. Maissel, R. Glan (Eds.), Handbook of Thin Film Technology, McGraw-Hill, New York, 1970, pp. 1–4.
[4] F.H. Mullins, A. Brunnschweiler, Solid State Electron. 19 (1976) 47.
[5] D.V. Lang, J. Appl. Phys. 45 (1974) 3023.
[6] A. Chantre, Appl. Phys. A 48 (1989) 3.
[7] P. Hacke, T. Detchprohm, K. Hiramatsu, N. Sawaki, Appl. Phys. Lett. 63 (1993) 2676.
[8] S. Ruvimov, Z. Liliental-Weber, J. Washburn, K.J. Duxstad, E.E. Haller, Z.-F. Fan, S.N. Mohammed, W. Kim, A.E. Botchkarev, H. Morkoc, Appl. Phys. Lett. 69 (1996) 1556.
[9] F.D. Auret, S.A. Goodman, F.K. Koschnick, J.-M. Spaeth, B. Beaumont, P. Gibart, Appl. Phys. Lett. 74 (1999) 2173.
[10] F.D. Auret, S.A. Goodman, F.K. Koschnick, J.-M. Spaeth, B. Beaumont, P. Gibart, Mater. Sci. Eng. (1999), submitted for publication.
[11] G.D. Watkins, Negative-U properties for Defects in Solids, Festkörperprobleme XXIV, 1984, p. 163.
[12] J.R. Troxell, G.D. Watkins, Phys. Rev. B 22 (1980) 593.
[13] J.L. Hartke, J. Appl. Phys. 39 (1968) 4871.

10 Conclusions

The research contained in this thesis is an excerpt of the investigations done by means of the digital DLTS system. Conclusions specific to each of the experimental sections are given in the text or in the included papers. In this section, the conclusions regarding the digital DLTS system are summarised.

Selection and characterisation of the instrumentation

The study showed that it is important that great care be taken in selecting the instrumentation for the DLTS system. Rough guidelines regarding the specifications of the equipment are given in Chapter 4.

A number of pulse generators were investigated and it was found that some of the less expensive pulse generators, such as the Agilent 33120A performed much better than more expensive models. Also, a number of modifications and additions to the standard DLTS set up, that allowed special measurements to be made, were described.

Characterisation of the EL2 and the E2 defect in n-GaAs

The emission from the EL2 defect in n-GaAs could be measured over a much wider temperature range than would be possible with an analogue DLTS system. The results obtained for the EL2 agree well with results previously obtained by means of an analogue DLTS system, as well as with the values quoted in literature. The results indicate that the digital system could accurately measure emission rates from below 10^{-3} s^{-1} to more than 10^{3} s^{-1}.

The ability of the digital DLTS system to measure very long transients allowed the observation of unusual phenomena, such as emission from the E2 defect stimulated by thermal radiation from the inner shroud of the cryostat.

Field dependence of the thermally activated emission rate

The field-enhanced emission from a number of defects was measured. The results appear in the relevant papers referenced in Chapter 7. The results agreed well with the relevant theory.

DLTS observation of the transformation of bistable defects

The digital DLTS system allowed single transients to be digitised. This made it possible to characterise the transformation of a metastable defect in *p*-Si much more accurately than was possible with an analogue system. This research clearly shows the superiority of the digital system when compared to an analogue system.

Negative-U defects in n-GaN

Again, the ability of the digital DLTS system to analyse single transients allowed the properties of a sputter-deposition-induced defect in *n*-GaN to be analysed in detail. The results obtained give strong evidence that the defect has negative-U properties. As was the case with the previous investigation, it would certainly not be possible to obtain these results using an analogue DLTS system.

General

It is clear that the digital DLTS system described in this thesis has a number of advantages over the analogue LIA-based system. These include:

- A wider range of emission rates (both longer and shorter) could be observed;
- The isothermal technique allows for more accurate temperature determination;
- "Single shot" measurements allowed the observation of phenomena that are not observable in a LIA-based system;
- Wide variations in pulse length can easily be accommodated;
- Digital acquisition of the capacitance transient allows for measurements on a single transient.

Further research

Since the original design and construction of the system, there were huge advances in the computational power and ADC technology. A more modern system, controlled by a friendlier user interface such as LabView, using a commercial ADC card, might give even more flexibility at lower cost. Furthermore, computational power is now fast enough to allow for more advanced analysis techniques, for instance the Gaver-Stehfest analysis technique investigated by Istratov.

References

Anderson PW 1975 Model for the Electronic Structure of Amorphous Semiconductors *Phys. Rev. Lett.* **34** 953

Auret FD, Goodman SA and Meyer WE 1998 Field enhanced emission kinetics of an as-grown defect in RMBE grown n-GaN *Proc. 24th Int. Conf. Phys. Semicond.* ed D Gershoni (Singapore: World Scientific)

Auret FD, Meyer WE, Goodman SA, Koschnick FK, Spaeth J-M, Beaumont B and Gibart P 1999 Metastable-like behaviour of a sputter deposition-induced electron trap in n-GaN *Physica B* **273-274** 92

Baliga BJ 1996 *Power semiconductor devices* (PWS Pub. Co.)

Bardeen J 1947 On the theory of the AC impendance of a contact rectifier *Bell Syst. Tech. J.* **28** 428

Bourgoin J and Lannoo M 1983 *Point defects in semiconductors II* (Berlin: Springer)

Chantre A 1987 Metastable thermal donor states in silicon *Appl. Phys. Lett.* **50** 1500

Chantre A 1989 Introduction to defect bistability *Appl. Phys. A* **48** 3

Chappell TI and Ransom CM 1984 Modifications to the Boonton 72BD capacitance meter for deep-level transient spectroscopy applications *Rev. Sci. Instrum.* **55** 200

Chen MC, Lang DV, Dautremont-Smith WC, Sergent AM and Harbison JP 1984 Effects of leakage current on deep level transient spectroscopy *Appl. Phys. Lett.* **44** 790

Christoforou N and Leslie JD 1991 Capacitance switching method of eliminating false transients on the Boonton 72B capacitance meter in deep level transient spectroscopy applications *Meas. Sci. Technol.* **2** 127

Cowley AM 1965 Depletion capacitance and diffusion potential of gallium phosphide Schottky-barrier diodes *J. Appl. Phys.* **37** 3024

Deenapanray PNK, Meyer WE and Auret FD 1999 Electric-field-enhanced emission and annealing behaviour of electron traps introduced in n-Si by low-energy He-ion bombardment *Semicond. Sci. Technol.* **14** 41

Dobaczewski L, Kaczor P, Hawkins ID and Peaker AR 1994 Laplace transform deep-level transient spectroscopic studies of defects in semiconductors *J. Appl. Phys.* **76** 194

Dobaczewski L, Kaczor P, Missous M, Peaker AR and Zytkiewicz Z 1992 Evidence for substitutional-interstitial defect motion leading to DX behaviour by donors in $Al_xGa_{1-x}As$ *Phys. Rev. Lett.* **68** 2508

Frenkel J 1938 On Pre-breakdown Phenomena in Insulators and Electronic Semi-Conductors *Phys. Rev.* **54** 647

Goodman SA, Auret FD and Meyer WE 1994 The effect of alpha-particle and proton irradiation on the electrical and defect properties of *n*-GaAs *Nucl. Instr. Meth. Phys. Res. B* **90** 349

Goodman SA, Auret FD, Koschnick FK, Spaeth J-M, Beaumont B and Gibart P 1999 Field-enhanced emission rate and electronic properties of a defect introduced in n-GaN by 5.4 MeV He-ion irradiation *Appl. Phys. Lett.* **74** 809

Goodman SA, Auret FD, Meyer WE, Koschnick FK, Spaeth J-M, Beaumont B and Gibart P 1998 Deep level defects introduced in n-GaN by 5.4 MeV He-ions *Proc. 24th Int. Conf. Phys. Semicond.* ed D Gershoni (Singapore: World Scientific)

Greulich-Weber S, Görger A, Spaeth J-M and Overhof H 1991 Iron-aluminum pairs in silicon *Appl. Phys. A* **53** 147

Hacke P, Detchprohm T, Hiramatsu K and Sawaki N 1993 Schottky barrier on n-type GaN grown by hydride vapor hase epitaxy *Appl. Phys. Lett.* 63 2676

Hall RN 1952 Electron-Hole Recombination in Germanium *Phys. Rev.* **87** 387

Hartke JL 1968 The Three-Dimensional Poole-Frenkel Effect *J. Appl. Phys.* **39** 4871

Henisch HK 1989 *Semiconductor contacts* (Oxford: Clarendon)

Henry PM, Meese JM, Farmer JW and Lamp CD 1985 Frequency-scanned deep-level transient spectroscopy *J. Appl. Phys.* **57** 628

Hubbard J 1963 Electron correlations in narrow energy bands *Proc. Roy. Soc.* **A276** 238

Istratov AA 1997 New correlation procedure for the improvement of resolution of deep level transient spectroscopy of semiconductors *J. Appl. Phys.* **82** 2965

Istratov AA, Vyvenko OF, Hieslmair H and Weber ER 1998 Critical analysis of weighting functions for the deep level transient spectroscopy of semiconductors *Meas. Sci. Technol.* **9** 477

Jackson JD 1975 *Classical Electrodynamics* (New York: Wiley)

Jacoby WG 2000 Loess: a nonparametric, graphical tool for depicting relationships between variables *Electoral Studies* **19** 577

Jaros M 1982 *Deep levels in semiconductors* (Bristol: Hilger)

Kaczor P, Żytkiewicz ZR, Godlewski M and Dobaczewski L 1993 X_1-X_3 conduction-band splitting of $Al_xGa_{1-x}As$ observed in far-infrared photoinduced absorption related to the DX defect *Phys. Rev. B.* **47** 12558

Kaminska H and Weber ER 1993 EL2 Defect in GaAs *Semiconductors and Semimetals Volume 38: Imperfections in III/V Materials* ed ER Weber (Boston: Academic)

Korol EN 1977 Ionization of Impurity States by an Electric Field *Sov. Phys. Solid State* **19** 1327

Lang DV 1974 Deep-level transient spectroscopy: A new method to characterize deep traps in semiconductors *J. Appl. Phys.* **45** 3023

Lannoo M and Bourgoin J 1981 *Point defects in semiconductors I* (Berlin: Springer)

Lefèvre H and Schulz M 1977 Double correlation technique (DDLTS) for the analysis of deep level profiles in semiconductors *Appl. Phys. A* **12** 45

Levinson M 1985 Capacitance transient analysis of configurationally bistable defect in semiconductors *J. Appl. Phys.* **58** 2628

Makram-Ebeid S and Lannoo M 1980 Effect of electric field on deep-level transients in GaAs and GaP *Appl. Phys. Lett.* **37** 464

Mamor M, Auret FD, Goodman SA, Meyer WE and Myburg G 1998 Electronic and transformation properties of a metastable defect introduced in epitaxially grown boron-doped p-type Si by alpha particle irradiation *Appl. Phys. Lett.* **72** 3178

Mamor M, Willander M, Auret FD, Meyer WE and Sveinbjörnsson E 2000 Configurationally metastable defects in irradiated epitaxially grown boron-doped p-type Si *Phys. Rev. B* **63** 045201

Mandl F 1988 *Statistical Physics* (Chichester: Wiley)

Martin M and Makram-Ebeid S 1986 *Deep Centers in Semiconductors* ed ST Pantelides (New York: Gordon and Breach)

Meyer WE and Auret FD 2004 Effect of thermal radiation on electron emission from the E2 defect in n-GaAs *Phys. Stat. Sol. (c)* ***1*** *2333*

Miller GL, Lang DV and Kimerling LC 1977 Capacitance Transient Spectroscopy *Ann. Rev. Mater. Sci.* **7** 377

Myburg G and Auret FD 1992 Influence of the electron beam evaporation rate of Pt and the semiconductor carrier density on the characteristics of Pt/*n*-GaAs Schottky contacts *J. appl Phys* **71** 6172

Myburg G, Meyer WE and Auret FD 1992 Modified sample holder for low temperature deep level transient spectroscopy current-voltage and capacitance-voltage measurements *Rev. Sci. Instrum.* **63** 2101

Peaker AR 1993 Point and extended defects in semiconductor devices *S. Afr. J. Phys.* **16** 22

Pons D and Bourgoin JC 1985 Irradiation-induced defects in GaAs *J. Phys. C* **18** 3839

Pons D, Makram-Ebeid S 1979 Phonon Assisted Tunnel Emission of Electrons from Deep Levels in GaAs *J. Phys. (Paris)* **40** 1161

Rhoderick EH and Williams RH 1988 *Metal-semiconductor contacts 2nd ed* (Oxford: Clarendon)

Ridly BK 1988 *Quantum Processes in Semiconductors* (Oxford: Oxford)

Ruvimov S 1993 Microstructure of Ti/Al and Ti/Al/Ni/Au Ohmic contacts for *n*-GaN *Appl. Phys. Lett.* **69** 1556

Schottky W 1942 Vereinfachte und erweiterte Theorie der Randschicht-gleichrichter *Z. Phys.* **107** 259

Shockley W and Read WT 1952 Statistics of the Recombinations of Holes and Electrons *Phys. Rev.* **87** 835

Smith RA 1978 *Semiconductors* (Cambridge: Cambridge University)

Song LW, Zhan XD, Benson BW, Watkins GD 1988 Bistable Defect in Silicon: The Interstitial-Carbon-Substitution-Carbon pair *Phys. Rev. Lett.* **60** 460

Street RA and Mott NF 1975 States in the Gap in Glassy Semiconductors *Phys. Rev. Lett.* **35** 1293

Sze SM 1981 *Physics of semiconductor devices* (New York: Wiley)

Wang AC, Sah CT 1985 New method for complete electrical characterization of recombination properties of traps in semiconductors *J. Appl. Phys.* **57** 4645

Watkins GD 1984 Negative-U Properties for Defects in Solids *Festkörperprobleme* **XXIV** 163

Zhan XD and Watkins GD 1993 Electron paramagnetic resonance of multistable interstitial-carbon–substitutional-group-V-atom pairs in silicon *Phys. Rev. B* **47** 6363

Zohta Y and Watanabe MO 1982 On the determination of the spatial distribution of deep centers in semiconducting thin films from capacitance transient spectroscopy *J. Appl. Phys* **53** 1809